Aus dem Walther-Straub-Institut für Pharmakologie und Toxikologie
Institut der Medizinischen Fakultät der Ludwig-Maximilians-Universität München
Vorstand: Prof. Dr. med. Thomas Gudermann

Regulatory mechanisms of the TRPM7 channel-kinase

Dissertation
zum Erwerb des Doktorgrades der Naturwissenschaften
an der Medizinischen Fakultät der
Ludwig-Maximilians-Universität München

vorgelegt von

Eva Schmücker
aus
Neumarkt i. d. Opf., Deutschland

2023

Mit Genehmigung der Medizinischen Fakultät
der Universität München

Betreuer(in):	Prof. Dr. rer. nat. Susanna Zierler
Zweitgutachter(in):	Prof. Dr. rer. nat. Alexander Faußner
Dekan:	Prof. Dr. med. Thomas Gudermann
Tag der mündlichen Prüfung:	02.05.2023

Affidavit

Schmücker, Eva

Name, Vorname

Ich erkläre hiermit an Eides statt, dass ich die vorliegende Dissertation mit dem Titel:

“Regulatory mechanisms of the TRPM7 channel-kinase”

selbständig verfasst, mich außer der angegebenen keiner weiteren Hilfsmittel bedient und alle Erkenntnisse, die aus dem Schrifttum ganz oder annähernd übernommen sind, als solche kenntlich gemacht und nach ihrer Herkunft unter Bezeichnung der Fundstelle einzeln nachgewiesen habe.

Ich erkläre des Weiteren, dass die hier vorgelegte Dissertation nicht in gleicher oder in ähnlicher Form bei einer anderen Stelle zur Erlangung eines akademischen Grades eingereicht wurde.

München, 05.06.23 Eva Schmücker

Ort,Datum
Unterschrift Doktorandin

Table of Contents

Abbreviations

ARF protein	ADP-ribosylation factor protein
ARF	Auxin response factors
ARL15 protein	ADP-ribosylation factor-like protein 15
ATP	Adenosine triphosphate
ChaK	Channel kinase
Ci-VSP	*Ciona intestinalis*- voltage sensitive phosphatase
CNNM	Cyclin and CBS domain divalent metal cation transport mediator
cryo-EM	Cryogenic electron microscopy
DPBS	Dulbecco's phosphate buffered saline
DVF solution	Divalent cation-free solution
EDTA	Ethylene diamine tetraacetic acid
eEF-2 kinase	Elongation factor-2 kinase
EGFP	Enhanced green fluorescent protein
EGTA	Triethylene glycol diamine tetraacetic acid
GTP	Guanosintriphosphate
HEPES	4-(2-Hydroxyethyl)piperazine-1-ethanesulfonic acid
HEK293T cells	Human embryonic kidney 293T cells
HSH	Hypomagnesemia with secondary hypocalcemia
IC_{50}	Half-maximal inhibitory concentration
MagNum currents	Magnesium nucleotide-regulated metal ion currents
MIC currents	Mg^{2+}-inhibited cation currents
MKs	Megakaryocytes
PIP_2	Phosphatidylinositol 4,5-bisphosphate
TRP channels	Transient receptor potential cation channels
TRPM6	Transient receptor potential cation channel melastatin-subfamily member 6

TRPM7	Transient receptor potential cation channel melastatin-subfamily member 7
WT	Wild type

List of publications

1) **Schmidt E**, Narangoda C, Nörenberg W, Egawa M, Rössig A, Leonhardt M, et al. Structural mechanism of TRPM7 channel regulation by intracellular magnesium. Cellular and Molecular Life Sciences 2022;79(225)

2) Kollewe A, Chubanov V, Tseung FT, Correia L, **Schmidt E**, Rössig A, et al. The molecular appearance of native TRPM7 channel complexes identified by high-resolution proteomics. Elife. 2021;10:e68544.

List of figures

1. Contribution to publications

1.1 Publication 1

Publication 1 (1) aimed to address the long-standing question of how intracellular Mg^{2+} levels regulate TRPM7 channel activity. To this end, a collection of mutant TRPM7 channel variants were created and extensively examined using a patch-clamp approach combined with molecular dynamics (MD) simulations. The obtained results support the new concept that the lower channel gate of TRPM7 contains an intersubunit Mg^{2+} binding site which is responsible for the inhibitory action of cytosolic Mg^{2+}.

Based on published cryogenic electron microscopy (cryo-EM) studies with TRPM proteins, I created 25 *Trpm7* cDNA variants with point mutations affecting polar and negatively charged residues, presumably forming a divalent cation binding site in TRPM7. The created TRPM7 variants were transiently expressed in HEK293T cells and evaluated using patch-clamp techniques. The results of these experiments are reported in Figures 1-6, Supplementary Figure S6 and Suppl. Figure S7 as well as in Suppl. Tables S1, S3 and S4.

Figure 1: Cryo-EM analysis of several TRPM proteins (2-10) reported a Ca^{2+} binding site formed by side chains of highly conserved glutamate (E), glutamine (Q), aspartate (D) and asparagine (N) residues located in the S3-S4 transmembrane helices of TRPM channels. Based on these findings, I identified the corresponding residues in mouse TRPM7 and exchanged them to alanine (A) or homologous residues (for instance Q to N, E and D) using a site-directed mutagenesis approach. I studied whether the introduced point mutation affects the channel activity of TRPM7 in the absence of intracellular Mg^{2+} or the presence of 2.3 mM Mg^{2+}. I transiently expressed all 25 TRPM7 mutant variants in HEK293T cells and examined the whole cell TRPM7 currents using the patch-clamp technique. Consequently, I could rule out TRPM7 channel variants with abrogated channel activity. Notably, I identified two mutants (N1097Q and N1098Q), which reduce the response of the channel to 2.3 mM Mg^{2+}. Accordingly, these two channel variants were selected for further detailed assessment.

Figures 2 and Suppl. Table S1: To compare the sensitivity of WT, N1097Q and N1098Q TRPM7 variants to intracellular Mg^{2+} I determined the concentration-dependent suppression of whole-cell currents using different concentrations of

intracellular Mg^{2+} and found that the N1097Q mutant displays normal activity in the presence of physiological Mg^{2+} levels suggesting that the N1097 residue is involved in Mg^{2+} regulation. The N1098Q channel variant was insensitive to intracellular Mg^{2+}.

Figure 3 and Suppl. Table S3 and S4: Because intracellular Mg^{2+} is required for the inhibitory effect of Mg·ATP on the TRPM7 channel, I investigated whether the N1097Q and N1098Q TRPM7 channel variants show a decreased sensitivity to intracellular Mg·ATP in the presence of subphysiological concentration of 0.25 mM Mg^{2+}. In addition, I studied the response of the TRPM7 mutant variants to 9 mM $[Mg{\cdot}ATP]_i$ and physiological levels of $[Mg^{2+}]_i$ (0.55 mM). These experiments demonstrated that the N1097Q and N1098Q mutations were insensitive to intracellular Mg·ATP.

Suppl. Figure S6: I employed perforated patch-clamp recordings to assess TRPM7 currents without manipulating the cytosolic milieu of the cells including Mg^{2+} and Mg·ATP (11). My results demonstrated that the WT TRPM7 channel was supressed in these experimental settings. In contrast, the N1097Q and N1098Q mutant TRPM7 variants showed constitutive activity reinforcing our idea that the N1097Q and N1098Q mutations resulted in a constitutively active channel insensitive to cytosolic Mg^{2+} and Mg·ATP levels in resting cells.

Figure 4 and 5: To test whether the TRPM7 channel variants show a reduced sensitivity exclusively to $[Mg^{2+}]_i$ but not to other ligands I examined whether N1097Q and N1098Q display an altered response to the synthetic TRPM7 channel agonist naltriben (12) and the drug-like TRPM7 channel inhibitor NS8593 (13). The obtained patch-clamp data supported the notion that the N1098Q mutation resulted in a new channel variant which is constitutively active and insensitive to naltriben and NS8593. The N1097Q mutant, however, was sensitive to naltriben activation and NS8593 inhibition.

Figure 6: To analyze whether the TRPM7 channel variants show a reduced sensitivity to other physiological regulators, such as phosphatidylinositol 4,5-bisphosphate (PIP_2), I examined whole-cell patch-clamp currents in HEK293T cells coexpressing the TRPM7 channel variants with recombinant *Ciona intestinalis* voltage-sensitive phosphatase (Ci-VSP) (14), which depletes plasma membrane PIP_2 levels upon depolarization. The Ci-VSP mutant (Ci-VSP-C363S), which is enzymatically inactive, was used in control measurements. The results indicate that

the N1097Q mutant is still sensitive to PIP_2 depletion, whereas the N1098Q mutant was insensitive to such treatment.

Suppl. Figure S7: To test if the introduced point mutation affects the permeability of the TRPM7 channel, whole-cell patch-clamp measurements were performed using a divalent cation free (DVF) solution abolish the block of the channel pore by external divalent cations (15) associated with characteristic changes of the current-voltage (I-V) relationship of TRPM7 currents. My results suggest that the channel's permeability for divalent cations was not affected by the N1097Q and N1098Q mutations.

In accordance with other approaches used in this study, my electrophysiological experiments supported the main conclusion of the publication that the N1097Q mutation results in a channel variant lacking response to the physiological range of $[Mg^{2+}]_i$ but retained sensitivity to other ligands of TRPM7 because the N1097 side-chains form an intersubunit Mg^{2+} regulatory site assessable from the cytosolic side of the channel gate. Furthermore, my electrophysiological analysis supported the notion that the N1098Q mutation leads to a channel variant which is constitutively active and insensitive to physiological and pharmacological regulators of the TRPM7 channel.

1.2 Publication 2

Publication 2 (16) represents a collaborative multidisciplinary study aimed at the isolation of native TRPM7 channel complexes from rodent brain using multiepitope affinity purification approach followed by a functional analysis of reconstructed TRPM7 complexed in heterologous expression in HEK293T and *Xenopus laevis* oocytes and a high-resolution mass spectrometry. These experiments revealed that TRPM7 forms ternary complexes with ADP-ribosylation factor-like protein 15 (ARL15) and the putative divalent metal transporter proteins CNNM1-4. Functional evaluation of the TRPM7 channel showed that ARL15 potently inhibits the TRPM7 channel activity. In contrast, CNNM3 displayed no effect on the TRPM7 channel activity. However, CNNM3 elicited a profound inhibitory effect on the kinase activity of TRPM7.

In the study I was responsible for the experiments shown in Figure 4-figure supplement 1 reporting patch-clamp results and Western-blot analysis of TRPM7 characteristics examined in the absence and presence of CNNM3 as shown in Figure 5-figure supplement 1. Figures are referred according to original eLife style.

Figure 4-figure supplement 1: To investigate whether CNNM3 can influence the Mg^{2+} permeability of the TRPM7 channel, I measured whole-cell currents in HEK293T cells expressing mouse TRPM7 alone or coexpressed with mouse CNNM3. Patch-clamp experiments revealed that the TRPM7 channel remained similarly permeable to Mg^{2+} regardless of the presence of CNNM3.

Figure 5-figure supplement 1: I studied whether CNNM3 affects the activity of the TRPM7 kinase domain in the TRPM7 channel. To address this question, I used an antibody, which specifically recognizes the known autophosphorylation residue Ser1511 ((p)Ser1511) in TRPM7 (17). To show that this antibody can be used for functional analysis of the TRPM7 kinase, I examined the effects of a known drug-like TRPM7 kinase inhibitor TG100-115 (18). To this end, I exposed living TRPM7 transfected HEK293T cells to different concentrations of TG100-115 and observed a concentration-dependent reduction in the (p)Ser1511 TRPM7 signal by Western-blot analysis. Furthermore, I observed that this inhibitory effect of TG100-115 was completely reversible after wash-out of TG100-115 using cell-culture medium. In addition, I could show that the inhibitory action of TG100-115 was time-dependent. Therefore, I concluded that the detection of (p)Ser1511 levels of TRPM7 is suitable

to monitor TRPM7 kinase activity. Consequently, this approach was used in the study to assess the inhibitory effect of CNNM3 on the kinase domain of TRPM7.

2. Introduction

2.1 The TRPM gene family of cation channels

The transient receptor potential cation channel, subfamily M (melastatin), member 7 (TRPM7) is a membrane protein compromising a cation channel unit linked to a cytosolic kinase domain. In mammals, eight melastatin-related TRP (TRPM) proteins represent a subgroup (family) of a large superfamily of transient receptor potential (TRP) ion channels. Similar to other TRP channels, TRPM channels, including TRPM7, function as tetramers. Every channel subunit contains six transmembrane helices (S1-S6). The pore-forming sequence is present between S5 and S6 (19). TRPM channels display exceptional variability in functional properties such as ion selectivity and activation mechanisms (20).

Melastatin or TRPM1 is the first discovered member of the TRPM subfamily. TRPM1 transcripts were initially found in melanoma-derived cells and thought to be associated with melanoma progression (20). Intriguingly, the functional characteristics of the TRPM1 channel remain poorly understood (20).

The close homolog of TRPM1, TRPM3 functions as a constitutively active cation channel, which is highly selective for Ca^{2+} (21). TRPM3 is further activated via heat stimuli (25-40°C) (22) and steroid pregnenolone sulfate (21-24).

TRPM2 represents an unusual type of ion channel because its channel moiety is linked to a C-terminal ADP-ribose pyrophosphatase domain. TRPM2 is defined as a nonselective cation channel, which is well permeable to Ca^{2+} and Na^{+} (25, 26). TRPM2 is activated by reactive oxygen species- and intracellular ADP-ribose and potentiated by cytosolic Ca^{2+} (27, 28).

A genetically related protein, TRPM8, lacks enzyme-like domains. The TRPM8 channel also shows no preference for monovalent and divalent cations. TRPM8 is activated by cold temperatures (8-26°C) (29) and ‘cooling’ compounds such as menthol (30, 31).

TRPM4 and TRPM5 are unique members of the TRP superfamily because these channels are selective for monovalent cations (i.e. Na^{+}) and, unlike other TRPs, are not permeable to Ca^{2+}. TRPM4 and TRPM5 are directly activated by an increase in cytosolic Ca^{2+} concentration, for instance, after activation by G-protein-coupled

receptors linked to phospholipase C (PLC) followed by a release of Ca^{2+} from intracellular Ca^{2+} stores (32, 33).

The remaining members of the TRPM subfamily, TRPM6 and TRPM7, form channel complexes that are selective for divalent cations, such as Zn^{2+}, Mg^{2+} and Ca^{2+} (34, 35) and are poorly permeable to monovalent cations under physiological conditions. The channel activity of TRPM6 and TRPM7 is negatively regulated by cytosolic Mg^{2+} and Mg·ATP. TRPM6 and TRPM7 are remarkable TRP channels because both proteins contain a C-terminal kinase domain and are often referred to as channel-kinases and chanzymes. The kinase segments of TRPM6 and TRPM7 belong to a group of atypical Ser/Thr protein kinases called α-kinases (15, 36-40).

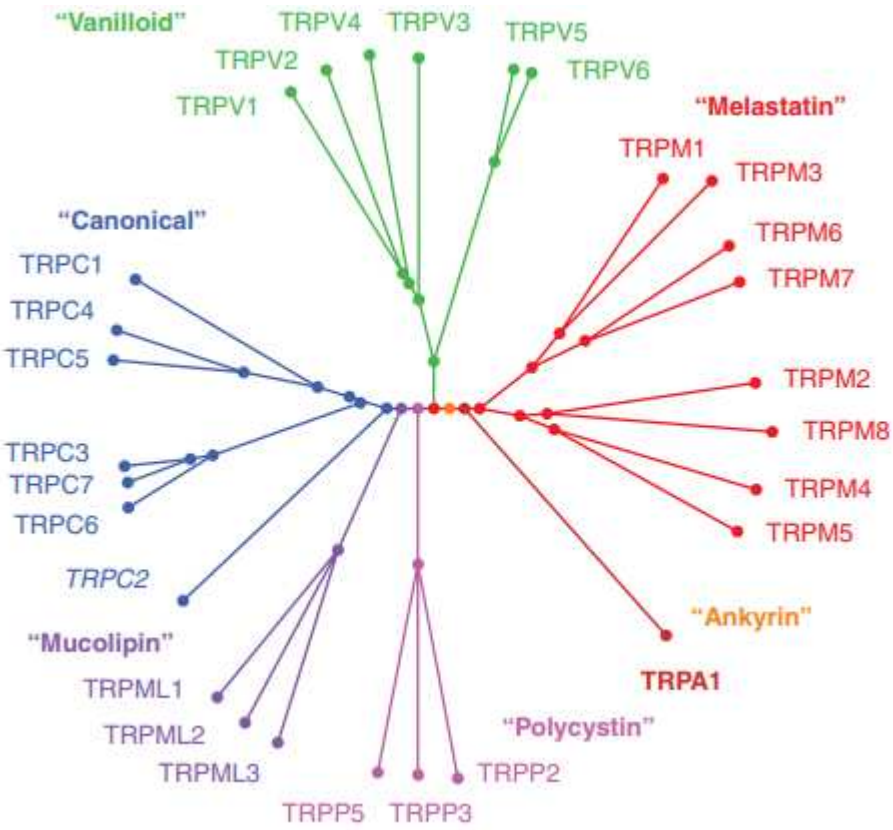

Figure 1. Phylogenetic tree of the mammalian TRP-channel family. The tree outlines the homology of human TRP proteins. The figure was taken from Gees *et al.*, 2010 (41).

2.2 Physiological roles of TRPM6 and TRPM7

Clinical studies with patients harboring mutations in the *TRPM6* and *TRPM7* genes and experiments with genetic animal models provided evidence that the channel-kinases TRPM6 and TRPM7 play a crucial role in the systemic homeostasis of Mg^{2+} and other divalent cations.

Thus, loss-of-function mutations in the human *TRPM6* gene underlie a rare genetic disease known as hypomagnesemia with secondary hypocalcemia (HSH) (39, 40). HSH is an autosomal recessive disorder characterized by very low Mg^{2+} levels in affected children. Mg^{2+} deficiency in HSH patients induces secondary symptoms including low Ca^{2+} levels, seizures, muscle spasms and can result in neurological damage and mortality. However, oral or intravenous Mg^{2+} supplementation enables the restoration of subnormal serum Mg^{2+} levels and ameliorates the secondary symptoms of this syndrome (36, 39, 40).

The mechanisms of HSH have been extensively investigated in genetic mouse genetic models (39, 40) and *in vitro* experiments with recombinant TRPM6 (36). Thus, our research group (42) proposed that TRPM6 forms heteromeric channel complexes with TRPM7 responsible for maintaining nutritional uptake of Mg^{2+} in intestinal epithelial cells. Genetic ablation of TRPM6 in mice results in severe hypomagnesemia, failure to grow and death of mutant animals. However, similar to HSH patients, dietary Mg^{2+} supplementation rescued these phenotypes (42).

In addition, one study (46) reported that TRPM7 plays a role in balancing the whole body Mg^{2+} homeostasis. Thus, the authors explored mice heterozygous for mutations in *Trpm7* locus. The mutation was generated by deletion of exons encoding the kinase domain of TRPM7 leading to an expression of a nonfunctional TRPM7 channel and consequently a reduction of endogenous TRPM7 currents in primary cells isolated from these mice. The mutation adult mice were viable but showed lower plasma and erythrocyte Mg^{2+} concentrations as well as a reduced Mg^{2+} storage in bones and signs of limb clasping and seizures indicating that TRPM7 is critically involved in the Mg^{2+} homeostasis (46).

Loss-of-function point mutations in the human *TRPM7* gene affect the ability of megakaryocytes (MKs) to produce platelets leading to the development of macrothrombocytopenia in human subjects heterozygous for such genetic alterations (49). Macrothrombocytopenia stands for the presence of a giant platelet

disorder often containing large vacuoles (49). In an animal model, Stritt et al. reported that MK-specific knockout of *Trpm7* in mice induced macrothombocytopenia. In contrast, mice carrying a kinase-dead point mutation (K1646R) in *Trpm7* did not develop any morphological and functional alterations of platelets indicating that impaired TRPM7 channel function rather than its kinase activity caused macrothrombocytopenia in mutant mice and humans (49). Notably, the intracellular Mg^{2+} concentration in *Trpm7*-deficient platelets was significantly reduced suggesting that the TRPM7 channel is essential for Mg^{2+} uptake. In addition, *Trpm7*-deficient platelets displayed cytoskeletal alterations, which were rescued by dietary Mg^{2+} supplementation of mutant mice. Taken together, it was suggested that impaired Mg^{2+} uptake triggered the pathophysiological changes in MKs and platelets observed in MK-specific knockout mice (49).

Another study by our group demonstrated that the TRPM7 channel functions as the central gatekeeper of the intestinal transport of divalent cations (45). Enterocyte-specific knockout of *Trpm7* in mice caused a substantial reduction in body weight and 100% lethality of preweened mutant individuals. Determining Ca^{2+}, Mg^{2+} and Zn^{2+} levels in serum and bones revealed that *Trpm7*-deficient mice developed severe deficiency in these cations. Consistently, dietary supplementation of breast-fed dams with Zn^{2+} and Mg^{2+} extended the survival rate of mutant offspring (45).

Extensive studies of TRPM7 in mouse embryonic tissues have been performed (43). An epiblast-restricted knockout of *Trpm7* leads to lethality, suggesting that *Trpm7* is essential for early embryonic development. In line with this finding, global deletion of *Trpm7* also caused embryonic mortality at embryonic days 7-9. However, ablation of *Trpm7* at later embryonic stages (embryonic day 14.5) did not affect prenatal development of mice and resulted in viable *Trpm7* null offspring indicating that the TRPM7 channel is required only before and during organogenesis (43).

2.3 Structure-functional relationships of TRPM7

Analogous to other TRP channels, four TRPM7 subunits form symmetric tetrameric channel complexes. A large N-terminal domain of the TRPM7 subunit contains four conserved segments referred to as melastatin-homology domains (MHD1-4), followed by a hydrophobic linker region (LH) connected to six transmembrane domains (S1-6) with the pore-forming loop (PL) and pore helix (PH) located between S5 and S6. The C-terminus of TRPM7 comprises a conserved TRP domain (TRP), a coiled-coiled (CC) domain (50) linked to a kinase substrate (SD) domain harboring a stretch of serine and threonine residues subjected to autophosphorylation by the C-terminal kinase domain (KD) (Figure 1) (51).

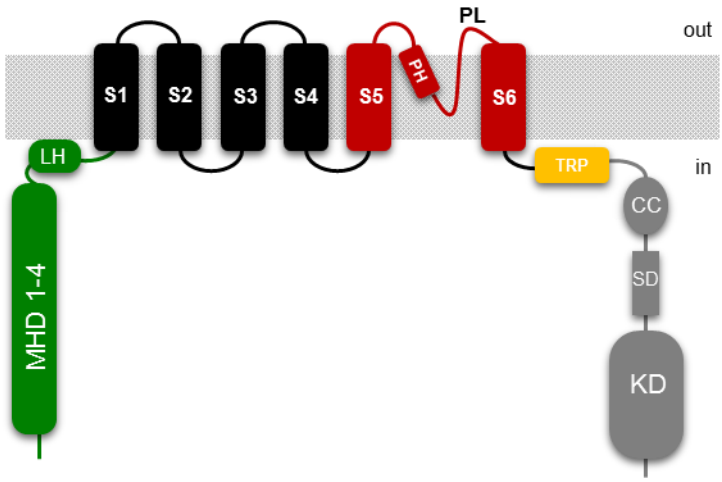

Figure 2. Domain topology of TRPM7. The N-terminus of the channel protein consists of four melastatin-homology domains (MHD) and a hydrophobic linker region (LH) The channel segment possesses six transmembrane domains (S1–S6) with the pore helix (PH) and the pore-forming loop (PL) located between S5 and S6. The C-terminus of the TRPM7 channels comprises four domains, a transient receptor potential (TRP) domain, a coiled-coil (CC) domain, a kinase substrate domain (SD) and a kinase domain (KD). The figure was modified and taken from Ferioli *et al.*, 2017 (51).

The kinase domain of TRPM7 belongs to a group of atypical protein kinases entitled α-kinases because they preferentially to phosphorylate serine and threonine residues located in the α-helices in substrate proteins (52, 53). The first known member of this group is the eukaryotic elongation factor-2 (eEF-2) kinase. Other proteins of this group are α-kinase 1, 2 and 3 (ALPK 1-3) (54).

The functional role of the TRPM7 kinase was explored in three directions. First, it was found that the TRPM7 kinase phosphorylates other proteins, including eEF-2, TRPM6, annexin A1, myosin II, STIM2, SMAD2 and Rho A (17, 55-60). Second, it was suggested that stimulation of the Fas-receptor in immune cells induced caspase-mediated cleavage of the kinase domain from channel segments of TRPM7 and this process was implicated in Fas-induced apoptosis (61). In addition, the cleaved TRPM7 kinase domain can translocate to the nucleus to promote histone phosphorylation leading to alterations in the transcriptional profile (62). Finally, it was demonstrated that the TRPM7 kinase could autophosphorylate its own residues located primarily in the SD domain but also in other segments of TRPM7 (17, 63).

The resolved crystal structure of the TRP channel kinase domain (64) revealed that the residues required for catalytic activity are highly conserved among α-kinases and more distantly related kinases. Additionally, the structure showed that there is a noticeable similarity in the folding of the whole kinase TRPM7 domain and classical protein kinases, such as cAMP dependent protein kinase (PKA). Furthermore, the TRPM7 kinase displayed a characteristic C-terminal glycine-rich motif, which can be involved in peptide substrate recognition and a Zn^{2+} binding site located in the C-terminal lobe of the TRPM7 kinase (64).

Recently, a cryo-EM analysis of the truncated TRPM7 channel (lacking the kinase domain) was reported. The structures of TRPM7 tetramers were obtained in the presence and absence of Mg^{2+} (65). Cryo-EM analysis captured the TRPM7 channel in the closed conformation in all conditions. Thus, structural rearrangements associated with the TRPM7 channel in the open state were not addressed and consequently, the action of physiological regulators (Mg^{2+}, Mg·ATP and PIP_2) on the TRPM7 channel remain mechanistically elusive (65). Nevertheless, the obtained structures revealed particular residues forming the ion selectivity filter of TRPM7. Thus, it was found that Mg^{2+} is present in the outer segment of the channel pore and interacts with the negatively charged side chain of four E1047 residues (Figure 2). The most constricted site of the lower channel gate was formed by isoleucine (I1093) and asparagine (N1097) residues of TRPM7 (Figure 2) (65).

Patch-clamp experiments with recombinant TRPM7 expressed in heterologous expression systems demonstrated that the TRPM7 channel is highly permeable to divalent cations (15, 59, 66). The channel's permeability sequence is: $Zn^{2+} \approx Ni^{2+} >> Ba^{2+} > Co^{2+} > Mg^{2+} \geq Mn^{2+} \geq Sr^{2+} \geq Cd^{2+} \geq Ca^{2+}$ (35). However, in a divalent cation-

free (DVF) extracellular solution the TRPM7 channel is able to conduct monovalent cations such as Na^+ because the extracellular block of divalent cations is removed under such experimental conditions (59, 67).

Two research groups (65, 68) revealed a structural basis of the high divalent permeability of the TRPM7 channel. Both groups proposed that a negatively charged side chain of the glutamate residue (E1047) located in the predicted pore-forming loop of the channel (Figure 2) forms an intersubunit cation binding site, which efficiently discriminates divalent and monovalent cations. Consequently, neutralization of E1047 using site-directed mutagenesis (E1047Q) was sufficient to abolish the high selectivity of TRPM7 to divalent cations i.e. mutant channel became well permeable to Na^+ in the presence of divalent cations (68). In accord with this concept, the recently published cryo-EM data revealed that Mg^{2+} is in direct contact with the side chains of four E1047 located in the selectivity filter of the TRPM7 channel (65).

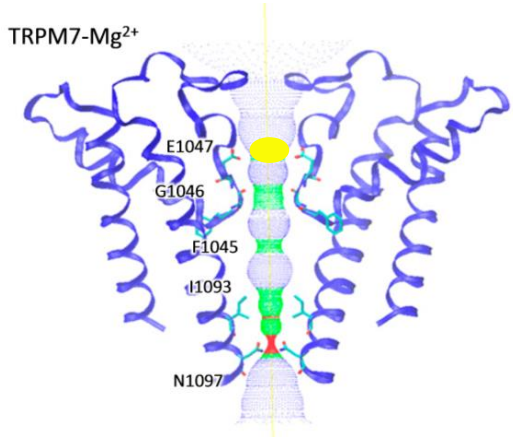

Figure 3. Ion conduction pathway in the TRPM7 channel structure. The residues E1047, G1046 and F1045 in the pore helix (PH) form the selectivity filter of the TRPM7 channel. Residues I1093 and N1097 of S6 are located in the lower channel gate. Mg^{2+} is indicated in yellow. The figure was modified from Duan et al., 2018 (65).

A commonly accepted view is that depleting intracellular free Mg^{2+} and Mg·ATP leads to an induction of the TRPM7 channel activity. Of note, endogenous TRPM7 currents were initially found in patch-clamp experiments with Jurkat T cells after intracellular Mg^{2+} was removed in the patch pipette solution containing high concentrations of EDTA/EGTA (15, 69, 70). In addition, Mg·ATP synergistically with free Mg^{2+} inhibits TRPM7 currents (3). Accordingly, the addition of free Mg^{2+} and

Mg·ATP to the intracellular patch pipette solution prevents the opening of the TRPM7 channel (15, 59, 70). Therefore, TRPM7 currents are frequently named magnesium-inhibited cation (MIC) currents and magnesium-nucleotide-regulated metal ion (MagNuM) currents (15, 70). Based on such an approach, many studies have registered TRPM7 currents in an extensive collection of cell lines, primary isolated cells or cells transfected with *Trpm7* cDNA expression constructs (43, 71, 72).

Phosphatidylinositol 4,5-bisphosphate (PIP_2) represents another crucial regulatory factor of TRPM7. It was reported that TRPM7 channel activity decreased upon M1 receptor stimulation by carbachol, indicating that G-protein-coupled receptor-mediated activation of phospholipase C (PLC) leads to PIP_2 hydrolysis and consequently to inhibition of the TRPM7 channel (73). In addition, some studies propose that Mg^{2+} affects TRPM7 indirectly by interfering with the binding of PIP_2 to TRPM7 (11, 73). However, the structural basis of the effect of PIP_2 remains unknown.

While it is commonly accepted that Mg^{2+}, Mg·ATP and PIP_2 are physiological regulators of TRPM7, the molecular mechanisms underlying the action of these ligands on TRPM7 remain unclear. Since the TRPM7 channel comprises a kinase domain, the regulatory role of this domain was investigated in initial studies (3, 11, 74, 75). Thus, several research groups reported that the introduction of a kinase-dead point mutation or the deletion of the whole kinase domain resulted in only modestly affected Mg^{2+} sensitivity or produced a nonfunctional TRPM7 channel variant (74, 75). Hence, the TRPM7 channel kinase activity is likely not essential for channel regulation by intracellular Mg^{2+}.

One study (74) proposed that the kinase domain implicated the action of Mg·ATP because the kinase-dead point mutation fully removed the channel's sensitivity to Mg·ATP whereas the Mg^{2+} sensitivity remained unaffected (74) supporting the idea that Mg^{2+} and Mg·ATP act on different regulatory sites of TRPM7. However, other groups demonstrated that the kinase domain of TRPM7 plays no role in the regulation of TRPM7 by Mg^{2+} and Mg·ATP (11, 75).

Recently our group (16) performed proteome-wide screens of native TRPM7 channel complexes in rodent brains and revealed the association of TRPM7 with ADP-ribosylation factor-like protein 15 (ARL15) and metal transporters CNNM1-4 (16, 76, 77). ARL15 is a small GTP-binding protein from the auxin response factor (ARF)

gene family (78). A shared characteristic of ARF proteins is their GTP-induced ability to bind and regulate effector proteins. GTPase-activating proteins (GAPs) in association with GTP exchange factors (GEFs) control the GTP- and GDP-bound states of ARFs. The main involvements of the characterized ARFs are remodeling of the cytoskeleton, membrane trafficking and phospholipid metabolism (78).

Functional analysis of TRPM7 expressed alone or coexpressed with ARL15 revealed that ARL15 inhibits the TRPM7 channel activity (16). In contrast, coexpression of CNNM3 and TRPM7 did not induce detectable effects on the TRPM7 channel but potently inhibited the kinase activity (16). However, another study (79) reported that CNNM2 and CNNM4 interact with TRPM7 and positively regulated the channel activity.

Several laboratories have identified small organic compounds acting as inhibitors of the TRPM7 channel. Among other entities, waixenicin A has been identified as a potent channel blocker with an IC_{50} value of 7.0 µM in the absence of intracellular free Mg^{2+} and 16 nM in the presence of 700 µM free Mg^{2+} (80). Waixenicin A, a natural terpenoid of a soft coral (*Sarcothelia edmondsoni*), was identified as an irreversible channel blocker (80). In addition, a synthetic TRPM7 channel inhibitor, NS8593, was identified (13). NS8593 reversibly blocks TRPM7 currents in primary isolated cells as well as in HEK293T cells transfected with *Trpm7* cDNA with an IC_{50} of 1.6 µM (13).

In addition, several TRPM7 channel agonists were found. The most potent activator is naltriben (EC_{50} value of 20.7 µM) which is able to stimulate TRPM7 currents in the presence of intracellular Mg^{2+} and depleted PIP_2 (12). Naltriben is an antagonist of δ-opioid receptors (12). Consequently, waixenicin A, NS8593 and naltriben were broadly used to map the function of TRPM7 in stable cell lines and primary isolated cells (12, 13, 80). However, the ligandbiding sites of waixenicin A and NS8593 as well as the mechanisms of their action on TRPM7 remain unknown.

Taken together, significant progress has been made in the mechanistic understanding of TRPM7 functions. Nevertheless, the structural basis of the modulatory effects of natural and synthetic ligands on TRPM7 remains poorly understood.

2.4 Research goals

TRPM7 channel-kinase plays an essential role in the cellular uptake of divalent cations. Despite extensive investigations, the question of how the TRPM7 channel activity is regulated remains to be addressed. Thus, fluctuations in cytosolic Mg^{2+} regulate TRPM7 currents, but the molecular basis of such Mg^{2+} action on TRPM7 remains unknown. In addition, the functional role of newly identified accessory proteins of TRPM7 channel complexes, such as CNNM1-4 and ARL15 remains unclear. Therefore, this study aims to elucidate the regulatory mechanisms of intracellular Mg^{2+} and the CNNM3 protein, a recently identified interaction partner of TRPM7.

Specifically, we aimed to address the following key questions:

1. What are the molecular mechanisms by which Mg^{2+} regulates the TRPM7 channel? (Publication 1)

2. Do Mg^{2+}, Mg·ATP and PIP_2 act on TRPM7 through a common regulatory mechanism or an independent mechanism? (Publication 1)

3. Can CNNM3 affect the channel or kinase activity of TRPM7? (Publication 2)

3. Conclusions

The present study aimed to identify the regulatory mechanisms of the TRPM7 channel kinase. Accordingly, the obtained experimental data supported the following conclusions:

1. The side chains of N1097 in the lower gate of the TRPM7 channel form an intersubunit Mg^{2+}-regulatory site underlying the sensitivity of TRPM7 currents to cytosolic free Mg^{2+}.

2. The interaction of Mg2+ with the side-chains of N1097 leads to a stabilization of the TRPM7 channel in the closed conformation.

3. The point mutations N1097Q and N1098Q in TRPM7 destroy the Mg^{2+} regulatory site and eliminate the sensitivity of the TRPM7 channel to intracellular free Mg^{2+} at physiological range.

4. CNNM3 is a new interaction partner of TRPM7, which acts as a negative regulator of TRPM7 kinase.

4. Abstract

The transient receptor potential cation channel, subfamily M, member 7 (TRPM7) is a bifunctional protein containing a transmembrane channel segment and a serine/threonine-protein kinase domain. The TRPM7 channel is selective to divalent cations. TRPM7 regulates many biological processes such as the organismal balance of Zn^{2+}, Ca^{2+} and Mg^{2+}, immunity, embryonic development and cell signalling. The widely accepted view is that cytosolic Mg^{2+} and Mg·ATP inhibit the TRPM7 channel to link the metabolic state of the cell to the uptake of divalent cations. More recently, independent studies focusing on the identification of native TRPM7 channel complexes revealed the association of TRPM7 with the metal transporters CNNM1-4. However, the mechanisms underlying TRPM7 sensitivity to intracellular Mg^{2+} and the regulatory role of CNNM1-4 remain poorly understood. Therefore, we used site-directed mutagenesis, patch-clamp measurements and other techniques to demonstrate that a regulatory Mg^{2+} binding site is formed by the side chains of N1097 in mouse TRPM7. Our results suggest a direct interaction between Mg^{2+} and N1097 leading to a stabilization of the TRPM7 in the closed conformation. In line with these findings, we showed that the sensitivity of TRPM7 to physiological concentrations of intracellular Mg^{2+} was selectively affected by an introduction of point mutation (N1097Q). In addition, our results indicate that the CNNM3 protein has no effect on the TRPM7 channel but rather negatively regulates the kinase activity of TRPM7. Thus, our study suggests new mechanistic insights into the regulatory characteristics of the kinase-coupled TRPM7 channel.

5. Zusammenfassung

Der Transient-Rezeptor-Potential-Kationenkanal, Unterfamilie M, Mitglied 7 (TRPM7) ist ein bifunktionelles Protein, das ein Transmembrankanalsegment umfasst, was mit einer Serin/Threonin-Proteinkinase-Domäne fusioniert ist. Der TRPM7-Kanal ist selektiv für Zn^{2+}, Ca^{2+} und Mg^{2+}. TRPM7 reguliert zahlreiche biologische Prozesse wie die Zn^{2+}-, Ca^{2+}- und Mg^{2+}-Homöostase im Organismus, die Embryonalentwicklung, Immunreaktionen und Signaltransduktion. Eine weit verbreitete Ansicht ist, dass zytosolisches Mg^{2+} und Mg·ATP als negative Regulatoren des TRPM7-Kanals wirken, um die Aufnahme zweiwertiger Kationen auf den Stoffwechselzustand der Zelle anzupassen. Kürzlich haben unabhängige Studien, die sich auf die Identifizierung nativer TRPM7-Kanalkomplexe konzentrierten, die Verbindung von TRPM7 mit den Metalltransportern CNNM1-4 aufgezeigt. Die Mechanismen, die der Sensitivität von TRPM7 gegenüber intrazellulärem Mg^{2+} und der regulatorischen Rolle von CNNM1-4 zugrunde liegen, sind jedoch nach wie vor kaum verstanden. Daher haben wir eine Kombination aus ortsgerichteter Mutagenese, Patch-Clamp-Techniken, Western-Blotting und 3D-Proteinmodelierung eingesetzt, um zu zeigen, dass die Seitenketten von N1097 in TRPM7 in der Maus zwischen den Untereinheiten eine Mg^{2+}-regulierende Stelle bilden. Unsere Ergebnisse legen nahe, dass Mg^{2+} direkt mit diesem Proteinsegment interagiert und dadurch TRPM7 im geschlossenen Zustand stabilisiert. In Übereinstimmung mit diesem Modell haben wir festgestellt, dass Punktmutationen in der Mg^{2+}-Regulationsstelle (N1097Q und N1098Q) die Sensitivität von TRPM7 gegenüber physiologischen Konzentrationen von intrazellulärem Mg^{2+} aufhebt. Darüber hinaus deuten unsere Ergebnisse darauf hin, dass das CNNM3-Protein keine Auswirkungen auf den TRPM7-Kanal hat, sondern vielmehr die Kinaseaktivität von TRPM7 negativ reguliert. Unsere Studie liefert somit neue mechanistische Erkenntnisse über die regulatorischen Eigenschaften des Kinase-gekoppelten TRPM7-Kanals.

6. Publication 1

Title: Structural mechanism of TRPM7 channel regulation by intracellular magnesium

https://link.springer.com/article/10.1007/s00018-022-04192-7

https://doi.org/10.1007/s00018-022-04192-7

Cellular and Molecular Life Sciences (2022) 79:225
https://doi.org/10.1007/s00018-022-04192-7

ORIGINAL ARTICLE

Structural mechanism of TRPM7 channel regulation by intracellular magnesium

Eva Schmidt[1] · Chamali Narangoda[2] · Wolfgang Nörenberg[3] · Miyuki Egawa[1] · Anna Rössig[1] · Marion Leonhardt[3] · Michael Schaefer[3] · Susanna Zierler[1,4] · Maria G. Kurnikova[2] · Thomas Gudermann[1,5] · Vladimir Chubanov[1]

Received: 22 October 2021 / Revised: 26 January 2022 / Accepted: 2 February 2022

Abstract

Zn^{2+}, Mg^{2+} and Ca^{2+} are essential divalent cations implicated in many metabolic processes and signalling pathways. An emerging new paradigm is that the organismal balance of these cations predominantly depends on a common gatekeeper, the channel-kinase TRPM7. Despite extensive electrophysiological studies and recent cryo-EM analysis, an open question is how the channel activity of TRPM7 is activated. Here, we performed site-directed mutagenesis of mouse TRPM7 in conjunction with patch-clamp assessment of whole-cell and single-channel activity and molecular dynamics (MD) simulations to show that the side chains of conserved N1097 form an inter-subunit Mg^{2+} regulatory site located in the lower channel gate of TRPM7. Our results suggest that intracellular Mg^{2+} binds to this site and stabilizes the TRPM7 channel in the closed state, whereas the removal of Mg^{2+} favours the opening of TRPM7. Hence, our study identifies the structural underpinnings through which the TRPM7 channel is controlled by cytosolic Mg^{2+}, representing a new structure–function relationship not yet explored among TRPM channels.

Keywords TRPM7 · TRP channels · Magnesium · PIP_2 · ATP · Molecular dynamics simulations

Introduction

The transient receptor potential cation channel, subfamily M, member 7 (TRPM7) encodes a bi-functional protein comprising a transmembrane channel segment fused to a serine/threonine-protein kinase domain [1–3]. The TRPM7 channel is highly permeable to divalent cations, including Zn^{2+}, Ca^{2+}, and Mg^{2+}, and there is mounting evidence to suggest that the influx of all three cations underlies the indispensable physiological role of TRPM7 [4–8]. Thus, TRPM7 controls a wide range of biological processes such as organismal Zn^{2+}, Ca^{2+} and Mg^{2+} homeostasis, embryonic development, immune responses, cell motility, proliferation and differentiation [1–3].

TRPM7 currents were discovered in patch-clamp experiments with immune cells after removing Mg^{2+} from pipette solutions [9–11]. In contrast, the addition of free Mg^{2+} and Mg·ATP prevented the opening of the TRPM7 channel through different mechanisms [11–13]. Moreover, free Mg^{2+} and Mg·ATP inhibit TRPM7 synergistically, since elevation of free Mg^{2+} concentrations increases the potency of Mg·ATP [13]. TRPM7 currents were thus termed magnesium-nucleotide-regulated metal ion currents (MagNuM) and magnesium-inhibited cation currents (MIC) [11, 12]. In the past two decades, this experimental paradigm was commonly used to identify TRPM7 currents in a wide variety of primary isolated cells and stable cell lines [1–3]. The current consensus is that both Mg^{2+} and Mg·ATP act as negative

Maria G. Kurnikova: corresponding author for theoretical analysis.

✉ Thomas Gudermann
thomas.gudermann@lrz.uni-muenchen.de

✉ Vladimir Chubanov
vladimir.chubanov@lrz.uni-muenchen.de

1 Walther-Straub Institute of Pharmacology and Toxicology, LMU Munich, Munich, Germany

2 Chemistry Department, Carnegie Mellon University, Pittsburgh, PA, USA

3 Rudolf-Boehm Institute of Pharmacology and Toxicology, Leipzig University, Leipzig, Germany

4 Institute of Pharmacology, Johannes Kepler University Linz, Linz, Austria

5 Comprehensive Pneumology Center, a member of the German Center for Lung Research (DZL), Munich, Germany

Published online: 07 April 2022

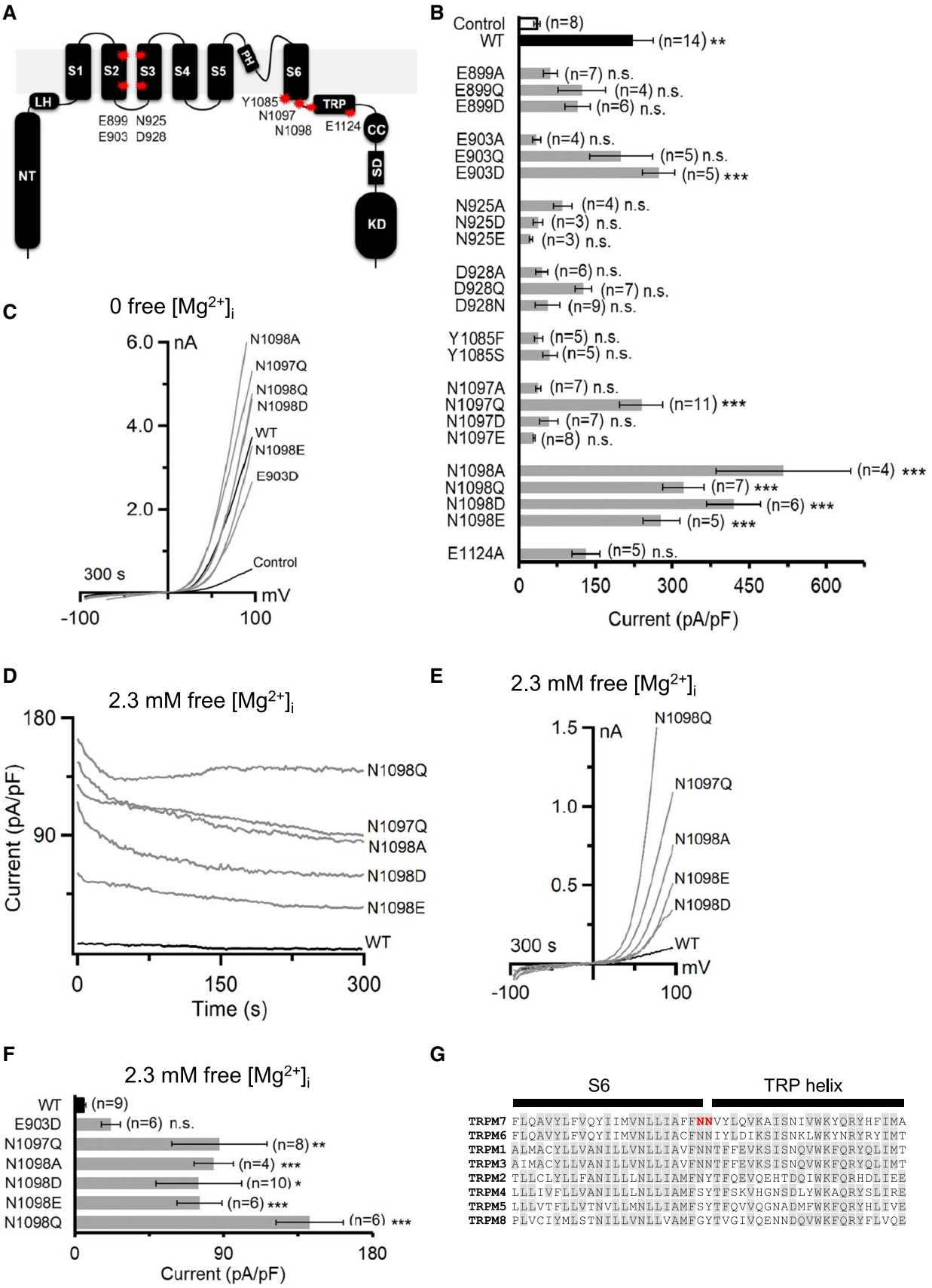
A
S1
S2
S3
S4
S5
PH
S6
LH
NT
E899 N925
E903 D928
Y1085
N1097
N1098
TRP
E1124
CC
SD
KD
B
Control
WT
(n=8)
(n=14) **
E899A
E899Q
E899D
(n=7) n.s.
(n=4) n.s.
(n=6) n.s.
E903A
E903Q
E903D
(n=4) n.s.
(n=5) n.s.
(n=5) ***
N925A
N925D
N925E
(n=4) n.s.
(n=3) n.s.
(n=3) n.s.
D928A
D928Q
D928N
(n=6) n.s.
(n=7) n.s.
(n=9) n.s.
Y1085F
Y1085S
(n=5) n.s.
(n=5) n.s.
N1097A
N1097Q
N1097D
N1097E
(n=7) n.s.
(n=11) ***
(n=7) n.s.
(n=8) n.s.
N1098A
N1098Q
N1098D
N1098E
(n=4) ***
(n=7) ***
(n=6) ***
(n=5) ***
E1124A
(n=5) n.s.
0
150
300
450
600
Current (pA/pF)
C
0 free [Mg2+]i
6.0 nA
4.0
2.0
N1098A
N1097Q
N1098Q
N1098D
WT
N1098E
E903D
Control
300 s
mV
-100
100
D
2.3 mM free [Mg2+]i
180
90
Current (pA/pF)
N1098Q
N1097Q
N1098A
N1098D
N1098E
WT
0
150
300
Time (s)
E
2.3 mM free [Mg2+]i
1.5 nA
1.0
0.5
N1098Q
N1097Q
N1098A
N1098E
N1098D
WT
300 s
mV
-100
100
F
2.3 mM free [Mg2+]i
WT
E903D
N1097Q
N1098A
N1098D
N1098E
N1098Q
(n=9)
(n=6) n.s.
(n=8) **
(n=4) ***
(n=10) *
(n=6) ***
(n=6) ***
0
90
180
Current (pA/pF)
G
S6
TRP helix
TRPM7 FLQAVYLFVQYIIMVNLLIAFFNNVYLQVKAISNIVWKYQRYHFIMA
TRPM6 FLQAVYLFVQYIIMVNLLIACFNNIYLDIKSISNKLWKYNRYRYIMT
TRPM1 ALMACYLLVANILLVNLLIAVFNNTFFEVKSISNQVWKFQRYQLIMT
TRPM3 AIMACYLLVANILLVNLLIAVFNNTFFEVKSISNQVWKFQRYQLIMT
TRPM2 TLLCLYLLFANILLLNLLIAMFNYTFQEVQEHTDQIWKFQRHDLIEE
TRPM4 LLLIVFLLVANILLLNLLIAMFSYTFSKVHGNSDLYWKAQRYSLIRE
TRPM5 LLLVTFLLVTNVLLMNLLIAMFSYTFQVVQGNADMFWKFQRYHLIVE
TRPM8 PLVCIYMLSTNILLVNLLVAMFGYTVGIVQENNDQVWKFQRYFLVQE

◂**Fig. 1** Assessment of the mouse TRPM7 variants expressed in HEK293T cells. **A** Domain topology of TRPM7. A large N-terminus (*NT*) of TRPM7 is linked to a pre-S1 helix also known as a linker-helical domain (*LH*) preceding a channel segment comprising six transmembrane helices (*S1–6*) with a short pore loop and a pore helix (*PH*) located between S5 and S6. The C-terminus of TRPM7 contains a receptor potential domain (*TRP*) followed by a coiled-coil (*CC*), kinase substrate (*SD*) and kinase (*KD*) domains. Red stars indicate the position of residues in the mouse TRPM7 protein subjected to site-directed mutagenesis in the present study. **B** Whole-cell currents measured in untransfected HEK293T cells (Control, white) and the cells transfected by wild type (WT, black) or indicated mutant variants (grey) of TRPM7-YFP cDNAs. Currents were induced using the standard $[Mg^{2+}]_i$-free intracellular solution and the standard external solution. Current amplitudes (mean ± SEM) were acquired at + 80 mV (at 300 s). *n*, number of cells measured; n.s., not significant; $*P<0.05$ $**P<0.01$; $***P<0.001$ (ANOVA, compared to Control). **C** Representative I–V relationships of currents shown in **B**. **D–F** A subset of TRPM7-YFP variants shown in **B** were examined using an intracellular solution containing 2.3 mM $[Mg^{2+}]_i$ (Suppl. Table S1). **D** Whole-cell currents measured in WT and indicated mutant variants of TRPM7-YFP. Current amplitudes (mean ± SEM) were acquired at − 80 and + 80 mV and plotted over time. **E** Representative I–V relationships of currents (at 300 s) illustrated in (**D**). **F** Bar graphs of outward currents (mean ± SEM; + 80 mV) shown in (D) at 300 s. *n*, number of cells measured; n.s., not significant; $*P<0.05$ $**P<0.01$; $***P<0.001$ (ANOVA, compared to WT). **G** Multiple sequence alignment (ClustalW) of amino acid sequences encoding the S6 and TRP segments in the mouse TRPM1 – 8 proteins. Grey background indicates the sequence consensus. N1097 and N1098 of TRPM7 are indicated in red

regulators of the ubiquitously expressed TRPM7 channel to correlate the uptake of essential metals with the metabolic state of the cell [1–3].

The molecular mechanism determining TRPM7 sensitivity to intracellular Mg^{2+} remains unclear. Previously, several research groups examined the role of the C-terminal kinase domain with regard to TRPM7 channel sensitivity to Mg^{2+} and obtained controversial results. Thus, deletion of the kinase domain resulted in either non-functional versions of the channel [14], channel variants with unchanged [15] or even increased sensitivity to free Mg^{2+} [5, 15, 16]. In other studies, the introduction of 'kinase-dead' point mutations (D1775A and K1648R) in the catalytic site of the kinase moiety or deletion of phosphorylation residues (S1511 and S1567) did not affect the responses of the channel to free Mg^{2+} [14, 17, 18]. However, other researchers observed that TRPM7 with 'kinase-dead' mutations (K1648R and G1799D) exhibited reduced responses to free Mg^{2+} [5, 13], whereas the T1482L mutation affecting a putative phosphorylation site in TRPM7 increased Mg^{2+} sensitivity of the channel [19]. While the reason for such inconsistencies remains unclear, the overall consensus is that functional TRPM7 channel variants with impaired kinase moiety retain the sensitivity to intracellular free Mg^{2+}, arguing that an additional Mg^{2+} regulatory domain must exist.

Other studies suggested that Mg^{2+} affects the TRPM7 channel indirectly, for instance, by interfering with the interaction of phosphatidylinositol 4,5-bisphosphate (PIP_2) and TRPM7, but the structural basis of such interference remains unknown [20–22]. More recently, high-resolution structures of a closed TRPM7 channel were resolved by cryo-electron microscopy (cryo-EM) [23]. However, structural rearrangements associated with the Mg^{2+}- and PIP_2-dependent opening of the TRPM7 channel were not identified in the structures available [23].

Here, we embark on extensive functional analysis, structural modelling and molecular dynamics simulations and propose that a pivotal Mg^{2+} regulatory site of TRPM7 is located within the lower channel gate. Our findings suggest that Mg^{2+} interacts directly with this protein segment and stabilizes TRPM7 in the closed state. In line with this model, we found that a point mutation introduced in the Mg^{2+} regulatory site abolishes the sensitivity of TRPM7 to physiological concentrations of intracellular Mg^{2+}.

Results

Search for amino acid residues involved in the Mg^{2+}-induced inhibition of TRPM7

Recently, several structures of TRPM channels were determined using cryo-EM [24–33]. The investigators noted that TRPM2, TRPM4, TRPM5 and TRPM8 harbour intra-subunit Ca^{2+}-binding sites formed by five negatively charged and polar residues in the S2 and S3 helices and the TRP segment (Suppl. Fig. S1) [24–33]. Interestingly, some of these residues are substituted in TRPM1, TRPM3, TRPM6 and TRPM7 (Suppl. Fig. S1), suggesting that the latter group of channels may contain a binding pocket for another ligand, for instance, Mg^{2+}. To test this hypothesis functionally, we exchanged E899, E903, N925, D928 and E1124 of TRPM7 to an uncharged alanine residue (A) or two structurally related acidic (D or E) and two polar residues (Q or N) (Fig. 1A).

In the pore domain formed by the S5 and S6 helices, the polar side chains of N1097 and N1098 appear to arrange the narrowest constriction in the lower gate of TRPM7 [23]. Since asparagine side chains frequently contribute to Mg^{2+}-binding sites in other channels [34, 35], we hypothesized that N1097 and N1098 could function as an Mg^{2+} recognition site in TRPM7. Accordingly, we produced versions of TRPM7 with modified amino acids at positions N1097 and N1098 (Fig. 1A). Finally, we introduced changes in Y1085 (Fig. 1A) since its side chain hydroxyl group is located in the upper channel gate and may potentially interact with Mg^{2+} [23]. Because of the exceptionally low efficiency of in vitro site-directed mutagenesis of untagged

mouse TRPM7 cDNA in the bicistronic pIRES2-EGFP vector, the functional impact of the introduced mutations was investigated using mouse TRPM7 with a C-terminal YFP tag in the pcDNA3.1 vector (see further details in "Materials and methods").

First, we studied whether the TRPM7 mutants can be activated in the absence of cytosolic Mg^{2+}, assuming that mutations with a specific impact on Mg^{2+}-dependent inhibition of the channel should not significantly affect current amplitudes and current–voltage (I–V) relationships of TRPM7 in such an experimental setting. To this end, we transiently transfected HEK293T cells with cDNAs encoding wild-type (WT) and mutant versions of TRPM7-YFP and conducted patch-clamp experiments with YFP-positive cells. Whole-cell currents were elicited by a voltage ramp protocol ranging from − 100 to + 100 mV and a standard Mg^{2+}-free internal solution (Fig. 1B, C). I–V relationships of WT currents exhibited characteristic features, such as tiny inward and large outward currents with a pronounced rectification and a reversal potential of about 0 mV (Fig. 1C). Accordingly, outward currents of TRPM7 variants were used to reliably quantify the effects of the mutations (Fig. 1B). Only six mutant variants (E903D, N1097Q, N1098A, N1098Q, N1098D and N1098E) displayed currents significantly different from endogenous currents in untransfected cells (Fig. 1B). In addition, I–V relationships of these mutant channels resembled those of WT currents (Fig. 1C). Consequently, only the latter six TRPM7 variants were selected for further analysis.

Next, we examined the channel activity of WT and mutant TRPM7 variants in the presence of relatively high levels of intracellular Mg^{2+}. As expected, the addition of free 2.3 mM $[Mg^{2+}]_i$ to the internal solution completely prevented the development of WT currents (Fig. 1D, F). Five channel variants (N1097Q, N1098A, N1098Q, N1098D and N1098E) displayed currents already after break-in, which were modestly reduced over time and exhibited typical I–V characteristics (Fig. 1F, D). In contrast, the E903D variant showed low activity under these experimental conditions (Fig. 1F). Hence, unlike other mutations, exchanges of asparagine residues located in the S6 segment and the TRP helix (Fig. 1G) resulted in active TRPM7 channels in the presence of $[Mg^{2+}]_i$. Consequently, we selected the N1097Q and N1098Q variants for a more detailed assessment.

Impact of N1097Q and N1098Q mutations on TRPM7 channel inhibition by $Mg^{2+}$and Ba^{2+}

To rule out a potential influence of the YFP tag on the functional analysis of TRPM7, we re-introduced the N1097Q and N1098Q amino acid exchanges into mouse TRPM7 cDNA inserted into the bicistronic pIRES2-EGFP vector [36, 37]. Immunofluorescent staining of HEK293T cells expressing WT and mutant versions of TRPM7 did not reveal differences in the subcellular distribution of the proteins (Suppl. Fig. S2).

Next, we performed patch-clamp experiments to examine the impact of N1097Q and N1098Q on the concentration-dependent suppression of the channel by free $[Mg^{2+}]_i$ (Fig. 2). The calculated IC_{50} value for WT currents was 0.47 mM (Fig. 2A, B). Currents in cells expressing TRPM7 carrying the N1097Q mutation were inhibited by $[Mg^{2+}]_i$ with an IC_{50} value of 3.74 mM (Fig. 2C, D). As $[Mg^{2+}]_i$ varies between 0.5 and 1.0 mM in most mammalian cells [41], these results suggest that, unlike the WT channel, the N1097Q variant remains active in the presence of physiological concentrations of Mg^{2+}. Remarkably, TRPM7 containing N1098Q was highly active after break-in and remained active over time in the presence of the whole range of $[Mg^{2+}]_i$ examined, thus precluding a reliable calculation of an IC_{50} value (Fig. 2E, F). These results indicate that the N1098Q mutation results in a constitutively active channel insensitive to physiological concentrations of intracellular Mg^{2+}.

Apart from Mg^{2+}, other divalent cations (Ba^{2+}, Ca^{2+} and Zn^{2+}) can suppress TRPM7 currents presumably through a common regulatory site [38]. Hence, we examined whether the N1097Q and N1098Q mutants interfered with the effects of free $[Ba^{2+}]_i$ (0.55 and 1 mM) on the TRPM7 channel variants (Figure S3). We observed that the WT TRPM7 channel was inactive in the presence of both concentrations of free $[Ba^{2+}]_i$ (Suppl. Fig. S3A). The N1097Q variant showed significantly reduced currents only after administration of 1 mM free $[Ba^{2+}]_i$ (Suppl. Fig. S3B), whereas the N1098Q channel remained unaffected under both experimental conditions (Suppl. Fig. S3C).

Effects of N1097Q and N1098Q mutations on TRPM7 channel suppression by Mg·ATP and Mg·GTP

Previously, extensive electrophysiological analyses revealed that free Mg^{2+} and Mg·ATP inhibit TRPM7, most likely through different ligand binding sites [12, 13]. Interestingly, the elevation of free Mg^{2+} levels increased the potency of Mg·ATP, suggesting that Mg^{2+} and Mg·ATP act synergistically on the TRPM7 channel [12, 13]. Therefore, to further verify the role of N1097Q and N1098Q, we compared the concentration-dependent inhibition of the TRPM7 channel variants by intracellular concentrations of Mg·ATP $[Mg{\cdot}ATP]_i$, in the presence of only 250 µM free $[Mg^{2+}]_i$. The physiological intracellular concentrations of ATP vary between 2 and 9 mM in most mammalian cells [39]. In a physiological saline solution, the apparent K_d of Mg·ATP

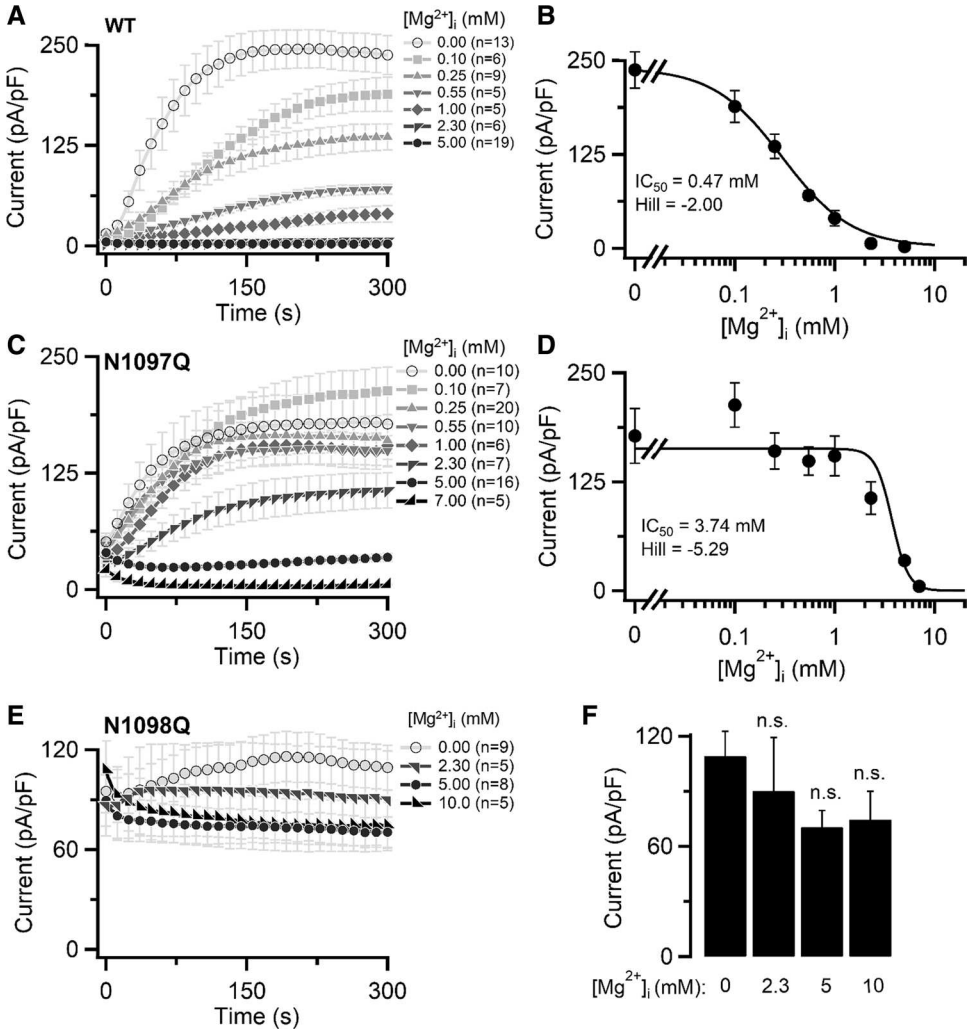

Fig. 2 Inhibition of TRPM7 currents by cytosolic Mg^{2+}. Whole-cell currents measured in HEK293T cells transfected by WT (**A, B**), N1097Q (**C, D**) and N1098Q (**E, F**) variants of TRPM7 cDNAs in pIRES2-EGFP expression vectors. **A**, **C**, **E** Current amplitudes (mean ± SEM) were measured at + 80 mV using internal solutions containing the indicated free $[Mg^{2+}]_i$ (Suppl. Table S1) and plotted over time. **B**, **D** Concentration-dependent suppression of currents (+ 80 mV, 300 s) shown in (**A**, **B**). The Hill equation was fitted to determine IC_{50} and the Hill factor. **F** Bar graphs of outward currents (mean ± SEM; + 80 mV) shown in (**E**) at 300 s. *n*, number of cells measured

is ~50 µM [40] and it was estimated that >90% of cytosolic ATP is present as Mg·ATP [41]. Using internal solutions covering this range of $[Mg{\cdot}ATP]_i$, we found that WT currents were suppressed with an IC_{50} value of 2.07 mM (Fig. 3A, B). By contrast, TRPM7 mutants N1097Q and N1098Q were characterized by a remarkably low sensitivity to $[Mg{\cdot}ATP]_i$ at all concentrations examined (Fig. 3C–F). Due to experimental limitations, $[Mg{\cdot}ATP]_i$ above 10 mM could not be reliably examined. Since other Mg·nucleotides (like Mg·GTP) were also capable of suppressing the TRPM7 channel, presumably through a mechanism shared with Mg·ATP [12, 13], we asked whether co-administration of 6 mM $[Mg{\cdot}GTP]_i$ and 250 µM free $[Mg^{2+}]_i$ will recapitulate the effects of 6 mM $[Mg{\cdot}ATP]_i$ co-applied with 250 µM free $[Mg^{2+}]_i$ (Suppl. Fig. S4). We observed that the impact of the N1097Q and N1098Q mutations on the channel's response to both Mg·nucletides were not different in such experimental settings (Suppl. Fig. S4).

Next, we examined the effects of 9 mM $[Mg{\cdot}ATP]_i$ in the presence of the physiological range of $[Mg^{2+}]_i$ concentrations using an internal solution containing 550 µM and 1 mM free $[Mg^{2+}]_i$. We found that WT currents were entirely suppressed under these conditions (Fig. 3G, Suppl. Fig. S5). In contrast, N1097Q mutant TRPM7 channel currents developed in the presence of 550 µM free $[Mg^{2+}]_i$ (Fig. 3G), but were undetectable after application of 1 mM free $[Mg^{2+}]_i$ (Suppl. Fig. S5). These results suggest that the N1097Q channel variant remained sensitive to Mg·ATP, but only in the presence of high concentrations of free Mg^{2+}, in accord with the idea that Mg^{2+} and Mg·ATP independently interact with different TRPM7 channel sites [12, 13], and that the N1097Q mutation primarily affected the Mg^{2+} regulatory mechanism. The N1098Q variant was not suppressed in all experimental settings (Fig. 3E, Suppl. Fig. S5), indicating that the N1098Q mutation engendered a constitutively active channel variant.

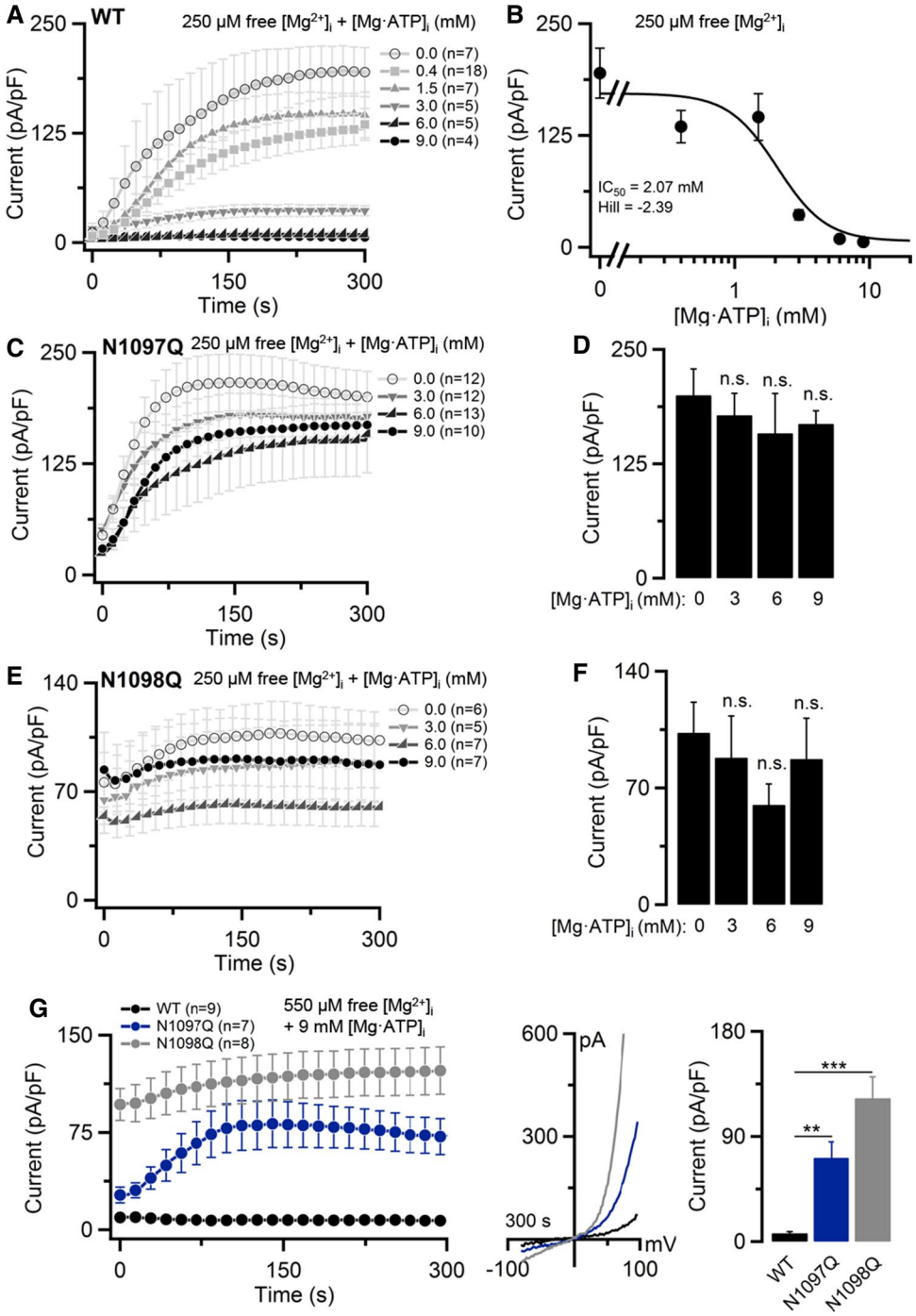

Fig. 3 Inhibition of TRPM7 currents by cytosolic Mg·ATP. Whole-cell currents measured in HEK293T cells transfected by WT, N1097Q and N1098Q variants of TRPM7 cDNAs (in pIRES2-EGFP). **A, B** Concentration-dependent suppression of WT TRPM7 by $[Mg{\cdot}ATP]_i$ in the presence of 250 µM free $[Mg^{2+}]_i$ (Suppl. Table S3). **A** Current amplitudes of the WT channel (mean ± SEM) measured at + 80mV were plotted over time. **B** Concentration–response curve for currents shown in **A** (+ 80 mV, 300 s). The Hill equation was used to determine IC_{50} and the Hill factor. **C–F** Effects of $[Mg{\cdot}ATP]_i$ on the N1097Q (**C**, **D**) and N1098Q (**E**, **F**) variants of TRPM7. Measurements were performed as in **A**. However, bar graphs of outward currents (mean ± SEM; + 80 mV) at 300 s were used to analyse the effects of $[Mg{\cdot}ATP]_i$. **G** Whole-cell currents were measured in the presence of 9 mM $[Mg{\cdot}ATP]_i$ and 550 µM free $[Mg^{2+}]_i$ (Suppl. Table S4). *Left panel* current amplitudes (mean ± SEM) acquired at + 80 mV were plotted over time. *Middle panel* representative current–voltage (I–V) relationships of currents (at 300 s) illustrated in the *left panel*. *Right panel* bar graphs of outward currents (mean ± SEM; + 80 mV) shown in the *left panel* at 300 s. *n*, number of cells measured; ns, not significant; $^{**}P < 0.01$, $^{***}P < 0.001$ (ANOVA)

Finally, we aimed to assess the activity of TRPM7 variants without manipulations of the cytosolic contents of Mg^{2+} and Mg·ATP using perforated patch recordings (Suppl. Fig. S6). Consistent with earlier studies [21], WT currents did not develop in this experimental setting, presumably because resting concentrations of Mg^{2+} and Mg·ATP are sufficient to inhibit TRPM7. On the contrary, channel activity of the N1097Q or N1098Q variants was well detectable (Suppl. Fig. S6), supporting the notion that the N1097Q or N1098Q mutations diminish the inhibitory

effects of both Mg^{2+} and Mg·ATP in resting HEK293T cells.

Effects of N1097Q and N1098Q on the sensitivity of TRPM7 to pharmacological agents and PIP_2 depletion

To determine whether the N1097Q or N1098Q amino acid exchanges altered the sensitivity of TRPM7 exclusively to $[Mg^{2+}]_i$ and $[Mg{\cdot}ATP]_i$ or caused more general changes of regulatory characteristics of the channel, we studied the effects of small synthetic molecules acting as activators or inhibitors of the TRPM7 channel. First, we assessed the action of naltriben, a potent agonist of the TRPM7 channel [42]. In these experiments, we used intracellular solutions containing 9 mM $[Mg{\cdot}ATP]_i$ and 550 µM free $[Mg^{2+}]_i$. The external application of naltriben led to a fast stimulation of WT and N1097Q currents (Fig. 4A, B). The N1098Q variant did not respond to naltriben (Fig. 4C).

Next, we examined the effect of NS8593, a potent TRPM7 inhibitor [43]. In these experiments, we induced currents using the standard $[Mg^{2+}]_i$-free intracellular pipette solution and externally applied NS8593 when currents were fully developed (Fig. 5). We noted that NS8593 caused a rapid inhibition of WT and N1097Q currents (Fig. 5A, B). In analogy to the effects of naltriben (Fig. 4A), the N1098Q mutation abolished the channel's sensitivity to NS8593 (Fig. 5C), indicating that the N1098Q mutant is functionally different from the N1097Q variant with regard to its sensitivity to natural or synthetic ligands.

It is well documented that depletion of plasma membrane PIP_2 results in the inactivation of the TRPM7 channel [20–22]. Therefore, we investigated the response of the TRPM7 variants to such a treatment using a voltage-sensitive phosphatase from *Ciona intestinalis* (Ci-VSP) [44]. Ci-VSP reduces PIP_2 levels in the plasma membranes at positive membrane potentials (Fig. 6A). A catalytically silent mutant of Ci-VSP (Ci-VSP-C363S) cannot hydrolyse PIP_2 and was used as a control (Fig. 6A). Cells co-expressing Ci-VSP or Ci-VSP-C363S together with TRPM7 variants were held at − 60 mV to allow induction of TRPM7 currents without activation of Ci-VSP. Then the regular voltage ramp ranging

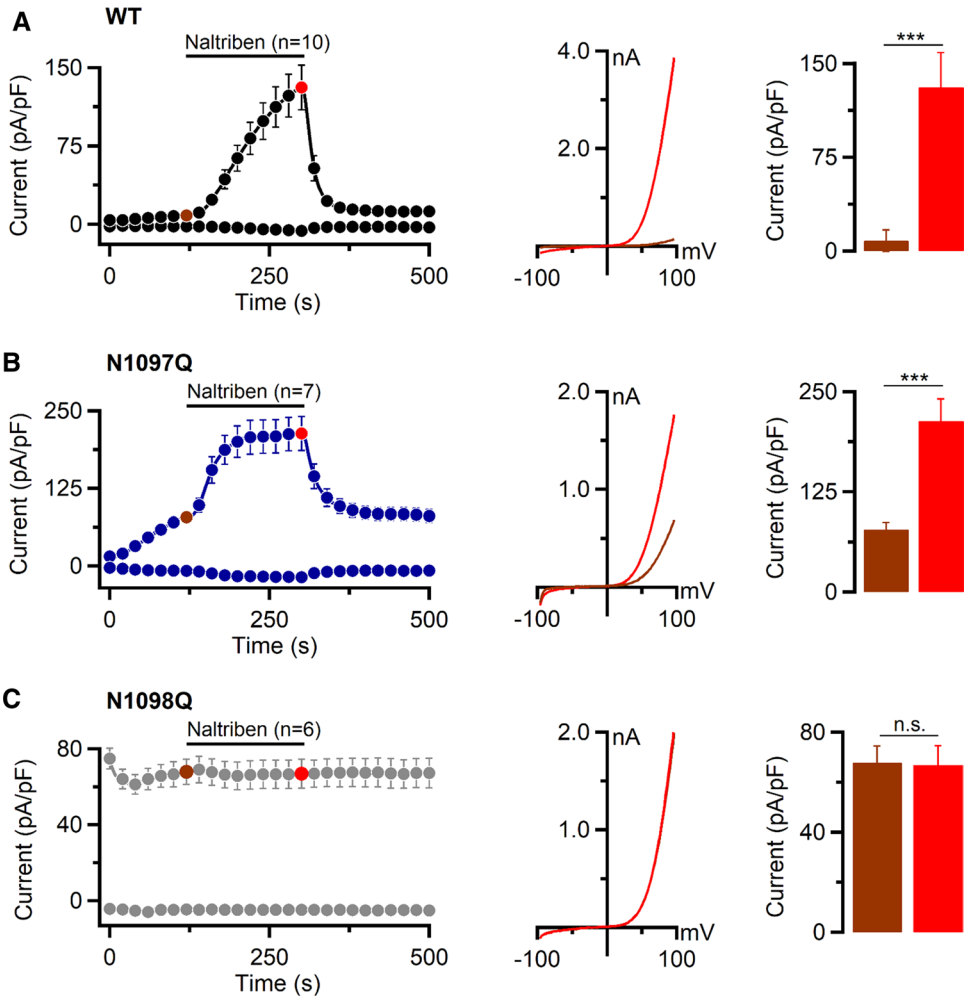

Fig. 4 Activation of TRPM7 currents by naltriben. Whole-cell currents were measured in HEK293T cells transfected by WT (**A**), N1097Q (**B**) and N1098Q (**C**) variants of TRPM7 cDNAs (in pIRES2-EGFP). *Left panels* current amplitudes (mean ± SEM) were measured at − 80 and + 80 mV and plotted over time. Currents were measured using an intracellular solution containing 9 mM $[Mg{\cdot}ATP]_i$ and 550 µM $[Mg^{2+}]_i$ and the standard external solution with or without 100 µM naltriben as indicated by the black bars. *Middle panels* representative I–V relationships obtained from individual ramps before (brown) and after (red) naltriben application as indicated in the *left panels* by coloured data points. *Right panels* bar graphs of outward currents (+ 80 mV, mean ± SEM) obtained before (brown) and after (red) naltriben application as indicated in the *left panels* by coloured data points. *n*, number of cells measured; ns, not significant; ***$P<0.001$ (two-tailed *t* test)

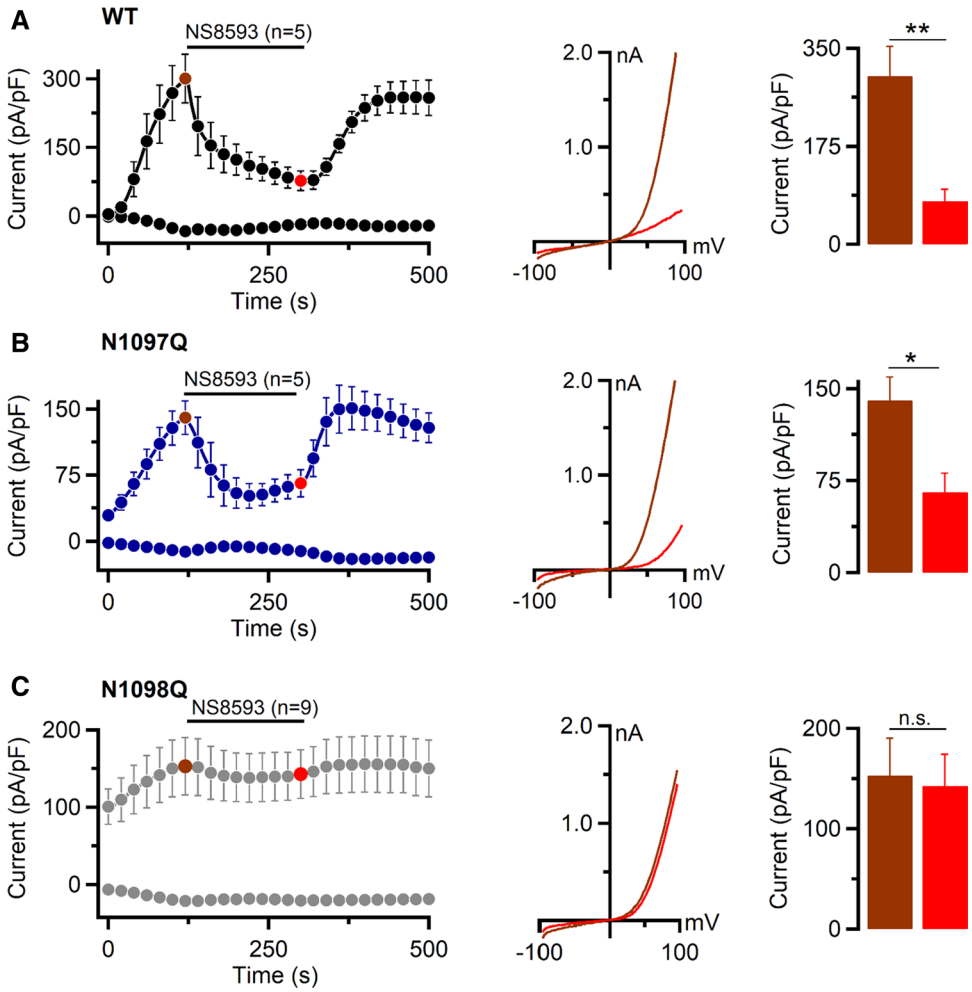

Fig. 5 Effects of NS8593 on TRPM7 currents. Whole-cell currents were measured in HEK293T cells transfected by WT (**A**), N1097Q (**B**), and N1098Q (**C**) variants of TRPM7 cDNAs (in pIRES2-EGFP) expressed in HEK293T cells. *Left panels* current amplitudes (mean ± SEM) were acquired at − 80 and + 80 mV and plotted over time. Currents were induced using the standard $[Mg^{2+}]_i$-free intracellular solution and the standard external solution. When currents were activated, the cells were exposed to the standard external solution with 10 µM NS8593 as indicated by the black bars. *Middle panels* representative I–V relationships obtained from individual ramps before (brown) and after (red) NS8593 application as indicated in the *left panels* by coloured data points. *Right panels* bar graphs of outward currents (+ 80 mV, mean ± SEM) obtained before (brown) and after (red) NS8593 application as indicated in the *left panels* by coloured data points. *n*, number of cells measured; ns, not significant; **P* < 0.05; ***P* < 0.01 (two-tailed *t* test)

from − 100 to + 100 mV was applied to activate Ci-VSP and record TRPM7 currents (Fig. 6B). We found that Ci-VSP, but not Ci-VSP-C363S, suppressed WT and N1097Q currents similarly (Fig. 6C, D). In contrast, N1098Q currents were not affected by Ci-VSP and Ci-VSP-C363S (Fig. 6E). Hence, the N1097Q channel resembles the WT channel in the sensitivity to naltriben, NS8593 and PIP_2 depletion by Ci-VSP, whereas the N1098Q variant represents a constitutively active channel insensitive to these agents.

Assessment of TRPM7 channel variants in a divalent cation-free (DVF) extracellular solution

A well-known characteristic feature of TRPM7 is the permeation block of the channel pore by extracellular divalent cations [12], causing the characteristic shape of the I–V relationship of TRPM7 currents in the presence of divalent cations in external solutions (Fig. 1C). However, exposure of TRPM7-expressing cells to a DVF solution abolish such a permeation block and entails large monovalent cation currents with a distinguishing semi-linearized I–V relationship [12]. We examined whether N1097Q or N1098Q would affect this channel feature. As illustrated in Suppl. Fig. S7, application of DVF solution to the WT channel caused rapid increases of outward and inward currents accompanied with expected alterations in the I–V relationships. After the removal of the DVF solution, this characteristic I–V relationship of TRPM7 was reversed. We also noted that the N1097Q or N1098Q variants recapitulated the response of WT TRPM7 (Suppl. Fig. S7), indicating that N1097Q or N1098Q did not impinge on the function of the ion selectivity filter of TRPM7.

Impact of N1097Q on TRPM7 characteristics in excised outside-out patches

For a more thorough examination of the hypothesis that the N1097Q mutation affected the sensitivity of TRPM7 to intracellular Mg^{2+}, we thought to analyse TRPM7 on the single-channel level. However, our extensive attempts to measure TRPM7 currents in inside-out patches were unsuccessful. Therefore, we used previously established experimental

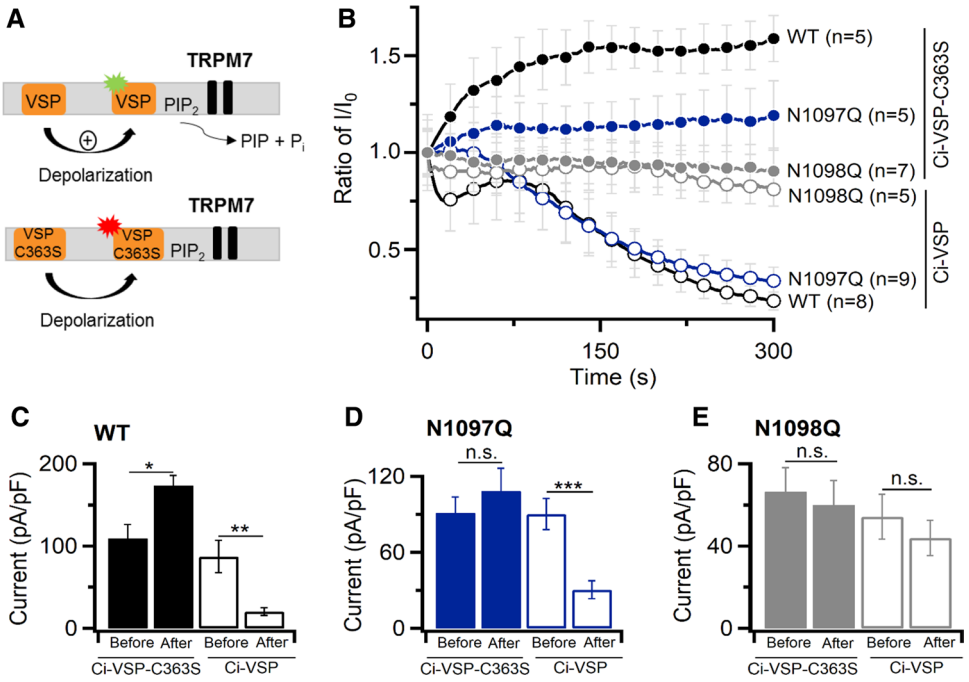

Fig. 6 Assessment of TRPM7 currents after PIP_2 depletion. **A** A diagram showing how wild-type voltage-sensitive phosphatase from *Ciona intestinalis* (Ci-VSP) reduces PIP_2 levels in the plasma membranes. A catalytically silent mutant of Ci-VSP (Ci-VSP-C363S) is unable to affect PIP_2 contents. **B** Time-dependent changes of normalized whole-cell outward currents in HEK293T cells transfected with WT, N1097Q and N1098Q variants of TRPM7 cDNA and Ci-VSP or Ci-VSP-C363S. Cells were held at − 60 mV for 2 min to allow induction of TRPM7 without activation of Ci-VSP. Then the voltage ramp ranging from − 100 to + 100 mV was applied to activate Ci-VSP and record TRPM7 currents. Current amplitudes (+ 80 mV) were normalized to the initial currents (mean ± SEM) and plotted over time. Data points are shown for every 10's ramp. *n*, number of cells measured. **C**–**E** Bar graphs of outward currents (+ 80 mV, mean ± SEM) shown in **B** immediately and after 300 s of application of voltage ramps from − 100 to + 100 mV. ns, not significant; $*P<0.05$; $**P<0.01$; $***P<0.001$ (two-tailed *t* test)

settings to analyse TRPM7 activity in excised outside-out patches [45]. To this end, outside-out patches were excised from transfected HEK293 cells and voltage clamped to − 60 mV. TRPM7 activity was evoked by exchanging the standard bath solution with a divalent cations-free (no-DIV) solution. This manoeuvre elicited only multichannel responses, irrespective of whether patches were from WT- or N1097Q-expressing cells, precluding an analysis of single-channel kinetics in these experimental settings (Suppl. Figure 8A, B). Nevertheless, differences between the WT and N1097Q channels were well evident. Single-channel amplitudes and the sojourns in the open state were about twice as large in the WT channels (Suppl. Fig. S8A, B). Estimated form a subset of experiments in which current–voltage relationships could be obtained, the calculated single-channel slope conductances (γ_s) were 41.4 ± 2.5 pS and 23.8 ± 2.4 pS for the WT and N1097Q, respectively [$n = 7$; see Suppl. Fig. S8C for examples; Suppl. Table S5 provides auxiliary chord conductance values (γ_c) from a larger sample]. The corresponding surrogate mean open times (T_{OS}), an admittedly rough estimate for the duration of the open state, were 4.7 ± 0.6 ms and 1.5 ± 0.3 ms for the WT and N1097Q channel variants, respectively. Despite shortening of T_{OS}, N1097Q did not affect the open probability (NP_O) (Suppl. Fig. S8C and Table S5), suggesting that the N1097Q mutation facilitated gating motions in the TRPM7 protein. Interestingly, besides a 40 pS main level, at least one additional subconductance state for TRPM7 has been described [46]. However, the all-points histograms derived from our data (Fig. 5A, C) showed evenly spaced peaks and lack of overt humps and, therefore, do not point to a significant contribution of such a subconductance state to the overall conductance under our experimental conditions.

To assess the effects of intracellular Mg^{2+} on channel characteristics, we used a pipette solution containing 1 mM free Mg^{2+}. All outside-out patches from cells overexpressing the WT channel exposed to no-DIV solution showed only an initial burst of channel openings followed by lasting quiescence (Fig. 7A, B). Single-channel current amplitudes assessed during the initial outbreaks of activity (− 2.3 ± 0.18 pA, Fig. 7A) were similar to those obtained in the absence of intracellular Mg^{2+} (− 2.2 ± 0.21 pA; Suppl. Fig. S8, Table S5). N1097Q behaved differently from the WT channel. Exposure to no-DIV solution induced sustained channel

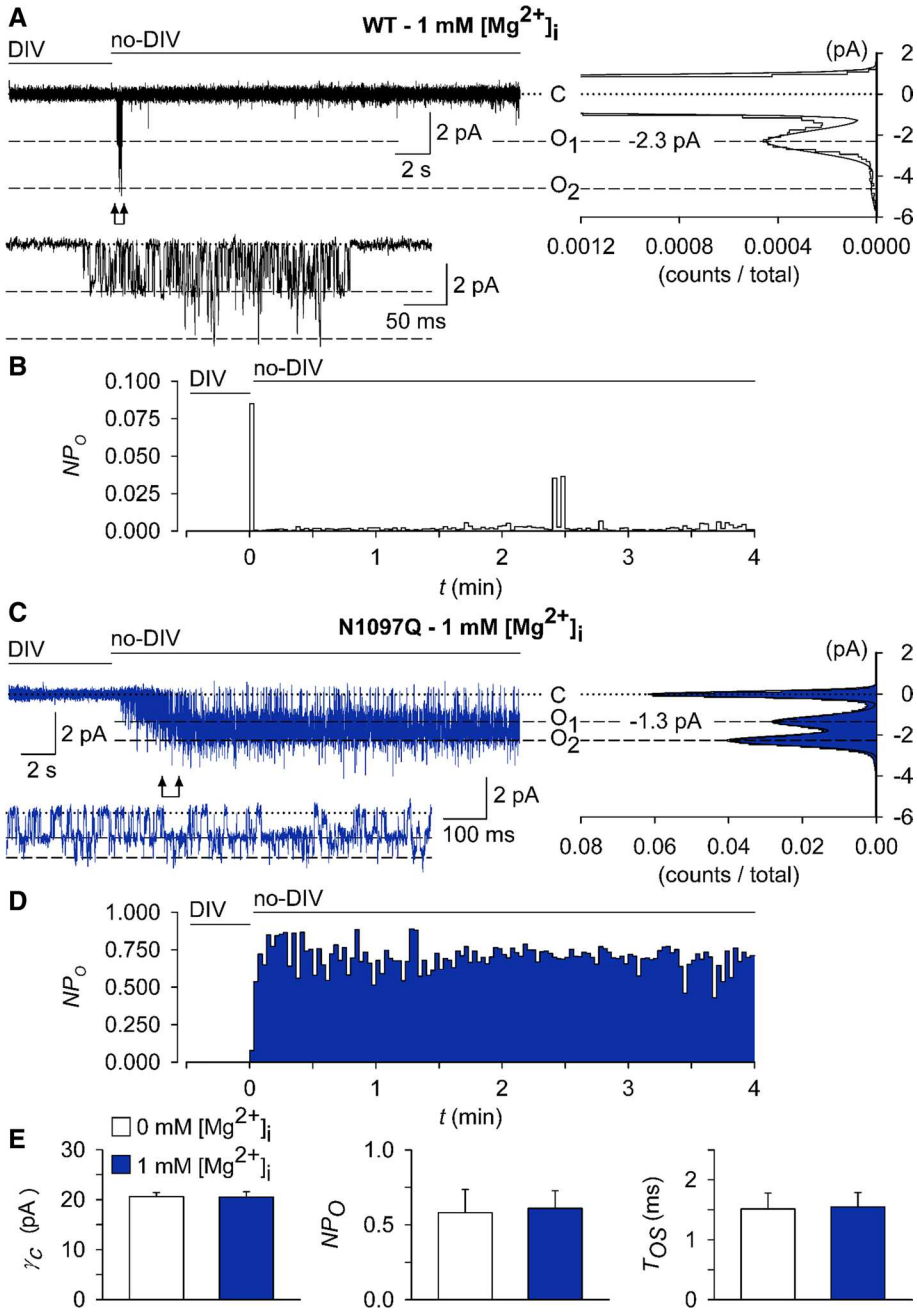

Fig. 7 Impact of intracellular Mg^{2+} on single-channel currents from TRPM7 variants. Currents were recorded at a holding potential of − 60 mV in outside-out membrane patches excised from HEK293 cells expressing WT (**A**, **B**) and N1097Q (**C**–**E**) variants of TRPM7. The WT (**A**) or N1097Q (**C**) channels were unblocked by removing the extracellular divalent cations (DIV bath) using a no-DIV solution, as indicated above the current traces. The intracellular solution was no-DIV augmented by 1 mM Mg^{2+}. Insets: currents on an expanded time scale from the segments indicated by arrows. The graphs on the right show all-point histograms from the two 30 s current traces. The dotted line indicates the closed level (**C**). The broken lines indicate the current level for one channel (*O1*) or two channels (*O2*) being open. Single-channel amplitudes (i) taken from O1 were − 2.3 pA and − 1.3 pA for WT channels (**A**) and N1097Q (**C**), respectively. **B**, **D** The open probabilities (NP_O) assessed for bins of 2 s over the whole 4.5 min duration of the experiments shown in (**A**, **C**). Note the different ordinate scaling in **B** and **D**. **E** Statistical evaluation of outside-out recordings with the N1097Q channel. Note that intracellular Mg^{2+} did not affect single-channel chord conductance (γ_c), NP_O and open time (T_{OS}; $n = 7$ each)

activity of the N1097Q variant, with the NP_O being stable over the whole time of current recordings (Fig. 7C, D). All measured channel characteristics, including chord conductance, NP_O, and T_{OS} were not affected by adding 1 mM intracellular Mg^{2+} (Fig. 7E, Table S5). Finally, using the same experimental settings, we analysed the effects of 2.9 mM $[Mg{\cdot}ATP]_i$ and 250 µM free $[Mg^{2+}]_i$ and observed that the WT channel exhibited only an initial burst of channel openings, whereas the N1097Q variant was active and displayed functional characteristics similar to those obtained in the presence of 1 mM free Mg^{2+} (Suppl. Fig. S9). These results corroborate with our analysis of whole-cell currents reinforcing the idea that the N1097Q substitution abrogated the inhibition of the TRPM7 channel by physiological intracellular Mg^{2+} concentrations.

Modelling and molecular dynamics (MD) simulations of the wild-type and mutant variants of the TRPM7 channel in closed and open conformations

To elucidate a mechanism by which N1097 and N1098 contribute to TRPM7 channel regulation, we opted for protein modelling and MD simulations of the TRPM7 ion

channel domain. The TRPM7 structure in Mg^{2+}-free conditions (PDB 5ZX5) showed the highest resolution of the S5–S6 segment in TRPM7, and, therefore, it was selected for analysis. To perform MD simulations, we constructed a 3D model of the closed channel pore-forming segment of TRPM7 (S4–S5 linker, S5–S6 helices and TRP domain) embedded in a lipid membrane and surrounded by water and ions (Fig. 8A). To develop a TRPM7 open channel structure, we used the homology modelling method. Initially, we attempted to use the open structure of the zebrafish TRPM2 channel as a template [32]. However, the open TRPM2 channel displayed significant conformational changes in the S5 helix driven by the interaction of charged residues in the S4–S5 linker and the TRP box, which are not conserved in TRPM7. Therefore, our analysis relied on the open structure of the human TRPV6 channel (PDB: 6BO8 [47]) (Suppl. Fig. S10).

The homology-modelled open channel structure then was used in targeted MD simulations to open the channel in lipid and water (Fig. 8). We observed that in the

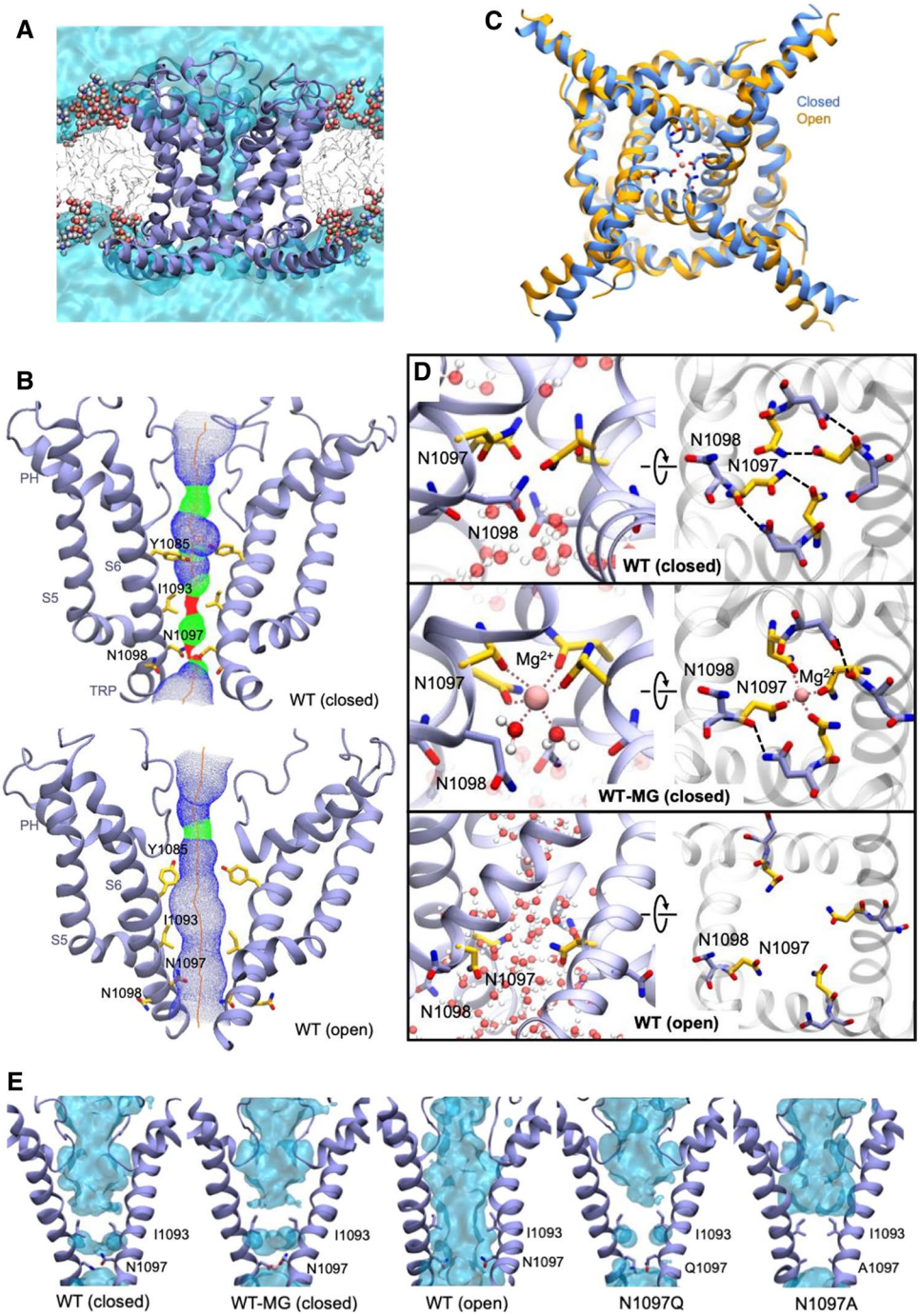

Fig. 8 Models of the channel pore-forming segment of mouse TRPM7 in lipid and water environments in closed and open conformations. **A** A representative structure of the mouse WT TRPM7 simulated channel unit (residues 982 to 1123) in the lipid bilayer and water. **B** A side view of a channel structure in the closed (top panel) and open (bottom panel) conformations. The channel pore-lining residues are shown. **C** Overlap of the closed structure an open structure shown (bottom view). **D** Structure of the channel gate in the closed channel with or without Mg^{2+} and open channel. Persistent water molecules are shown in red. Dashed lines indicate hydrogen bonds formed between N1097 and N1098 residues and Mg^{2+}. Note that the hydrogen bonds are transient, and the specific interactions shown are not present in all frames of the trajectory. **E** Channel's hydration in the simulations is shown for the WT, N1097A and N1097Q variants. Water is shown as a semi-transparent light blue continuum

closed state of the channel, the side chains of I1093 formed a hydrophobic seal excluding water from the channel (Fig. 8E), whereas polar side chains of N1097 build the narrowest segment of the cation permeation path in the pore (Fig. 8B). We found that transient inter-subunit hydrogen bonds were formed between N1097 residues of different subunits and between N1097 and N1098 residues. The most prominent hydrogen bonds were formed between the side chain amino and carbonyl groups of N1097 residues of adjacent subunits and between the side chain amino group of N1098 and the backbone carbonyl group of N1097 of adjacent subunits (Fig. 8D). On average, 3.6 inter-subunit hydrogen bonds involving N1097 and N1098 were present in the tetramer during the simulation (Suppl. Table S6). Our analysis suggests that these hydrogen bonds serve to stabilize the closed state of the channel gate (Fig. 8B, D).

MD simulation of TRPM7 in the open channel state revealed several remarkable structural rearrangements compared to the closed pore state (Fig. 8B, D). Specifically, we observed a loss of the hydrophobic seal formed by I1093 and significantly increased distance between the side chains of N1097. Inter-subunit hydrogen bonds formed by N1097 and N1098 were nearly absent with an average of 0.36 (Suppl. Table S6). Next, we performed MD simulations with Mg^{2+} placed in the pocket formed by the four N1097 in the closed channel (Fig. 8D). We found that Mg^{2+} steadily interacted with the side chain carbonyl groups of N1097 and two water molecules (Fig. 8C, D), stabilizing the closed state of TRPM7.

Finally, we performed MD simulations of the N1097A, N1097Q, N1098Q mutants. The N1097A channel formed a tightly closed gate due to the hydrophobicity of A1097 downstream to the hydrophobic seal formed by I1093 (Fig. 8E), thus explaining the silencing of the channel variant in patch-clamp experiments (Fig. 1). In the absence of Mg^{2+}, the N1097Q variant behaved similarly to the WT channel (Fig. 8E). However, MD simulations in the presence of Mg^{2+} revealed that Mg^{2+} lost coordination with three out of the four side chains of Q1097 (Suppl. Figure 11A), thus explaining the shift in concentration–response Mg^{2+} inhibition of the N1097Q channel (Fig. 2). The N1098Q presented a more complicated picture. In the absence of Mg^{2+}, the N1098Q mutation reduced the average number of inter-subunit hydrogen bonds formed by N1097 and Q1098 to only 0.6 as opposed to 3.6 in the WT structure (Suppl. Table S6, Suppl. Figure 11B). These results suggest that the closed state of the N1098Q channel is significantly less stable than the WT channel. In the presence of Mg^{2+}, the N1098Q channel retained coordination with Mg^{2+}, but the glutamine residue at position 1098 interacted weaker with N1097 than the WT channel (Suppl. Table S6). Hence, consistent with electrophysiological data, N1097 and N1098 have distinct structural roles in the lower channel gate of TRPM7.

Discussion

There is growing evidence to show that TRPM7 is a central gatekeeper of the cellular uptake of essential divalent cations and that cytosolic Mg^{2+} acts as the principal regulator of this fundamental process. In the present paper, we used a combination of site-directed mutagenesis, electrophysiological techniques and MD simulations to show that side chains of N1097 in mouse TRPM7 form an inter-subunit Mg^{2+}-regulatory site, determining the responses of the channel to changes of cytosolic Mg^{2+} levels. Hence, our study offers a molecular explanation of the key regulatory characteristic of the TRPM7 channel. The primary role of the lower channel gate in sensing the intracellular milieu has not been described yet in TRPM channels. Whether such a mechanism epitomizes a general principle among other TRP channels remains to be answered in the future.

The current view is that intracellular Mg^{2+} and Mg·ATP represent physiologically relevant negative regulators of the channel. Because TRPM7 contains a kinase unit, initial studies attempted to address the regulatory role of this domain [13–15, 21]. However, a kinase-dead point mutation (K1646R in mouse TRPM7) or channel variants lacking the C-terminal segments of the channel, including the kinase moiety, resulted in channels with only modestly changed sensitivity to Mg^{2+} [13–15, 21]. In contrast, the effects of Mg·ATP were dependent on the kinase moiety and upstream coiled-coil segments of TRPM7 in a species-specific fashion [13–15, 21]. These findings can be interpreted to mean that Mg^{2+} and Mg·ATP operate through different regulatory sites in TRPM7 and that Mg^{2+} blocks TRPM7 independently from the kinase domain.

In the present study, we uncovered the structural basis of the inhibitory action of free Mg^{2+} on the TRPM7 channel. Our hypothesis-driven assessment of TRPM7 variants with point mutations spanning different segments of TRPM7 suggests that the lower channel gate determines the Mg^{2+} sensitivity of TRPM7. Thus, a slight modification of the side chain of N1097 (N1097Q mutation) was sufficient to shift the IC_{50} value beyond physiological levels of free Mg^{2+}. Consequently, the N1097Q mutant was active in perforated patch-clamp recordings when the patch pipette solutions did not manipulate the intracellular Mg^{2+} levels. Interestingly, the N1097Q channel showed reduced sensitivity to free Ba^{2+}, implying that other divalent cations can potentially occupy the proposed Mg^{2+} binding site, thus, providing a mechanistic explanation for the inhibition of TRPM7 currents by Ba^{2+}, Ca^{2+} and Zn^{2+}

when applied in the mM range [38]. Significantly, N1097Q did not affect the current amplitudes of the channel in the absence of intracellular or extracellular Mg^{2+} and displayed unchanged I–V characteristics in all experimental settings used. The N1097Q mutant retained the sensitivity to pharmacological agents acting as negative and positive gating modulators of TRPM7, such as NS8593 and naltriben. Moreover, assessing the biophysical properties of the N1097Q mutant on the single-channel level corroborated our conclusion derived from whole-cell data, in that the mutant channel remains active in the presence of physiological concentrations of internal Mg^{2+}. Collectively, these results indicate that the N1097Q mutation selectively affects the inhibitory action of intracellular Mg^{2+} rather than perturbing TRPM7 function unspecifically.

Although the present study primarily aimed to reveal regulatory mechanisms of Mg^{2+}, our experiments also provide new insight into the action of PIP_2 and Mg·ATP on TRPM7. Thus, the N1097Q variant responded to PIP_2 depletion similarly to the WT channel. The latter finding is not surprising because the side chain of N1097 is exposed to the channel pore lumen and, consequently, incapable of interacting directly with membrane PIP_2. However, we observed that the N1097Q channel was sensitive to unphysiologically high Mg^{2+} concentrations suggesting that an additional action of Mg^{2+} was retained, for instance, the predicted electrostatic Mg^{2+} shielding of negatively charged PIP_2 [20–22]. Also, we observed that in the presence of relatively low Mg^{2+} levels (250 and 550 µM), the N1097Q variant exhibited a significantly reduced sensitivity to Mg·ATP (and Mg·GTP). However, the inhibitory effect of Mg·ATP on N1097Q currents was retained in the presence of 1 mM free Mg^{2+}. These results are consistent with a previous study [13], demonstrating that free Mg^{2+} and Mg·ATP can interact with TRPM7 causing the synergistic inhibition of TRPM7 currents. Accordingly, we suggest that the N1097Q mutation primarily affects the channel's response to free Mg^{2+}, while its sensitivity to Mg·ATP is still preserved.

MD simulations allowed us to interrogate the structural role of N1097 in opening of the TRPM7 channel. Our data suggest that the four side chains of N1097 in a TRPM7 tetramer form an inter-subunit cation-binding site and that the presence of Mg^{2+} in this pocket stabilizes the closed channel state. Accordingly, the lack of Mg^{2+} facilitates channel opening. In line with electrophysiological experiments, the N1097Q variant eradicates the coordination of Mg^{2+} in the lower channel gate due to the difference of one methylene group in the length of side chains of asparagine and glutamine, thus destabilizing the closed channel state in the presence of Mg^{2+}. Unlike N1097Q, a similar modification of an adjacent asparagine, N1098Q, resulted in a gain-of-function mutation completely offsetting the effects of Mg^{2+}, Ba^{2+}, Mg·ATP, Mg·GTP, PIP_2 and pharmacological agents. Such constitutive activity of the N1098Q channel resembles a previously isolated TRPM7 variant containing the point mutation S1107E in the TRP domain [42]. The S1107E channel was insensitive to physiological levels of free Mg^{2+}, PIP_2 and naltriben [42].

The structural role of N1098 is distinguishable from that of N1097. MD simulations suggest that N1098 forms inter-subunit hydrogen bonds stabilizing the closed state of the WT channel. Consequently, the N1098Q mutation most likely destabilizes such hydrogen bonds resulting in a constitutively active channel variant. The striking functional impact of N1098Q and the closely located S1107E further reinforce the notion that this segment of TRPM7 plays a crucial role in opening of the channel.

Previously, our structure–functional analysis of mouse TRPM7 identified the crucial role of E1047 in the cation selectivity filter of the channel [48]. Together with other researchers [23, 48, 49], we showed that the E1047Q variant of TRPM7 was essentially impermeable to divalent cations, supporting the idea that the side chain of E1047 forms an inter-subunit site that directly interacts with divalent cations entering the channel pore. To this end, the structural impact of E1047 in the cation selectivity filter resembles the role of N1097 in the lower channel gate of TRPM7, implying the channel function of TRPM7 primarily operates using two inter-subunit cation-binding sites interacting with extracellular and cytosolic divalent cations. Since N1097 and N1098 of mouse TRPM7 are conserved within the TRPM1/3/6/7 group of mammalian proteins (Fig. 1G), such a structure–function paradigm may be relevant for this subgroup of TRPM channels as a general principle.

Material and methods

Molecular biology and cell culture

Mouse TRPM7 (in pIRES2-EGFP vector) and TRPM7-YFP (in pcDNA3.1/V5-His TA-TOPO vector) were reported previously [36, 37]. Ci-VSP or Ci-VSP-C363S cDNAs (in pIRES2-EGFP) were provided by Joris Vriens, KU Leuven [50].

Point mutations in TRPM7 were introduced using the QuikChange system (Thermo Fisher Scientific) according to the manufacturer's protocol and verified by sequencing (Eurofins, Germany). Initially, we attempted to introduce the mutations outlined in Fig. 1A in the mouse TRPM7 cDNA in the bicistronic pIRES2-EGFP vector [36, 37]. However, we found that side-directed mutagenesis of this expression construct is highly inefficient and prone to errors likely due to cis-acting IRES sequence. Nevertheless, we could successfully conduct mutagenesis using the mouse TRPM7

with C-terminal YFP tag in pcDNA3.1 vector [36, 37] and, consequently, the primary functional assessment of TRPM7 variants (Fig. 1) was performed using the latter expression construct.

HEK293T cells were grown at 37 °C and 5% CO_2 in Dulbecco's modified Eagle's medium (DMEM, Sigma-Aldrich) supplemented with 10% foetal bovine serum (FBS, Thermo Fisher Scientific), 100 U/ml penicillin and 100 µg/ml streptomycin (P/S, Sigma-Aldrich). Cells ~60% confluence, 3 cm dish) were transiently transfected by 2 µg TRPM7 cDNAs using Lipofectamine 2000 reagent (Thermo Fisher Scientific). In some experiments, 2 µg TRPM7 cDNAs (pIRES2-EGFP) were co-transfected with 1 µg Ci-VSP WT or Ci-VSP-C363S cDNAs (pIRES2-EGFP) as indicated in the corresponding figure legend.

Immunofluorescent staining

HEK293T cells cultured on glass-bottom cell culture dishes (World Precision Instruments) were transiently transfected by 2 µg/dish WT or mutant variants of TRPM7 cDNA (in pIRES2-EGFP) and examined 18–24 h after transfection. Cells were washed twice with PBS, fixed with ice-cold methanol for 20 min at − 20 °C, and blocked for 1 h with 5% (v/v) BSA in PBS at room temperature. The mouse monoclonal anti-TRPM7 antibody (clone 2C7; 0.84 µg/ml; [51]) was applied. The secondary antibody (0.5 µg/ml) was goat anti-mouse IgG conjugated to Alexa Fluor 488 (Molecular Probes). Each incubation was performed in PBS containing 5% (v/v) normal goat serum for 1 h at room temperature, followed by triple washing with PBS. After the final washing, glass coverslips were placed on glass-bottom cell culture dishes using a mounting medium (DakoCytomation). Differential interference contrast (DIC) and Airyscan images of Alexa Fluor 488 were obtained with the confocal laser-scanning microscope LSM 880 AxioObserver (Carl Zeiss). We used a C-Apochromat 63x/1.2 W objective, 488 nm excitation wavelength and 493–630 nm filters, multi-line argon laser 458/488/514 nm and an Airyscan detector. The acquired images were analysed using the ZEN 3.0 SR software (Carl Zeiss).

Electrophysiological techniques

Patch-clamp experiments with HEK293T cells were performed 18–22 h after transfection as reported previously [37, 52] with a few modifications. Whole-cell currents were measured using an EPC10 patch-clamp amplifier and PatchMaster software (Harvard Bioscience). Voltages were corrected for a liquid junction potential of 10 mV. Currents were elicited by a ramp protocol from − 100 mV to + 100 mV over 50 ms acquired at 0.5 Hz and a holding potential of 0 mV. Inward and outward current amplitudes were extracted at − 80 mV and + 80 mV and were normalized to cell size as pA/pF. Capacitance was measured using the automated capacitance cancellation function of EPC10. Patch pipettes were made of borosilicate glass (Science Products) and had resistance 2–3.5 MΩ.

Unless stated otherwise, a standard extracellular solution contained (in mM): 140 NaCl, 2.8 KCl, 1 $CaCl_2$, 2 $MgCl_2$, 10 HEPES–NaOH and 11 glucose (all from Roth Industries), pH 7.2. Effects of NS8593 (Tocris) and naltriben (Tocris) were examined by adding the compounds to the standard extracellular solution. A divalent cation-free (DVF) extracellular solution contained (in mM) 140 NaCl, 2.8 KCl, 11 glucose, 10 Na-EDTA and 10 HEPES–NaOH, pH 7.2. For the experiment with TRPM7-YFP (Fig. 1), we used an extracellular solution contained (in mM): 140 NaCl, 2.8 KCl, 1 $CaCl_2$, 10 HEPES–NaOH, and 11 glucose (all from Roth Industries), pH 7.2. The standard Mg^{2+}-free intracellular ($[Mg^{2+}]_i$) pipette solution containing (in mM): 120 Cs·glutamate, 8 NaCl, 10 Cs-EGTA, 5 Cs-EDTA, 10 HEPES–CsOH, pH 7.2.

To obtain $[Mg^{2+}]_i$ and $[Mg{\cdot}ATP]_i$ concentration–response data, the intracellular pipette solutions were prepared as outlined in Suppl. Tables S1–S4. Concentrations of $[Mg{\cdot}ATP]_i$ and free $[Mg^{2+}]_i$ were calculated using the Maxchelator software (maxchelator.stanford.edu).

The concentration–response data were fitted (Prism 8.4.0) with the following equation:

$$E(c) = E_{\min} + (E_{\max} - E_{\min}) \times (1/(1 + (IC_{50}/c)^h)),$$

with E being the effect/current at a given concentration c of inhibitor; $E_{\min}$, the minimal effect/current; E_{max}, the maximal effect; IC_{50}, the half-maximal concentration; h, the Hill factor.

For perforated patch recordings, 320 µM amphotericin B (Sigma-Aldrich) was added to the internal solution containing (in mM): 120 monopotassium glutamate (Sigma-Aldrich), 8 NaCl, 1 $MgCl_2$, 10 HEPES–KOH, pH 7.2. Cells were held at − 60 mV for 2 min to ensure activation of TRPM7 currents, followed by the standard voltage ramp protocol.

Outside-out patch-clamp recordings with EGFP-positive HEK293 cells were performed the day after transfection with either the WT or the N1097Q mutant of TRPM7, using procedures described previously [45]. The standard extracellular solution contained in these experiments (in mM): 147 NaCl, 2 KCl, 1 $MgCl_2$, 2 $CaCl_2$, 13 D-glucose and 10 HEPES (~305 mOsm/l; pH 7.3 with NaOH). A divalent cation-free (no-DIV) solution was produced by omitting Ca^{2+} and Mg^{2+} and supplementing EGTA and EDTA (1 mM each). Patch pipettes had a resistance of 15–20 MΩ when filled with intracellular solutions. These were either identical with the

no-DIV saline or based on it but containing about 1 mM of free Mg^{2+} in addition (2.07 mM added $MgCl_2$). Baselines in the current traces were corrected and raw single-channel data was evaluated with the QuB program. The mean amplitudes (i) of TRPM7 single-channel currents (digitized at 20 kHz and filtered at 2 kHz) were thereby from all-points amplitude histograms fitted to a sum of multiple Gaussian distributions, with the number of components depending on the apparent number of active channels (N) in a given patch. The probability for N channels being open (NP_O) was, in turn, defined as the ratio of the area occupied by all the peaks for open channels to the total amplitude histogram (summation of the open and closed peaks). The unitary conductance (γ) of WT or mutant TRPM7 channels was either calculated from i as chord conductance (γ_c), assuming a reversal potential of zero mV or, for comparison, in some experiments also derived from the slope of respective current–voltage relationships (γ_s, slope conductance). In multichannel patches, like those usually obtained during this study, uncertainties concerning the "true" value of N, as well as the overlap of channel openings, precludes a detailed dwell time analysis.

To still allow for comparisons, such as between WT and N1097Q channels, the relation [53]:

$$T_{os} = \left(\sum_i L_i \, t_i \right) / \, \#O,$$

where t_i is the total time the outside-out currents dwelt on level L_i during the recording and $\#O$ is the total of the number of opening events, was used to estimate a surrogate mean open time (T_{OS}). To this end, channel openings were counted over a prolonged time (4 min) in the outside-out current recordings, using the 50% amplitude threshold criterion implemented in QuB. The dead time imposed was 200 µs (~1.2-fold of the filter rise time), thus excluding shorter events than this from the analysis.

Data are presented as means ± standard error of the mean (means ± SEM). Statistical comparisons (Prism 8.4.0 or SigmaPlot 14.0) were made using analysis of variance (ordinary one-way ANOVA) or two-tailed t test, as indicated in the figure legends. Significance was accepted at $P \leq 0.05$.

MD simulations

All MD simulations were carried out using the pmemd.cuda program of AMBER16 molecular dynamics package [54]. The Amber FF99SB–ILDN force field [55] for proteins was used for all simulations combined with Lipid14 model [56] for lipids and TIP3P model for water. All covalent bonds involving hydrogen atoms were constrained using SHAKE [57] to allow an integration time step of 2 fs. Langevin thermostat and Berendsen barostat were used to control temperature and pressure, respectively. All NPT simulations were carried out using anisotropic pressure scaling. Electrostatic interactions were calculated using particle mesh ewald (PME) method [58] as implemented in Amber, with a non-bonded cutoff distance of 8 Å. Periodic boundary conditions were applied in all directions. In order to maintain the integrity of the pore loop of the protein, backbone hydrogen bond distances in the pore helix (residues 1031–1043) were restrained between 2.6 Å and the initial value during all simulations. Post-processing of trajectories was carried out using CPPTRAJ [59] and VMD [60].

MD simulation setup

Residues 982–1123 (S4-S5 linker, S5 helix, pore loop, S6 helix, and TRP helix) of the cryo-EM structure of the closed TRPM7 channel (PDB: 5ZX5) was used as the starting structure for all simulations. The protein was embedded in a POPC lipid membrane and solvated in water using the CHARMM-GUI Membrane Builder [61]. Additional water molecules were added manually to solvate the ion channel pore. The system was prepared for simulations using the charmmlipid2amber.py script and the tleap program in AmberTools16 (www.ambermd.org). The protein N and C termini were capped with the neutral acetyl and amide groups, and the conserved disulfide bond between residues C1056 and C1066 was introduced. The system was neutralized with Na^+ and Cl^- ions. The final system contained 568 protein residues, 159 lipid molecules, 13,585 water molecules and neutralizing ions.

MD simulations of the closed TRPM7 channel

The prepared TRPM7 closed channel system was equilibrated as follows. First, a short minimization (6000 steps) was performed to remove clashes in the system. The system was then heated from 0.1 to 100 K in NVT ensemble and 100 K to 300 K in NPT ensemble, over 250 ps. The protein heavy atoms were restrained at their initial positions with a harmonic force constant (k) of 10 kcal mol^{-1} $Å^{-2}$ during the heating steps (residues 1050–1070 in the pore loop were not restrained in order to enforce the disulphide bond between C1056 and C1066). The system was equilibrated at 300 K in NPT ensemble for 35 ns while gradually decreasing restraints on the protein until only the C_α atoms were restrained with $k = 0.5$ kcal mol^{-1} $Å^{-2}$. The resulting system was used as the starting structure for the simulations with Mg^{2+} and N1097 mutant simulations (described in the following sections). All restraints on protein C_α atoms were removed except those on residues 1116–1123 of the TRP helix, and the closed channel was equilibrated in NPT ensemble for further 100 ns.

TRPM7 open channel conformation model

The S5, S6, and TRP helices and the S4–S5 linker (residues 982–1022 and 1071–1123) of the TRPM7 open channel were modelled in SWISS-MODEL [62] using the open channel structure of human TRPV6 channel (PDB ID: 6BO8) as a template. The target–template alignment for homology modelling was extracted from a multiple sequence alignment of the transmembrane and TRP regions of known TRPM and TRPV structures (TRPM7, TRPM4, TRPM2, TRPV1, TRPV3, TRPV6) performed using Clustal Omega at EMBL-EBI [63]. Residues 471–513 and 553–605 of PDB: 6BO8 was used to model the open structure of TRPM7.

MD simulations of the open channel

The homology model of the open TRPM7 channel was used to open the equilibrated closed channel by targeted MD simulations with simulated annealing. To open the channel, the C_α atoms of residues 982–1022 and 1071–1123 (S4–S5 and S5 helix, S6 and TRP helices) in the closed channel were harmonically restrained to the corresponding coordinates of the open homology model. Simulated annealing was performed in six steps as follows. In each step, (a) the system was equilibrated for 5 ns at 300 K, (b) heated to 350 K over 500 ps, (c) equilibrated at 350 K for 5 ns (or until RMSD of the targeted C_α atoms with respect to the reference structure was stable), and (d) cooled back to 300 K over 500 ps. Harmonic restraints were maintained throughout the process, increasing the force constant at the end of each step from 0.05, 0.1, 0.2, 1.0, 2.0 to 2.5 kcal mol^{-1} Å^{-2}. The restraints were then released gradually over a period of 25 ns and, finally, unrestrained simulations of the open model were carried out for over 200 ns.

MD simulations of the mutant TRPM7 variants

The partially equilibrated closed TRPM7 channel (see "MD simulations of the closed TRPM7 channel" section) was used to construct the mutants N1097Q, N1097A and N1098Q. Additionally, Mg^{2+} was placed between the residues at the 1097 position to obtain complexes of the wild type (WT-MG), and the N1097Q (N1097Q-MG) and N1098Q (N1098Q-MG) mutants with Mg^{2+}. The charge on Mg^{2+} was set to + 1.65. Each system was equilibrated using a protocol similar to that described in the previous section (MD simulations of the closed TRPM7 channel), except restraints on the protein C_α atoms were changed from $k = 10$ to 0.5 kcal mol^{-1} Å^{-2} in 20 ns. In WT-MG, N1097Q-MG and N1098Q-MG systems, the magnesium ion was restrained with the same force constant used to restrain the protein, and an additional equilibration step of 100 ns was carried out without restraints on the magnesium ion while maintaining restraints on the protein C_α atoms at $k = 0.5$ kcal mol^{-1} Å^{-2}. All systems were simulated for 100 ns with all restraints removed except the restraints on C_α atoms of residues 1116–1123.

Supplementary Information The online version contains supplementary material available at https://doi.org/10.1007/s00018-022-04192-7.

Acknowledgements We thank the Extreme Science and Engineering Discovery Environment (XSEDE) at the Pittsburgh Supercomputing Center for technical support (allocation TG-MCB180173). We thank Joanna Zaisserer, Lisa Pleninger and Anna Erbacher for their technical assistance.

Authors' contributions All authors read and approved the final manuscript. All authors contributed to the study conception and design as follows: conceptualization: VC, TG, MGK; funding acquisition, VC, TG, MGK, MS; experimental investigation, ES, CN, WN, ME, AR, ML; theoretical investigation, CN, MGK; formal analysis, SZ, MS, CN, MGK; writing—original draft preparation VC, TG, MGK; writing—review and editing, MS, SZ, WN, VC, TG.

Funding Open Access funding enabled and organized by Projekt DEAL. VC, MS, SZ and TG were supported by the Deutsche Forschungsgemeinschaft, TRR 152. TG was supported by Research Training Group 2338 (DFG). CN and MK were supported by grants from NSF 1818213, NSF 1563291, and NIH RO1NS083660.

Availability of data and materials All reagents and data generated or analysed during this study and its supplementary information files are available from the corresponding authors on request.

Declarations

Conflict of interests The authors declare that they have no conflict of interests.

Consent for publication Not applicable.

Ethics approval and consent to participate Not applicable.

References

1. Chubanov V, Mittermeier L, Gudermann T (2018) Role of kinase-coupled TRP channels in mineral homeostasis. Pharmacol Ther 184:159–176

2. Fleig A, Chubanov V (2014) Trpm7. Handb Exp Pharmacol 222:521–546
3. Bates-Withers C, Sah R, Clapham DE (2011) TRPM7, the Mg(2+) inhibited channel and kinase. Adv Exp Med Biol 704:173–183
4. Mittermeier L et al (2019) TRPM7 is the central gatekeeper of intestinal mineral absorption essential for postnatal survival. Proc Natl Acad Sci U S A 116(10):4706–4715
5. Schmitz C et al (2003) Regulation of vertebrate cellular Mg^{2+} homeostasis by TRPM7. Cell 114(2):191–200
6. Abiria SA et al (2017) TRPM7 senses oxidative stress to release Zn(2+) from unique intracellular vesicles. Proc Natl Acad Sci USA 114(30):E6079–E6088
7. Monteilh-Zoller MK et al (2003) TRPM7 provides an ion channel mechanism for cellular entry of trace metal ions. J Gen Physiol 121(1):49–60
8. Faouzi M et al (2017) The TRPM7 channel kinase regulates store-operated calcium entry. J Physiol 595(10):3165–3180
9. Kerschbaum HH, Cahalan MD (1999) Single-channel recording of a store-operated Ca^{2+} channel in Jurkat T lymphocytes. Science 283(5403):836–839
10. Prakriya M, Lewis RS (2002) Separation and characterization of currents through store-operated CRAC channels and Mg^{2+}-inhibited cation (MIC) channels. J Gen Physiol 119(5):487–507
11. Kozak JA, Kerschbaum HH, Cahalan MD (2002) Distinct properties of CRAC and MIC channels in RBL cells. J Gen Physiol 120(2):221–235
12. Nadler MJ et al (2001) LTRPC7 is a Mg·ATP-regulated divalent cation channel required for cell viability. Nature 411(6837):590–595
13. Demeuse P, Penner R, Fleig A (2006) TRPM7 channel is regulated by magnesium nucleotides via its kinase domain. J Gen Physiol 127(4):421–434
14. Matsushita M et al (2005) Channel function is dissociated from the intrinsic kinase activity and autophosphorylation of TRPM7/ChaK1. J Biol Chem 280(21):20793–20803
15. Jansen C et al (2016) The coiled-coil domain of zebrafish TRPM7 regulates Mg. nucleotide sensitivity. Sci Rep 6:33459
16. Ryazanova LV et al (2010) TRPM7 is essential for Mg(2+) homeostasis in mammals. Nat Commun 1:109
17. Ryazanova LV et al (2014) Elucidating the role of the TRPM7 alpha-kinase: TRPM7 kinase inactivation leads to magnesium deprivation resistance phenotype in mice. Sci Rep 4:7599
18. Kaitsuka T et al (2014) Inactivation of TRPM7 kinase activity does not impair its channel function in mice. Sci Rep 4:5718
19. Hermosura MC et al (2005) A TRPM7 variant shows altered sensitivity to magnesium that may contribute to the pathogenesis of two Guamanian neurodegenerative disorders. Proc Natl Acad Sci U S A 102(32):11510–11515
20. Runnels LW, Yue L, Clapham DE (2002) The TRPM7 channel is inactivated by PIP(2) hydrolysis. Nat Cell Biol 4(5):329–336
21. Kozak JA et al (2005) Charge screening by internal pH and polyvalent cations as a mechanism for activation, inhibition, and rundown of TRPM7/MIC channels. J Gen Physiol 126(5):499–514
22. Xie J et al (2011) Phosphatidylinositol 4,5-bisphosphate (PIP(2)) controls magnesium gatekeeper TRPM6 activity. Sci Rep 1:146
23. Duan J et al (2018) Structure of the mammalian TRPM7, a magnesium channel required during embryonic development. Proc Natl Acad Sci U S A 115(35):E8201–E8210
24. Ruan Z et al (2021) Structures of the TRPM5 channel elucidate mechanisms of activation and inhibition. Nat Struct Mol Biol 28(7):604–613
25. Duan J et al (2018) Structure of full-length human TRPM4. Proc Natl Acad Sci U S A 115(10):2377–2382
26. Autzen HE et al (2018) Structure of the human TRPM4 ion channel in a lipid nanodisc. Science 359(6372):228–232
27. Winkler PA et al (2017) Electron cryo-microscopy structure of a human TRPM4 channel. Nature 552(7684):200–204
28. Guo J et al (2017) Structures of the calcium-activated, non-selective cation channel TRPM4. Nature 552(7684):205–209
29. Yin Y et al (2019) Structural basis of cooling agent and lipid sensing by the cold-activated TRPM8 channel. Science 363(6430):9334
30. Diver MM, Cheng Y, Julius D (2019) Structural insights into TRPM8 inhibition and desensitization. Science 365(6460):1434–1440
31. Huang Y et al (2019) Ligand recognition and gating mechanism through three ligand-binding sites of human TRPM2 channel. Elife 8:e50175
32. Huang Y et al (2018) Architecture of the TRPM2 channel and its activation mechanism by ADP-ribose and calcium. Nature 562(7725):145–149
33. Zhang Z et al (2018) Structure of a TRPM2 channel in complex with Ca(2+) explains unique gating regulation. Elife 7:e36409
34. Mesbahi-Vasey S et al (2017) All atom NMDA receptor transmembrane domain model development and simulations in lipid bilayers and water. PLoS ONE 12(6):e0177686
35. Payandeh J, Pfoh R, Pai EF (2013) The structure and regulation of magnesium selective ion channels. Biochim Biophys Acta 1828(11):2778–2792
36. Chubanov V et al (2004) Disruption of TRPM6/TRPM7 complex formation by a mutation in the TRPM6 gene causes hypomagnesemia with secondary hypocalcemia. Proc Natl Acad Sci U S A 101(9):2894–2899
37. Ferioli S et al (2017) TRPM6 and TRPM7 differentially contribute to the relief of heteromeric TRPM6/7 channels from inhibition by cytosolic Mg(2+) and Mg. ATP. Sci Rep 7(1):8806
38. Kozak JA, Cahalan MD (2003) MIC channels are inhibited by internal divalent cations but not ATP. Biophys J 84(2 Pt 1):922–927
39. Traut TW (1994) Physiological concentrations of purines and pyrimidines. Mol Cell Biochem 140(1):1–22
40. Gupta RK et al (1983) Measurement of the dissociation constant of MgATP at physiological nucleotide levels by a combination of 31P NMR and optical absorbance spectroscopy. Biochem Biophys Res Commun 117(1):210–216
41. Romani AM (2011) Cellular magnesium homeostasis. Arch Biochem Biophys 512(1):1–23
42. Hofmann T et al (2014) Activation of TRPM7 channels by small molecules under physiological conditions. Pflugers Arch 466(12):2177–2189
43. Chubanov V et al (2012) Natural and synthetic modulators of SK (K (ca)2) potassium channels inhibit magnesium-dependent activity of the kinase-coupled cation channel TRPM7. Br J Pharmacol 166(4):1357–1376
44. Murata Y et al (2005) Phosphoinositide phosphatase activity coupled to an intrinsic voltage sensor. Nature 435(7046):1239–1243
45. Norenberg W et al (2016) TRPM7 is a molecular substrate of ATP-evoked P2X7-like currents in tumor cells. J Gen Physiol 147(6):467–483
46. Chokshi R, Matsushita M, Kozak JA (2012) Sensitivity of TRPM7 channels to Mg^{2+} characterized in cell-free patches of Jurkat T lymphocytes. Am J Physiol Cell Physiol 302(11):C1642–C1651
47. McGoldrick LL et al (2018) Opening of the human epithelial calcium channel TRPV6. Nature 553(7687):233–237
48. Mederos y Schnitzler M et al (2008) Evolutionary determinants of divergent calcium selectivity of TRPM channels. FASEB J 22(5):1540–1551

49. Li M et al (2007) Molecular determinants of Mg^{2+} and Ca^{2+} permeability and pH sensitivity in TRPM6 and TRPM7. J Biol Chem 282(35):25817–25830
50. Toth BI et al (2015) Regulation of the transient receptor potential channel TRPM3 by phosphoinositides. J Gen Physiol 146(1):51–63
51. Kollewe A et al (2021) The molecular appearance of native TRPM7 channel complexes identified by high-resolution proteomics. Elife 10:e68544
52. Chubanov V et al (2016) Epithelial magnesium transport by TRPM6 is essential for prenatal development and adult survival. Elife 5:e20914
53. Nemec J, Wickman K, Clapham DE (1999) Gbetagamma binding increases the open time of IKACh: kinetic evidence for multiple Gbetagamma binding sites. Biophys J 76(1 Pt 1):246–252
54. Case DA et al (2005) The Amber biomolecular simulation programs. J Comput Chem 26(16):1668–1688
55. Lindorff-Larsen K et al (2010) Improved side-chain torsion potentials for the Amber ff99SB protein force field. Proteins 78(8):1950–1958
56. Dickson CJ et al (2014) Lipid14: the amber lipid force field. J Chem Theory Comput 10(2):865–879
57. Hauptman HA (1997) Shake-and-bake: an algorithm for automatic solution ab initio of crystal structures. Methods Enzymol 277:3–13
58. Darden T et al (1999) New tricks for modelers from the crystallography toolkit: the particle mesh Ewald algorithm and its use in nucleic acid simulations. Structure 7(3):R55-60
59. Roe DR, Cheatham TE 3rd (2013) PTRAJ and CPPTRAJ: software for processing and analysis of molecular dynamics trajectory data. J Chem Theory Comput 9(7):3084–3095
60. Humphrey W, Dalke A, Schulten K (1996) VMD: visual molecular dynamics. J Mol Graph 14(1):33–38
61. Jo S, Kim T, Im W (2007) Automated builder and database of protein/membrane complexes for molecular dynamics simulations. PLoS ONE 2(9):e880
62. Waterhouse A et al (2018) SWISS-MODEL: homology modelling of protein structures and complexes. Nucleic Acids Res 46(W1):W296–W303
63. Madeira F et al (2019) The EMBL-EBI search and sequence analysis tools APIs in 2019. Nucleic Acids Res 47(W1):W636–W641

6.1 Supplementary figures publication 1

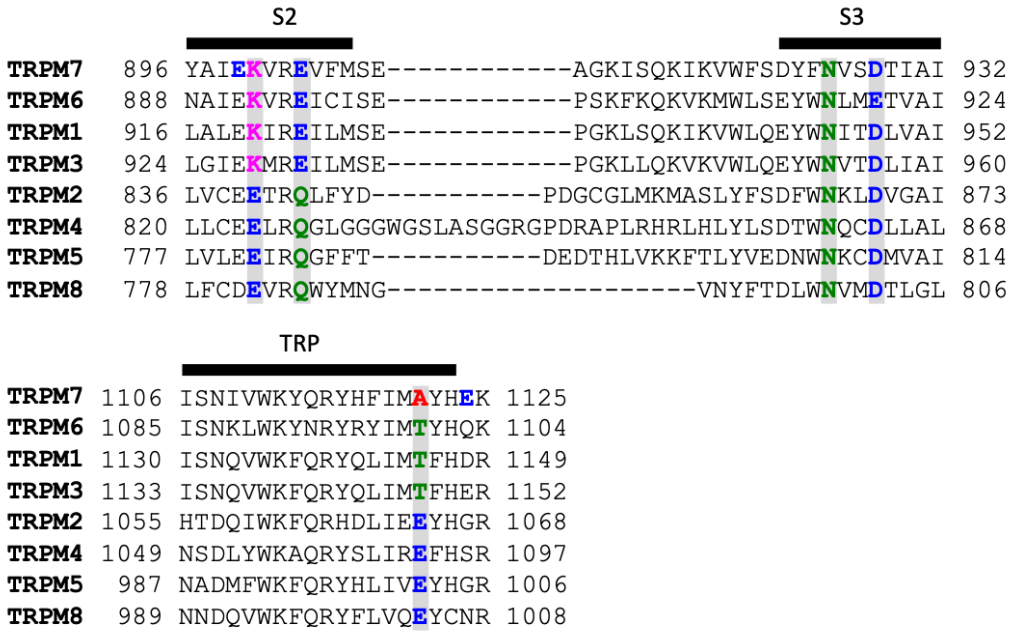

Suppl. Figure S1. Multiple sequence alignment of amino-acid sequences encoding the S2, S3 and TRP segments in the mouse TRPM1-8 proteins.

Conserved E, D, N and Q residues forming Ca^{2+}-binding pockets in TRPM2, TRPM4, TRPM5 and TRPM8 are labelled in green or blue and highlighted in grey. Note that these residues are only partially retained in TRPM7 as indicated accordingly.

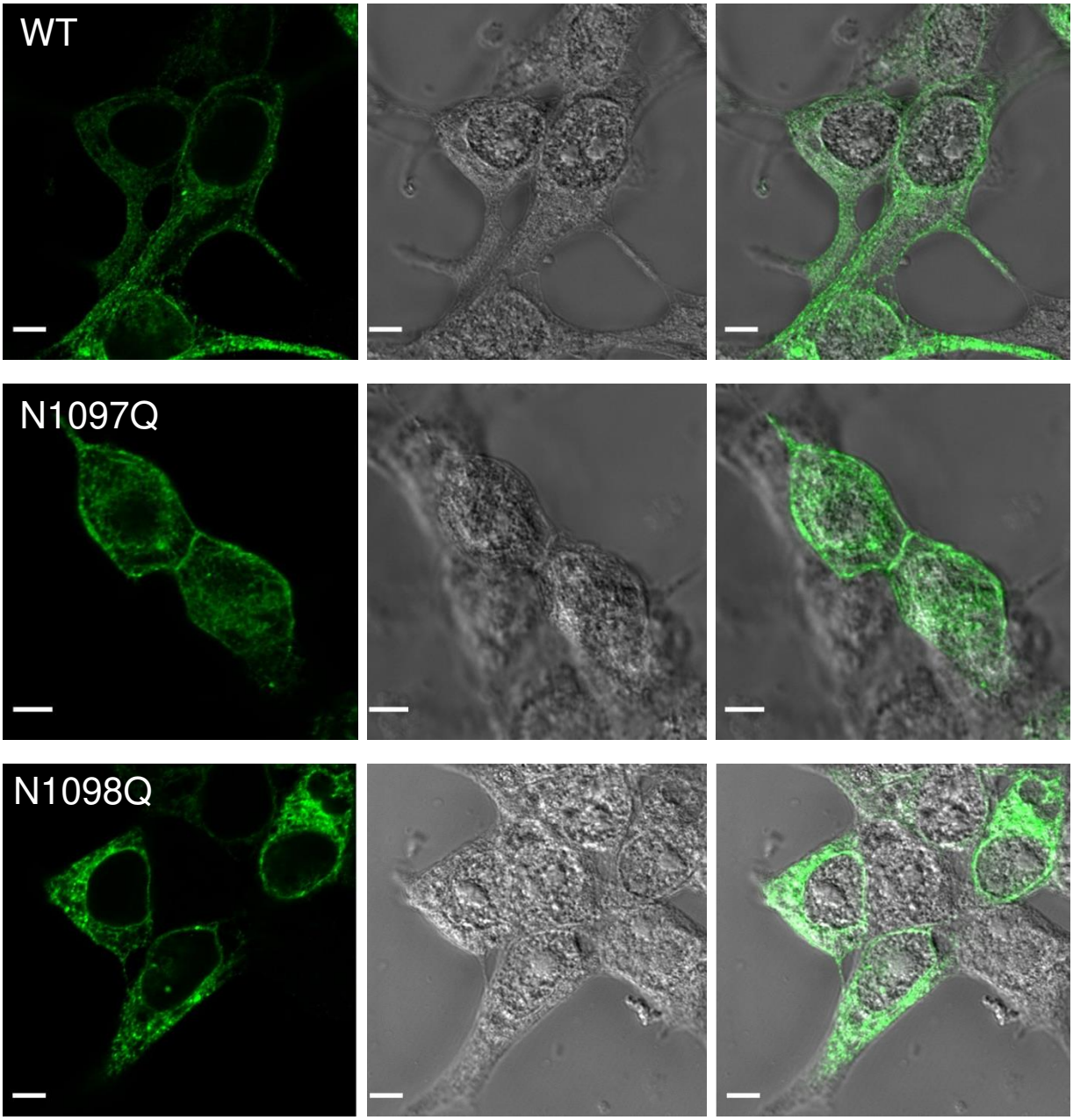

Suppl. Figure S2. *S*ubcellular localization of TRPM7 in HEK293T cells.

Mouse TRPM7 variants were transiently expressed in the indicated TRPM7 cDNA plasmid variants in HEK293T cells and immunolocalized using anti-TRPM7 and anti-mouse IgG- Alexa Fluor antibodies. Representative confocal images of Alexa Fluor 488 fluorescence (*Left panels*) and their overlay with corresponding DIC images (*Middle and Right panels*) are shown. *Scale bars* are 5 µm.

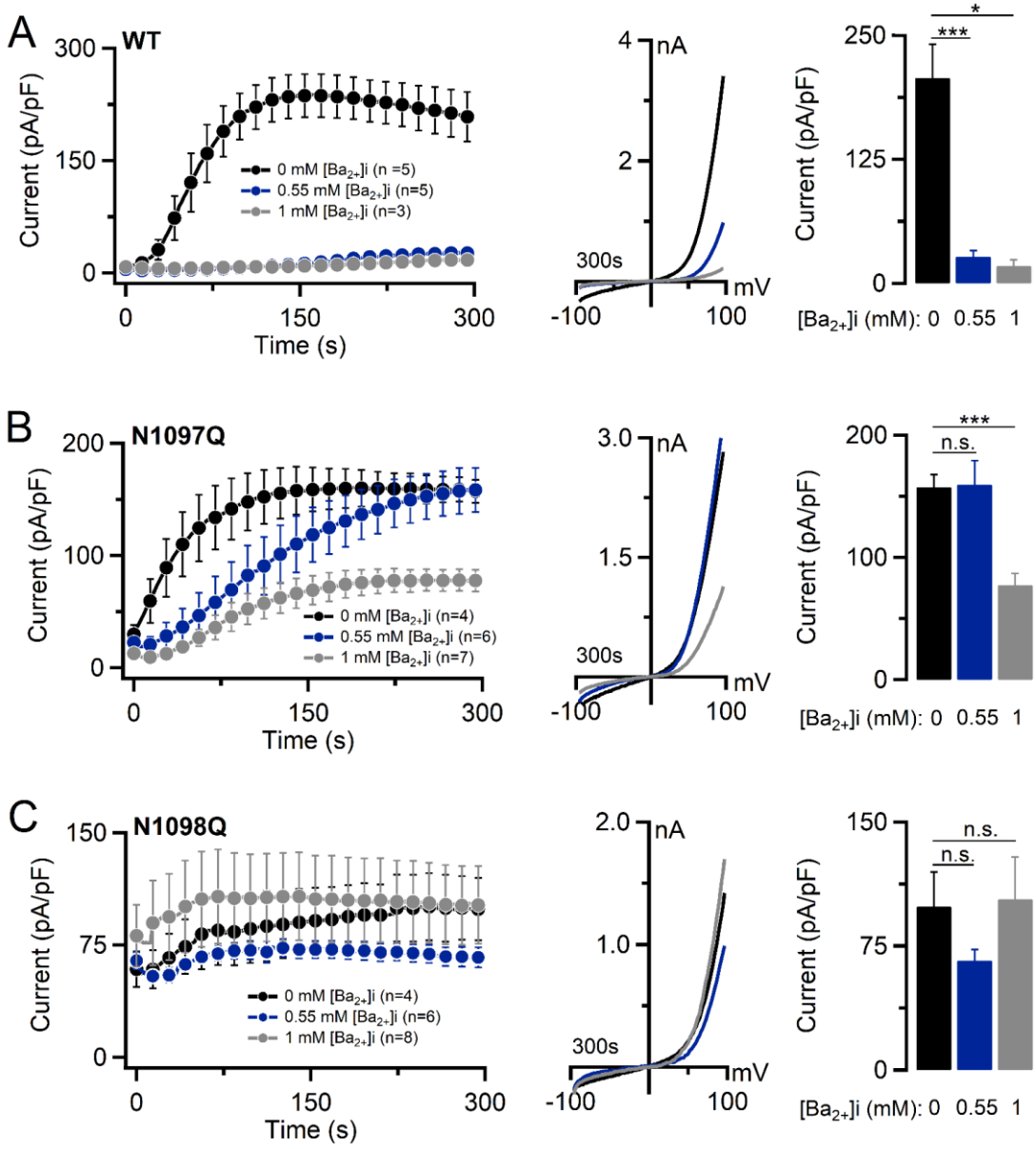

Suppl. Figure S3. Inhibition of TRPM7 currents by intracellular Ba^{2+}.

Whole-cell currents were measured in HEK293T cells transfected by WT (**A**), N1097Q (**B**) and N1098Q (**C**) variants of TRPM7 cDNAs (in pIRES2-EGFP). *Left panels:* Current amplitudes (mean ± SEM) were measured at -80 and +80 mV and plotted over time. Currents were measured using an intracellular solution containing the standard $[Mg^{2+}]_i$-free intracellular solution and solutions containing 0.55 and 1 mM free $[Ba^{2+}]_i$ (Suppl. Table S2). *Middle panels*: Representative I-V relationships obtained from individual ramps at 300 s in the *Left panels*. *Right panels*: Bar graphs of outward currents (+80 mV, mean ± SEM) obtained at 300 s as indicated in the *Left panels*. n, number of cells measured; n.s., not significant; ** P < 0.01, *** P < 0.001 (ANOVA).

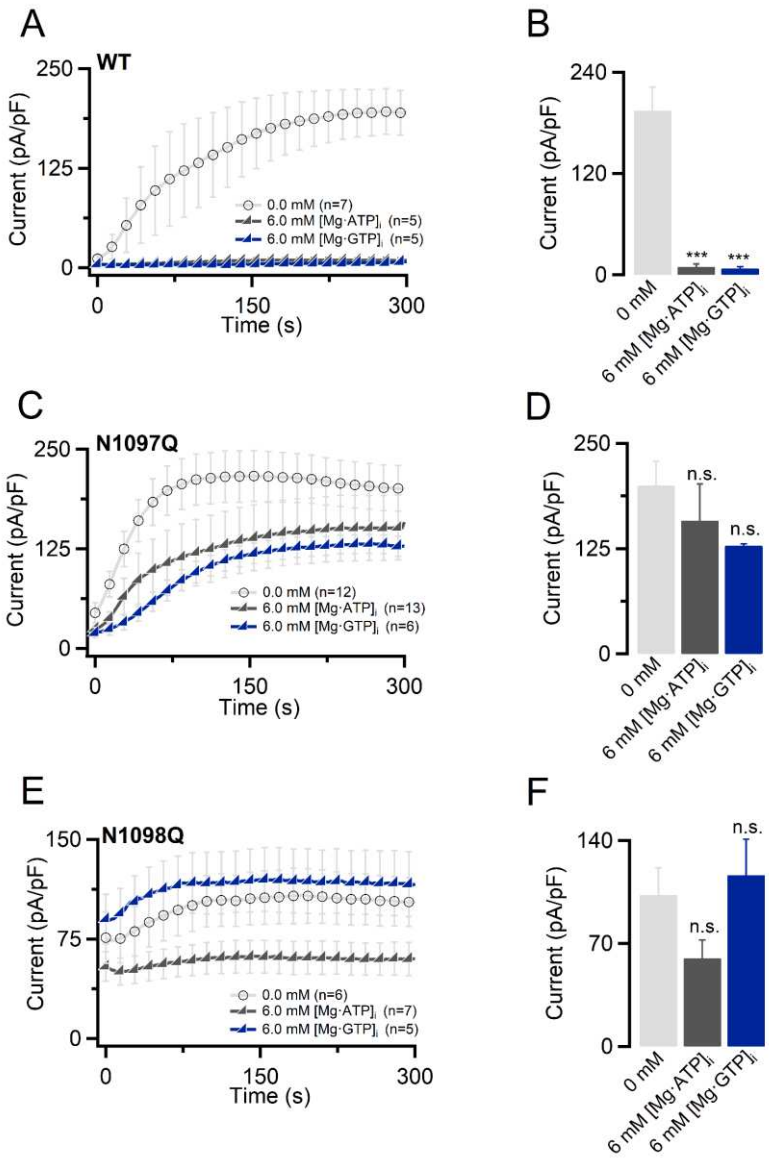

Suppl. Figure S4. Inhibition of TRPM7 currents by cytosolic Mg·ATP and Mg·GTP.

Whole-cell currents were measured in HEK293T cells transfected by WT (**A, B**), N1097Q (**C, D**) and N1098Q (**E, F**) variants of TRPM7 cDNAs (in pIRES2-EGFP). (A, C, D) Current amplitudes (mean ± SEM) were measured at -80 and +80 mV and plotted over time. Currents were measured using an intracellular solution containing 250 µM free $[Mg^{2+}]_i$ without Mg·nucleotides, 250 µM free $[Mg^{2+}]_i$ with 6 mM $[Mg{\cdot}ATP]_i$, and 250 µM free $[Mg^{2+}]_i$ with 6 mM $[Mg{\cdot}GTP]_i$ (Suppl. Table S3). (B, D, F) Bar graphs of outward currents (+80 mV, mean ± SEM) obtained at 300 s as indicated in (A, B, C). *Note:* The results obtained with 250 µM free $[Mg^{2+}]_I$ without Mg·nucleotides and with 6 mM $[Mg{\cdot}ATP]_i$ were taken from Fig. 3. n, number of cells measured; n.s., not significant; *** $P < 0.001$ (ANOVA).

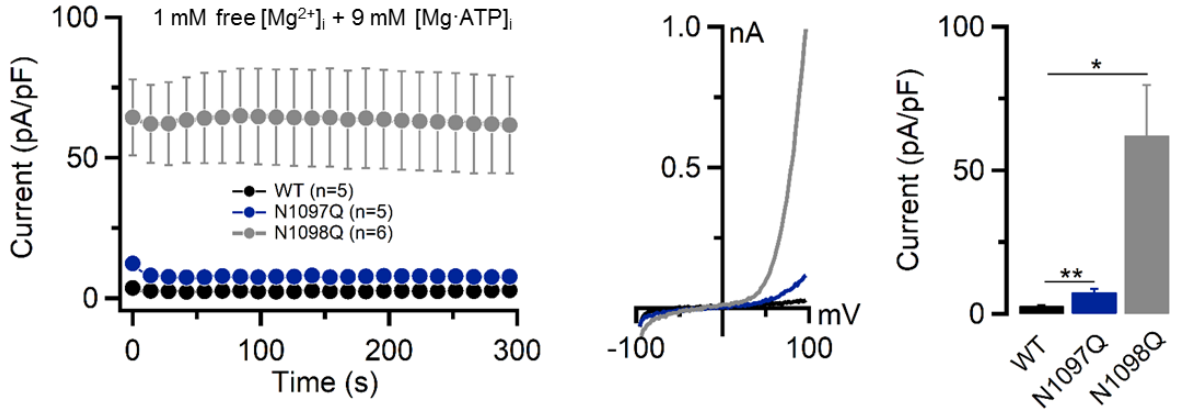

Suppl. Figure S5. Suppression of TRPM7 currents by 9 mM Mg·ATP in the presence of 1 mM free Mg^{2+}.

Whole-cell currents were measured and analysed analogously to the experiment outlined in Figure 3G, except that 9 mM $[Mg{\cdot}ATP]_i$ and 1 mM free $[Mg^{2+}]_i$ were included in the intracellular solution (Table S4). n, number of cells measured; n.s., not significant; * $P < 0.05$, ** $P < 0.01$ (ANOVA).

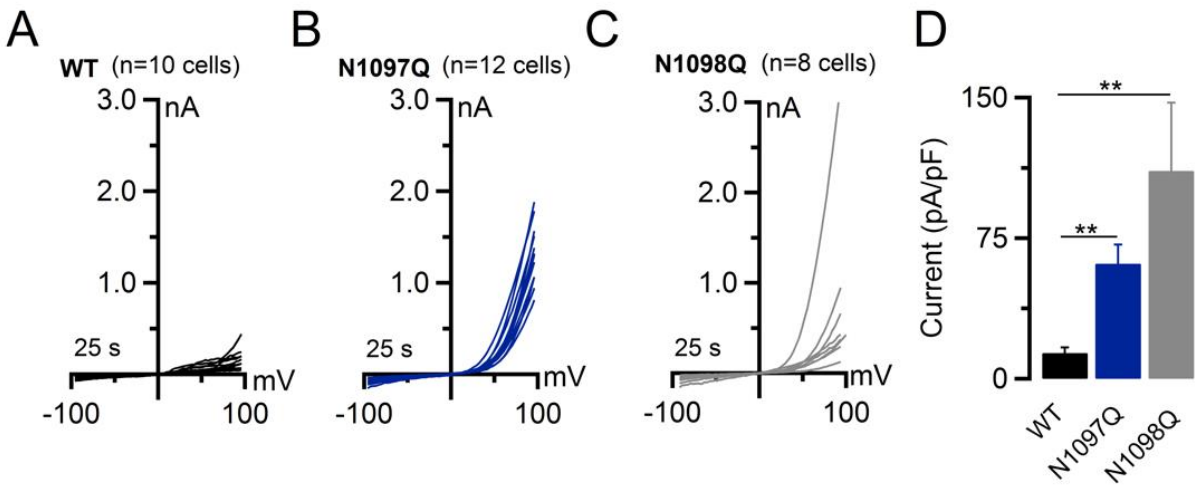

Suppl. Figure S6. Examination of TRPM7 currents in the perforated patch.

Current-voltage (I-V) relationships of currents were measured in HEK293T cells transfected by WT (**A**), N1097Q (**B**) and N1098Q (**C**) variants of TRPM7 cDNAs. The I-V relationships were acquired after 25 s of brake-in using the standard intracellular solution containing 320 µM amphotericin B. (**D**) Bar graphs of outward currents (+80 mV, 25 s) shown in (A-C). n, number of cells measured; ** $P < 0.01$ (ANOVA).

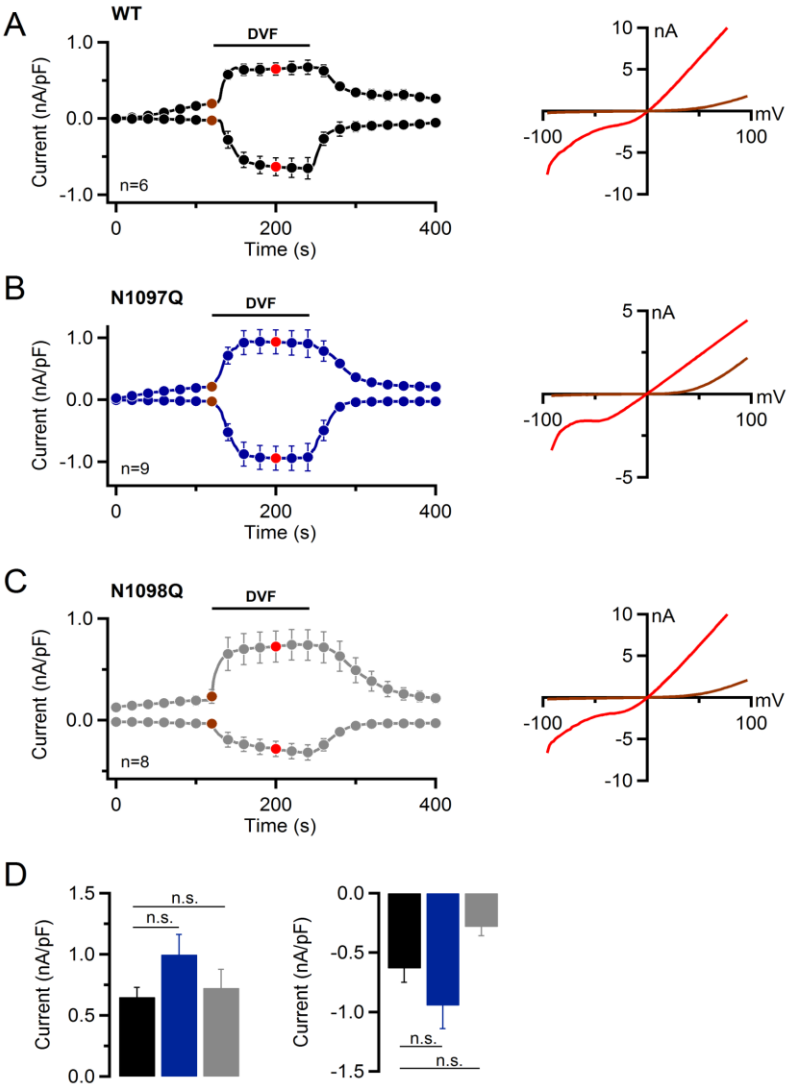

Suppl. Figure S7. Assessment of TRPM7 currents using a divalent cation-free (DVF) extracellular solution.

Whole-cell currents of WT (**A**), N1097Q (**B**) and N1098Q (**C**) TRPM7 variants (in pIRES2-EGFP) expressed in HEK293T cells. *Left panels:* Current amplitudes (mean ± SEM) were measured at -80 and +80 mV and plotted over time. Currents were induced using the standard $[Mg^{2+}]_i$ free intracellular solution and the standard external solution. When currents were fully activated, cells were perfused with the DVF solution as indicated by the black bars. *Right panels*: Representative I-V relationships obtained from individual ramps before (brown) and after (red) DVF application as indicated in the *Left panels* by coloured data points. (**D**) Bar graphs of outward (+80 mV; *Left panel*) and inward (-80 mV; *Right panel*) currents (mean ± SEM) shown in (A-C) at 200 s. n, number of cells measured; n.s., not significant (ANOVA).

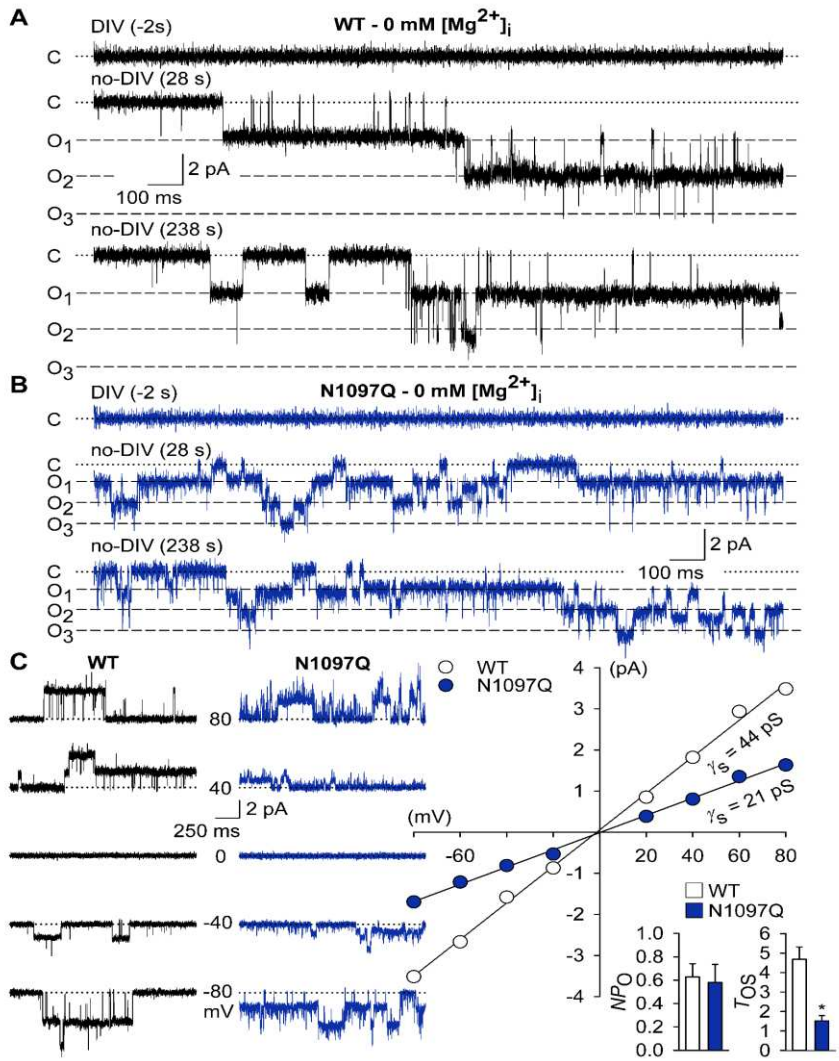

Suppl. Figure S8. Single-channel properties of the WT and N1097Q TRPM7 variants.

Currents were recorded in outside-out membrane patches excised from HEK293 cells expressing WT (**A, C**) and N1097Q (**B, C**) variants of TRPM7. The intracellular solution was no-DIV (0 mM Mg^{2+}). (A, B) Shown are current traces at a holding potential of -60 mV from WT (A) and N1097Q channels (B), starting (from top to bottom) 2 s before channels were unblocked by switching from a divalent cation-containing bath solution (DIV) to a divalent-free bath (no-DIV) and 28 s and 238 s after solution exchange. (C) The left panel shows representative current traces from the same patches as in (A) and (B), obtained at the indicated patch potentials in a no-DIV bath. The right panel shows a plot of unitary current amplitudes versus patch potential constructed thereof, revealing a linear I-V relationships. The slope conductance (γ_s) derived from linear regression fitting (R^2 = 0.997 and 0.997) was in these two outside-out patches 44 pS and 21 pS for WT and N1097Q channels, respectively. Insets: Statistical evaluation of outside-out recordings with the WT channel and N1097Q in the absence of intracellular Mg^{2+}. Note that the open probability (NP_O) was similar for the TRPM7 variants (P = 0.806), despite the significantly shorter open time (T_{OS}) of N1097Q (n = 7 cells, P = 0.002). The NP_O and T_{OS} data for N1097Q are taken from Fig. 7 and replotted here for comparison.

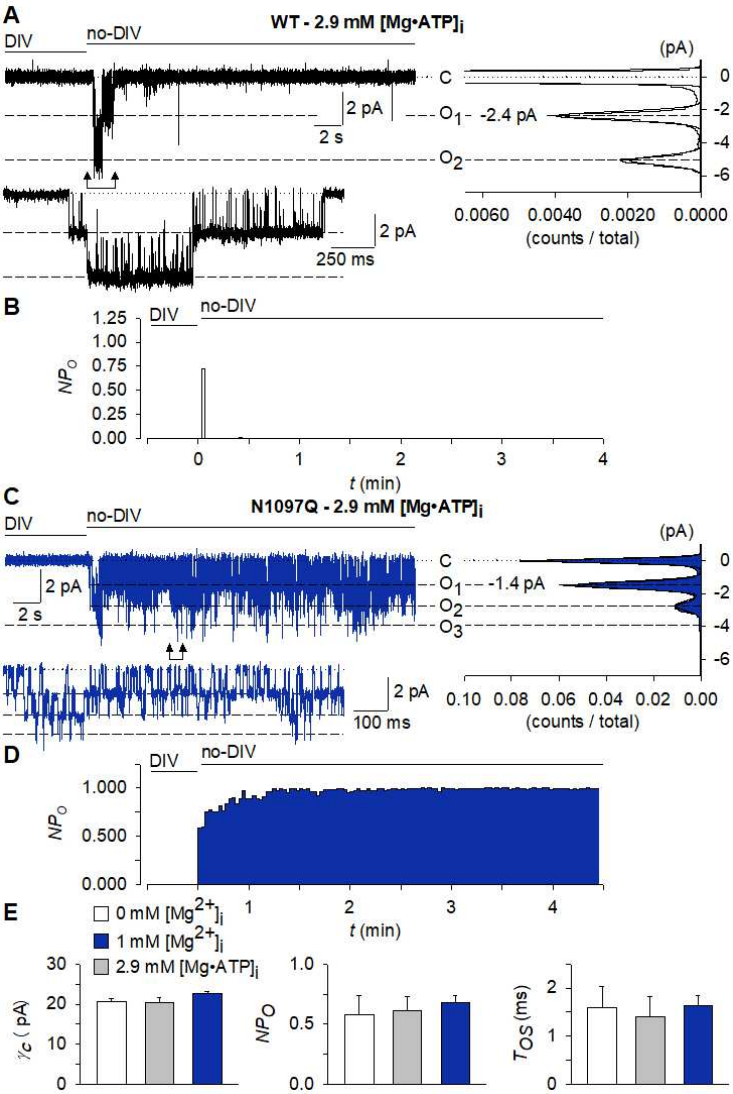

Suppl. Figure S9. Impact of intracellular Mg^{2+} and Mg·ATP on single-channel TRPM7 currents. Currents were recorded at a holding potential of -60 mV in outside-out membrane patches excised from HEK293 cells expressing WT (**A, B**) and N1097Q (**C-E**) variants of TRPM7. The WT (A) or N1097Q (C) channels were induced by removing the extracellular divalent cations (DIV bath) using a no-DIV solution, as indicated above the current traces. The intracellular solution was no-DIV containing 3 mM Mg·ATP and 0.5 mM $MgCl_2$, resulting in 2.9 mM $[Mg{\cdot}ATP]_i$ and 250 µM free $[Mg^{2+}]_i$. Insets: currents on an expanded time scale from the segments indicated by arrows. The graphs on the right show all-point histograms from the two 30 s current traces. The dotted line indicates the closed level (C). The broken lines indicate the current level for 1 channel (O_1), 2 channels (O_2) or 3 channels (O_3) being open. Single-channel amplitudes (*i*) taken from O_1 were -2.4 pA and -1.4 pA for WT channels (A) and N1097Q (C), respectively. (B, D) The open probabilities (NP_O) assessed for bins of 2 s over the whole 4.5 min duration of the experiments shown in (A, C). (E) Statistical evaluation of outside-out recordings with the N1097Q channel. The data obtained with 0 and 1 mM Mg^{2+} were replotted from Fig. 7. Note that intracellular Mg·ATP did not affect single-channel chord conductance (γ_c; P = 0.43, one-way ANOVA), NP_O (P = 0.91, one-way ANOVA) and open time (T_{OS}; n = 3 - 7; P = 0.925, one-way ANOVA).

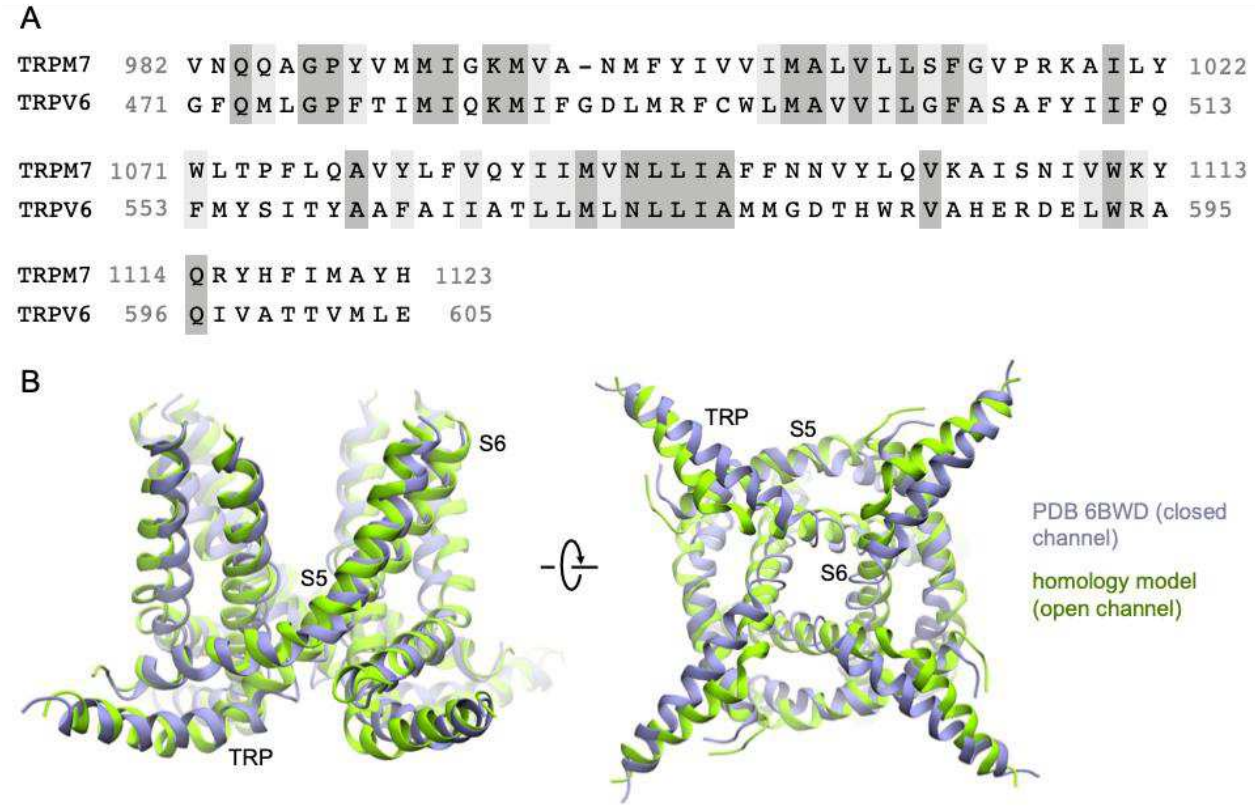

Suppl. Figure S10. Homology modelling of the S4-S5, S5, S6, and TRP domains of the open TRPM7 channel using the TRPV6 open channel as a template.

(**A**) Sequence alignment of residues 982-1022 and 1071-1123 of TRPM7, and residues 471 to 513 and 553 to 605 of the human TRPV6 open channel (PDB 6BO8). (**B**) Overlap of the homology model (green) and the cryo-EM structure of the closed TRPM7 (PDB 6BWD, blue)

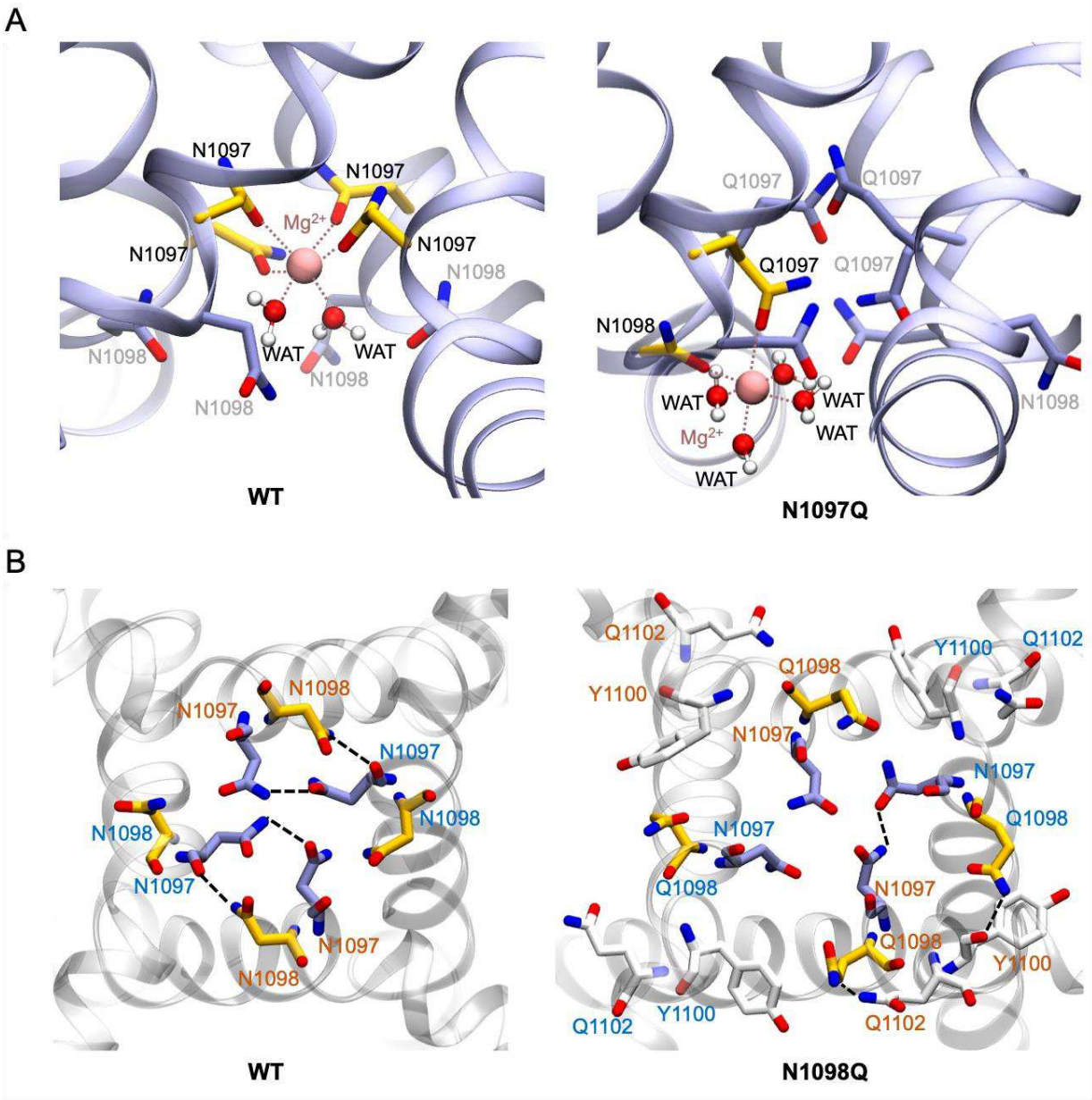

Suppl. Figure S11. The proposed arrangements of N1097 and N1098 in the lower channel gate of TRPM7.

(**A**) Comparison of the interaction of Mg^{2+} at the lower gate in simulated WT and N1097Q channels. Protein residues that interact with Mg^{2+} are shown in yellow. Water molecules (*WAT*) that interact with the Mg^{2+} ion are shown as red and white spheres. (**B**) Representative snapshots of WT and N1098Q channels displaying hydrogen bond interactions (dashed lines) of residue 1098 (yellow) viewed intracellularly. N1097 (blue) and other residues that interact with the mutated residue in at least one subunit (white) are shown. Residues in diagonal subunit pairs are labelled in different colours. Note that the hydrogen bonds are transient, and the specific interactions shown are not present in all frames of the trajectory.

6.2 Supplementary tables publication 1

Suppl. Table S1. Internal solutions used to study Mg^{2+} concentration-dependent inhibition of TRPM7 currents.

[a]Free $[Mg^{2+}]_i$ (mM)	Cs-glutamate (mM)	NaCl (mM)	Cs-HEPES (mM)	Cs-EGTA (mM)	$MgCl_2$ (mM)
0.10	140	8	10	10	0.16
0.25	120	8	10	10	0.38
0.55	120	8	10	10	0.83
1.00	120	8	10	10	1.50
2.30	120	8	10	10	3.40
5.00	120	8	10	10	7.10
7.00	120	8	10	10	9.67
10.0	120	8	10	10	13.56

[a]Free $[Mg^{2+}]_i$ was calculated using WebMaxC software.

Suppl. Table S2. Internal solutions used to study the effects of free $[Ba^{2+}]_i$ on TRPM7 currents.

[a]Free $[Ba^{2+}]_i$ (mM)	Cs-glutamate (mM)	NaCl (mM)	Cs-HEPES (mM)	Cs-EGTA (mM)	$BaCl_2$ (mM)
0.55	120	8	10	10	9.55
1.00	120	8	10	10	10.49

[a]Free $[Ba^{2+}]_i$ was calculated using WebMaxC software.

Suppl. Table S3. Internal solutions used to determine Mg·ATP concentration-dependent inhibition of TRPM7 currents.

[a][Mg·ATP]$_i$ (mM)	Free [b][Mg^{2+}]$_i$ (µM)	Cs-glutam. (mM)	NaCl (mM)	Cs-HEPES (mM)	Cs-EGTA (mM)	Cs-EDTA (mM)	Mg·ATP (mM)	$MgCl_2$ (mM)
0	250	140	8	10	10	3	0	0.38
0.4	250	120	8	10	10	3	0.57	3.19
1.5	250	120	8	10	10	3	2.15	2.71
3	250	120	8	10	10	3	4.30	2.10
4	250	120	8	10	10	3	5.70	1.70
5	250	120	8	10	10	3	7.10	1.28
6	250	120	8	10	10	3	8.55	0.85
9	250	120	8	10	10	3	12.4	-

[a,b][Mg·ATP]$_i$ and free [Mg^{2+}]$_i$ were calculated using WebMaxC software.

Suppl. Table S4. Internal solution containing of 9 mM [Mg·ATP]$_i$, and 0.55 or 1 mM [Mg^{2+}]$_i$.

[a][Mg·ATP]$_i$ (mM)	Free [b][Mg^{2+}]$_i$ (µM)	Cs-glutam. (mM)	NaCl (mM)	Cs-HEPES (mM)	Cs-EGTA (mM)	Cs-EDTA (mM)	Mg·ATP (mM)	$MgCl_2$ (mM)
9	550	140	8	10	10	3	10.7	2.10
9	1.00	140	8	10	10	3	9.9	3.55

[a, b][Mg·ATP]$_i$ and free [Mg^{2+}]$_i$ were calculated using WebMaxC software.

Suppl. Table S5. Biophysical properties of the WT and N1097Q channel variants obtained in outside-out recordings.

N: number of channels being simultaneously active in a given patch;
i: single channel amplitude at -60 mV;

	0 mM $[Mg^{2+}]_i$		1 mM $[Mg^{2+}]_i$
	WT (*n* = 7)	N1097Q (*n* = 7)	N1097Q (*n* = 7)
N	2 - 6	1 - 6	2 - 5
i (pA)	-2.2 ± 0.21	-1.3 ± 0.13*	-1.2 ± 0.09
γ_C (pS)	36.1 ± 3.46	20.6 ± 0.79*	20.5 ± 1.08
NP_O	0.63 ± 0.112	0.58 ± 0.156	0.61 ± 0.117
T_{OS} (ms)	4.7 ± 0.63	1.5 ± 0.30 *	1.6 ± 0.29

γ_C: single channel chord conductance at -60 mV (assuming a reversal potential of 0 mV in symmetrical Na^+);
NP_O: probability of being open simultaneously of the N^{th} channel;
T_{OS}: surrogate mean open time (product of NP_O and total recording time divided by the number of openings);
n: number of independent cells measured;
*: significant difference from WT.

Table S6. Interactions of residues 1097 and 1098 stabilizing the closed gate in simulated TRPM7 channels.

Simulated system	The average number of inter-subunit hydrogen bonds			Number of Residue 1097-Mg^{2+} interactions
	Res1097-Res1097	Res1097-Res1098	Total	
WT (closed)	1.61	2	3.61	-
WT-MG	0.17	1.94	2.11	4
WT (open)	0.09	0.27	0.36	-
N1097A	0	3.23	3.23	-
N1097Q	1.39	0.84	2.23	-
N1097-MG	1.81	1.42	3.23	1
N1098A	0.03	0	0.03	-
N1098D	0.1	0	0.1	-
N1098E	0.65	0.62	1.27	-
N1098Q	0.39	0.23	0.62	-
N1098Q-MG	0.83	0.72	1.55	4

7. Publication 2

Title: The molecular appearance of native TRPM7 channel complexes identified by high-resolution proteomics

https://elifesciences.org/articles/68544

https://doi.org/10.7554/eLife.68544.sa0

RESEARCH ARTICLE

The molecular appearance of native TRPM7 channel complexes identified by high-resolution proteomics

Astrid Kollewe[1†], Vladimir Chubanov[2†], Fong Tsuen Tseung[2], Leonor Correia[2], Eva Schmidt[2], Anna Rössig[2], Susanna Zierler[2,3], Alexander Haupt[1], Catrin Swantje Müller[1], Wolfgang Bildl[1], Uwe Schulte[1,4], Annette Nicke[2], Bernd Fakler[1,4]*, Thomas Gudermann[2,5]*

[1]Institute of Physiology II, Faculty of Medicine, University of Freiburg, Freiburg, Germany; [2]Walther-Straub Institute of Pharmacology and Toxicology, LMU Munich, Munich, Germany; [3]Institute of Pharmacology, Johannes Kepler University Linz, Linz, Austria; [4]Signalling Research Centres BIOSS and CIBSS, Freiburg, Germany; [5]German Center for Lung Research, Munich, Germany

Abstract The transient receptor potential melastatin-subfamily member 7 (TRPM7) is a ubiquitously expressed membrane protein consisting of ion channel and protein kinase domains. TRPM7 plays a fundamental role in the cellular uptake of divalent cations such as Zn^{2+}, Mg^{2+}, and Ca^{2+}, and thus shapes cellular excitability, plasticity, and metabolic activity. The molecular appearance and operation of TRPM7 channels in native tissues have remained unresolved. Here, we investigated the subunit composition of endogenous TRPM7 channels in rodent brain by multi-epitope affinity purification and high-resolution quantitative mass spectrometry (MS) analysis. We found that native TRPM7 channels are high-molecular-weight multi-protein complexes that contain the putative metal transporter proteins CNNM1-4 and a small G-protein ADP-ribosylation factor-like protein 15 (ARL15). Heterologous reconstitution experiments confirmed the formation of TRPM7/CNNM/ARL15 ternary complexes and indicated that complex formation effectively and specifically impacts TRPM7 activity. These results open up new avenues towards a mechanistic understanding of the cellular regulation and function of TRPM7 channels.

***For correspondence:** bernd.fakler@physiologie.uni-freiburg.de (BF); Thomas.Gudermann@lrz.uni-muenchen.de (TG)

†These authors contributed equally to this work

Competing interest: The authors declare that no competing interests exist.

Funding: See page 22

Received: 18 March 2021
Preprinted: 09 July 2021
Accepted: 08 November 2021
Published: 12 November 2021

Reviewing Editor: László Csanády, Semmelweis University, Hungary

Editor's evaluation

This work will be interesting to people studying TRP family ion channels and more generally, cellular ion homeostasis. It is the first to identify interacting protein partners of the cation channel TRPM7, a key regulator of cellular Mg^{2+} and Zn^{2+} homeostasis, and reveals functional coupling between TRPM7, a putative magnesium transporter, and a small G protein.

Introduction

Transient receptor potential melastatin-subfamily member 7 (TRPM7) encodes a bi-functional protein with a transient receptor potential (TRP) ion channel domain fused to a C-terminal α-type serine/threonine-protein kinase (reviewed in ***Chubanov et al., 2018***; ***Fleig and Chubanov, 2014***; ***Ryazanov et al., 1997***). Among all other known channels and kinases, only its homologue TPRM6 shows a similar design (***Ryazanov et al., 1997***; ***Chubanov and Gudermann, 2014***).

TRPM7 is involved in various cellular processes such as homeostatic balance, cell motility, proliferation, differentiation, and regulation of immune responses (***Chubanov et al., 2018***; ***Fleig and***

Chubanov, 2014; *Ryazanov et al., 1997*). Genetic deletion of *Trpm7* in mice is embryonically lethal, and tissue-specific null mutants have shown defects in cardiac and renal morphogenesis, organismal Zn^{2+}, Mg^{2+}, and Ca^{2+} homeostasis, thrombopoiesis, and mast cell degranulation (*Mittermeier et al., 2019*; *Chubanov et al., 2004*; *Jin et al., 2008*; *Sah et al., 2013b*; *Sah et al., 2013a*; *Jin et al., 2012*; *Stritt et al., 2016*; *Abiria et al., 2017*; *Schmitz et al., 2003*). Besides, TRPM7 has emerged as a promising therapeutic target for numerous pathophysiological conditions (*Chubanov et al., 2018*; *Fleig and Chubanov, 2014*; *Ryazanov et al., 1997*; *Hofmann et al., 2014*; *Aarts et al., 2003*; *Hermosura et al., 2005*).

The channel-coding segment of TRPM7 comprises six transmembrane helices with a pore-loop sequence between S5 and S6 (*Figure 1A*, *Duan et al., 2018*; *Mederos y Schnitzler et al., 2008*). Four subunits assemble to form constitutively active channels highly selective for divalent cations such as Zn^{2+}, Ca^{2+}, and Mg^{2+} (*Nadler et al., 2001*; *Runnels et al., 2001*; *Monteilh-Zoller et al., 2003*). Free Mg^{2+}, the Mg·ATP complex, and phosphatidylinositol-4,5-bisphosphate (PIP_2) were described as physiological regulators of the channel activity of TRPM7 (*Nadler et al., 2001*; *Runnels et al., 2002*). While Mg^{2+} or Mg·ATP act as negative regulators, PIP_2 appears to be a crucial co-factor of the active channel (*Nadler et al., 2001*; *Runnels et al., 2002*). Mechanistically, however, the effects of Mg^{2+}, Mg·ATP, or PIP_2 on TRPM7 activity are poorly understood, and most likely, there are additional regulators of TRPM7 function with hitherto unknown molecular identity.

The C-terminal α-kinase domain of TRPM7 acts in two ways: First, it autophosphorylates cytoplasmic residues of TRPM7, and second, it may target a variety of proteins with diverse cellular functions such as annexin A1, myosin II, eEF2-k, PLCγ2, STIM2, SMAD2, and RhoA (*Runnels et al., 2001*; *Dorovkov and Ryazanov, 2004*; *Perraud et al., 2011*; *Clark et al., 2008*; *Romagnani et al., 2017*; *Voringer et al., 2020*; *Faouzi et al., 2017*). In immune cells, the TRPM7 kinase domain has been reported to be clipped from the channel domain by caspases in response to Fas-receptor stimulation (*Desai et al., 2012*). In line with this observation, cleaved TRPM7 kinase was detected in several cell lines and shown to translocate to the nucleus, where it promotes histone phosphorylation (*Krapivinsky et al., 2014*).

The majority of the current knowledge about TRPM7 was derived from in vitro experiments with cultured cells, whereas insights into the operation of both channel and α-kinase activity of TRPM7 in native tissues are limited. We, therefore, investigated the molecular architecture of TRPM7 in rodent brain by using blue native polyacrylamide gel electrophoresis (BN-PAGE) and multi-epitope affinity purifications (ME-APs) in combination with high-resolution quantitative mass spectrometry (MS). These approaches showed that native TRPM7 channels are macromolecular complexes with an apparent size of ≧1.2 MDa and identified proteins CNNM1-4 and ADP-ribosylation factor-like protein 15 (ARL15) as complex constituents. Subsequent functional studies in *Xenopus laevis* oocytes and HEK293 cells suggested ARL15 and CNNM3 as hitherto unrecognised regulators of the TRPM7 ion channel and kinase activity, respectively.

Results

ME-AP proteomic analyses of native TRPM7 channels

TRPM7 channels assemble from four subunits (*Fleig and Chubanov, 2014*), each of which is about 1860 aa in length and comprises several distinct domains in its extended intracellular N- and C-termini in addition to a transmembrane channel domain (*Figure 1A*). Unexpectedly, analysis by native gel electrophoresis (BN-PAGE) of TRPM7 channels either endogenous to HEK293 cells or exogenously expressed in these cells via transient transfection, elicited a molecular mass of at least 1.2 MDa considerably exceeding the molecular mass of ~850 kDa calculated for TRPM7 tetramers (*Figure 1B*, upper panel). To see whether this large molecular size is a peculiarity of HEK293 cells, we recapitulated the analysis for TRPM7 channels expressed in mouse brain using a recently developed technique that combines BN-PAGE with cryo-slicing and quantitative mass spectrometry (csBN-MS, *Müller et al., 2019*). In this approach, membrane fractions prepared from the entire mouse brain and solubilised with the mild detergent buffer CL-47 (*Schwenk et al., 2016*; *Schwenk et al., 2012*; *Müller et al., 2010*) are first separated on a native gel, which is subsequently embedded and cut into 300 µm gel slices using a cryo-microtome. In a second step, the protein content of each slice is analysed individually by nanoflow liquid chromatography tandem mass spectrometry (nanoLC-MS/MS), providing

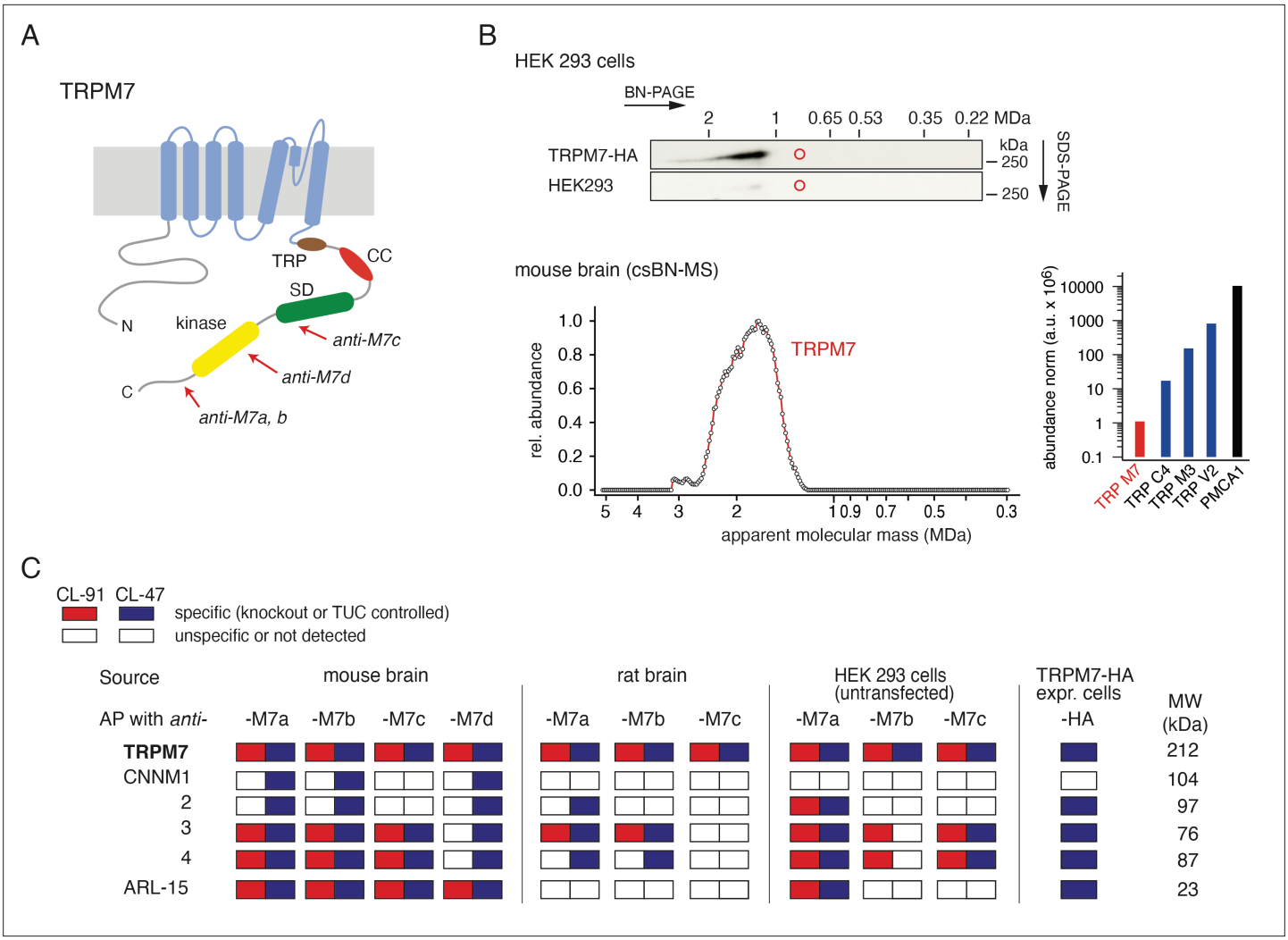

Figure 1. Protein constituents of native transient receptor potential melastatin-subfamily member 7 (TRPM7) channels identified by multi-epitope antibody-based affinity purification (ME-AP) proteomics. (**A**) Topology and localisation of the *anti*-TRPM7 antibodies used for ME-APs. Established hallmark domains of TRPM7 are colour-coded, TRP (transient receptor potential domain, brown), CC (coiled-coil domain, red), kinase (kinase domain, yellow), SD (serine/threonine-rich substrate domain of kinase(s), green). (**B**) *Upper panel*: Two-dimensional gel separation of TRPM7 channels in CL-47 solubilised membrane fractions of HEK293 cells with (*upper panel*) or without (*lower panel*) transfection of HA-tagged *Trpm7*, Western-probed with an *anti*-TRPM7 antibody (Materials and methods). Size (blue native polyacrylamide gel electrophoresis [BN-PAGE]) and molecular weight (SDS-PAGE) are as indicated. *Lower panel*: Abundance-mass profile of TRPM7 obtained by cryo-slicing blue native mass spectrometry (csBN-MS) in a CL-47 solubilised membrane fraction from adult mouse brain (a total of 192 gel slices). Inset: Abundance of the indicated proteins in the mouse brain. Note the large apparent molecular mass of the native TRPM7 channel in both culture cells and mouse brain, markedly exceeding the mass calculated for tetrameric channel assemblies (about 850 kDa, red circles). (**C**) Table summarising the results of all *anti*-TRPM7 APs performed with the indicated antibodies on membrane fractions prepared from rodent brain and cultured HEK293 cells. Solubilisation conditions and specificity of purification of the listed proteins determined by comparison with stringent negative controls are colour-coded as given in the upper left; MW is indicated on the right. TUC refers to series of APs with target-unrelated control antibodies. Note that TRPM7 channels co-assemble with all CNNM family members and ADP-ribosylation factor-like protein 15 (ARL15) in the brain and HEK293 cells.

The online version of this article includes the following figure supplement(s) for figure 1:

Figure supplement 1. The specificity of an *anti*-transient receptor potential melastatin-subfamily member 7 (TRPM7) mouse monoclonal antibody in Western blot assessment of the recombinant TRPM6 and TRPM7 proteins.

information on both the identity and amount of the proteins in each slice; noteworthy, protein amounts are determined with a dynamic range of up to four orders of magnitude (***Müller et al., 2010***; ***Schwenk et al., 2010***; ***Bildl et al., 2012***). As illustrated in ***Figure 1B***, lower panel, csBN-MS analysis of mouse brain membranes detected the TRPM7 protein with an apparent molecular mass between 1.2 and 2.6 MDa, comparable to the results obtained from HEK293 cells (***Figure 1B***, upper panel). Moreover, the

determination of the total protein amount by signal integration over all slices showed that TRPM7 levels in the brain are rather low compared to other members of the TRP family of proteins. Thus, the abundance of TRPM7 is about one to three orders of magnitude below that obtained for TRPC4, TRPM3, or TRPV2 (***Figure 1B***, lower right).

Together, these results indicated that native TRPM7 complexes exceed the predicted molecular size of bare tetrameric assemblies in different cellular environments suggesting that the rather simplistic view on the molecular make-up of native TRPM7 channel complexes has to be revised.

To identify proteins that may co-assemble with TRPM7, we used affinity purifications with multiple antibodies targeting distinct epitopes of the TRPM7 protein (***Figure 1A***, ***Figure 1—figure supplement 1***) and evaluated the respective eluates of HEK293 cells and rodent brains by high-resolution quantitative MS analysis (ME-APs, ***Schwenk et al., 2016***; ***Schwenk et al., 2012***; ***Müller et al., 2010***; ***Schwenk et al., 2010***). HEK293 cells were selected because these cells are widely used for the functional assessment of endogenous and overexpressed TRPM7. The brain was chosen since TRPM7 plays a critical role in neurological injuries and synaptic and cognitive functions (***Aarts et al., 2003***; ***Sun et al., 2009***; ***Liu et al., 2018***). For these ME-APs, membrane fractions prepared either from whole brains of adult mice and rats or from WT HEK293 cells were solubilised with detergent buffers of mild (CL-47) or intermediate (CL-91) stringency (***Schwenk et al., 2012***; ***Müller et al., 2010***; ***Schwenk et al., 2010***) prior to TRPM7 purification. TRPM7 was also affinity-isolated from HEK293 cells transiently (over)-expressing C-terminally HA-tagged TRPM7 using an *anti*-HA antibody.

In all APs, TRPM7 could be reliably detected under both solubilisation conditions (***Figure 1C***) with MS-identified peptides covering a large percentage of the primary sequence of TRPM7 in samples from mouse brain as well as from HEK293 cells (77% and 98%, respectively).

All other proteins identified in the ME-APs were evaluated for specificity and consistency of their co-purification with TRPM7 based on protein amounts determined by label-free quantification (see Materials and methods section). The specificity of co-purification was assessed by comparing protein amounts in APs targeting TRPM7 with protein amounts obtained with stringent negative controls. Thus, (i) APs with five different target-unrelated control (TUC) antibodies were used as negative controls for *anti*-TRPM7 APs from rodent brain, (ii) *anti*-TRPM7 APs from a *TRPM7*$^{-/-}$ HEK293 cell line (***Abiria et al., 2017***) served as negative controls for *anti*-TRPM7 APs from WT HEK293 cells, and (iii) HEK293 cells heterologously expressing TRPM7-myc were used as negative

Table 1. Protein constituents of native transient receptor potential melastatin-subfamily member 7 (TRPM7) channels identified by multi-epitope affinity purifications (ME-APs).

Protein ID	Acc. No. UniProtKB	Name	Primary function	Rel. abundance CL-47	Rel. abundance CL-91
TRPM7	Q923J1	TRP channel M7	Ion channel	=	=
CNNM1	Q0GA42	Transporter CNNM1, Cyclin-M1	Potential transporter	<<	
CNNM2	Q5U2P1	Transporter CNNM1, Cyclin-M2	Potential transporter	<	<<
CNNM3	Q32NY4	Transporter CNNM1, Cyclin-M3	Potential transporter	<	<<
CNNM4	Q69ZF7	Transporter CNNM1, Cyclin-M4	Potential transporter	<	<<
ARL15	Q8BGR6	ADP-ribosylation factor-like protein 15	Unknown	=	<<
TP4A1[†]	Q93096	Protein tyrosine phosphatase type IVA 1	Enzyme	<<<	<<
TP4A3[##]	Q9D658	Protein tyrosine phosphatase type IVA 3	Enzyme		<<
TRPM6[###]	Q9BX84	TRP channel M6	Ion channel	<<<	<<

Notes: Relative abundance refers to the amount of TRPM7 as a reference and was classified as follows: = when between 0.33-fold and 3.3-fold of reference, < when between 0.033-fold and 0.33-fold of reference, << when between 0.0033-fold and 0.033-fold of reference, and <<< when less than 0.0033-fold of the reference amount.

Transmembrane proteins; cytoplasmic proteins.

[†]Co-purified from HEK293 cells with *anti*-M7a (CL-47) and with *anti*-M7c (CL-91); [##]co-purified with anti-M7c from rat brain membranes (CL-91); [###]co-purified with anti-M7a from HEK293 cells (CL-47, CL-91).

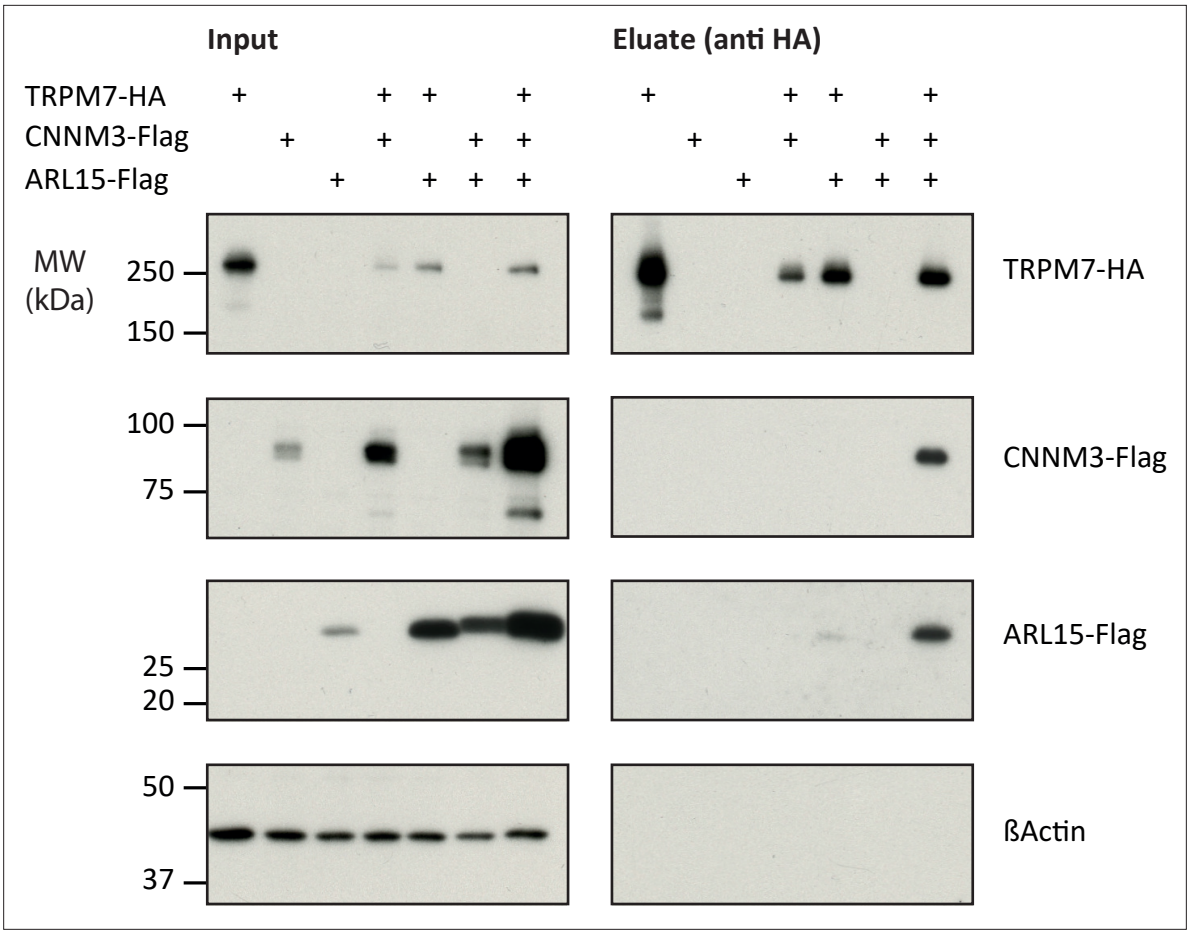

Figure 2. Heterologous reconstitution of transient receptor potential melastatin-subfamily member 7 (TRPM7) complexes in HEK293 cells. Affinity purifications (APs) with *anti*-HA antibody from CL-47 solubilised membrane fractions of *TRPM7*$^{-/-}$ HEK293 cells transiently expressing the proteins indicated above. Input and eluates of the distinct APs were separated by SDS-PAGE and Western-probed with *anti*-Flag, *anti*-HA, and *anti*-β-actin antibodies. Molecular weight (MW) is marked on the left.

The online version of this article includes the following figure supplement(s) for figure 2:

Figure supplement 1. Heterologous reconstitution of transient receptor potential melastatin-subfamily member 7 (TRPM7) complexes in HEK293 cells.

controls for *anti*-HA APs from HEK293 cells overexpressing TRPM7-HA. A protein was considered consistently co-purified if detected in APs with at least two antibodies under the same solubilisation condition. Together, these specificity and consistency criteria identified five proteins as high-confidence interaction partners of TRPM7: ARL15 and the cyclin M family proteins CNNM1-4, putative Mg^{2+} transporters (***Figure 1C***, ***Table 1***). Neither of these proteins was detected in any of the negative controls. Moreover, they were not only consistently co-purified with several antibodies but with the exception of CNNM1 also from both rodent brain and HEK293 cells. Comparison of the degree of association under the two solubilisation conditions revealed that the interaction between TRPM7, ARL15, and CNNMs was weakened by the more stringent detergent CL-91 (***Figure 1C***, ***Table 1***).

Next, we verified the identified interactions between TRPM7, ARL15, and CNNM1-4 in co-expression experiments performed in *TRPM7*$^{-/-}$ HEK293 cells (***Figure 2***). Flag-tagged ARL15 and CNNM proteins could be specifically and robustly co-purified with HA-tagged TRPM7 in *anti*-HA APs when all three proteins were present, whereas the association was markedly less efficient when ARL15-Flag or CNNM-Flag were co-expressed with TRPM7-HA alone (***Figure 2***, ***Figure 2—figure supplement 1***). These results corroborated the ME-AP results from the rodent brain and strongly suggested the formation of ternary complexes containing TRPM7, ARL15, and CNNM proteins.

Effects of CNNM3 and ARL15 on TRPM7 channel activity

To investigate if the assembly of TRPM7 with ARL15 and CNNM proteins modified TRPM7 function, we studied their effect(s) on TRPM7 currents by co-expression in *X. laevis* oocytes. This approach allows co-expression of defined protein ratios by cRNA injection and, therefore, is widely used for functional assessment of ion channel complexes, including functional interaction of TRPM7 with TRPM6 (***Chubanov et al., 2018***; ***Chubanov et al., 2004***). The two-electrode voltage clamp (TEVC) measurement in ***Figure 3A*** illustrates a typical current-voltage (I-V) relationship of constitutively active TRPM7 channels characterised by steep outward rectification and very small inward currents over the whole range of negative membrane potentials (***Nadler et al., 2001***). Co-expression of TRPM7 and CNNM3, the most efficiently co-purified CNNM protein (***Figure 1C***), neither changed the shape of the I-V relationship nor current amplitudes. In contrast, ARL15 effectively suppressed constitutive TRPM7 currents in a concentration-dependent manner, as deduced from experiments with increasing amounts of ARL15 (***Figure 3B and C***). Oocytes co-expressing all three proteins TRPM7, CNNM3, and ARL15 did not exhibit TRPM7 currents, similar to the co-expression of TRPM7 and ARL15 (***Figure 3A***). The suppressive effect was specific for TRPM7, as co-expressed ARL15 did not inhibit another TRP channel, TRPV1, in an analogous experiment (***Figure 3—figure supplement 1***). Consistently, co-expression of TRPM7 with another ARL family member, ARL8A (***Gillingham and Munro, 2007***), did not affect TRPM7 currents (***Figure 3—figure supplement 2***).

Next, we examined if the interference of ARL15 with the TRPM7 function was due to reduced expression levels or altered membrane localisation. Western blot analysis of oocytes injected with *Trpm7* or *Trpm7* and *Arl15* cRNAs did not reveal any change in the expression level of TRPM7 protein (***Figure 3D***). Using immunofluorescence staining with the *anti*-M7d antibody, we detected TRPM7 at the cell surface of oocytes injected with *Trpm7* but not in uninjected oocytes (***Figure 3E***). Notably, the TRPM7 signal was similarly detectable at the cell surface of oocytes co-expressing TRPM7 and ARL15 (***Figure 3E***).

TRPM7 inward currents at negative membrane potentials are small, and, consequently, quantification of the comparably large outward currents is commonly used for functional assessment of the TRPM7 channel activity. Nevertheless, we asked whether TRPM7 inward currents could be equally suppressed by ARL15 (***Figure 3—figure supplement 3A, B***). This analysis revealed that ARL15 acted similarly on inward and outward TRPM7 currents, suggesting that ARL15 elicited a general block of the TRPM7 channel.

To obtain further insight into the functional interaction of ARL15 with TRPM7, we investigated whether the kinase activity of TRPM7 is necessary for the inhibitory effect of ARL15. To this end, we examined oocytes expressing a kinase-dead TRPM7 mutant (K1646R, ***Nadler et al., 2001***; ***Runnels et al., 2002***) and observed that the K1646R mutation did not change the sensitivity of TRPM7 for the inhibitory effect of ARL15 (***Figure 3—figure supplement 3C***).

Finally, we investigated whether ARL15 could also regulate TRPM7 channels in mammalian cells. Using the patch-clamp technique, we measured endogenous TRPM7 currents in HEK293 cells. Similar to previous reports (***Chubanov et al., 2004***; ***Ferioli et al., 2017***), removing intracellular Mg^{2+} by using a pipette solution free of divalent cations induced endogenous TRPM7 currents (***Figure 3—figure supplement 4***). Transient expression of ARL15 however caused a significant reduction of these TRPM7 currents (***Figure 3—figure supplement 4***).

Collectively, these results suggest that the inhibitory effect of ARL15 on TRPM7 currents is specific and concentration-dependent.

Impact of CNNM3 on TRPM7 Mg^{2+} currents and kinase activity

Given the crucial role of TRPM7 and CNNM proteins in membrane Mg^{2+} transport (***Mittermeier et al., 2019***; ***Schmitz et al., 2003***; ***Funato and Miki, 2019***), we asked whether CNNM3 would specifically affect TRPM7 Mg^{2+} currents rather than exerting a general (i.e., ARL15-like) effect. To this end, we conducted TEVC measurements with TRPM7-expressing oocytes using external saline containing 3 mM Mg^{2+} (instead of 3 mM Ba^{2+} in ***Figure 3A***), implying that at negative membrane potentials, the TRPM7 channel should primarily exhibit Mg^{2+} currents under such experimental conditions (***Nadler et al., 2001***). TRPM7 expressing oocytes displayed characteristic TRPM7 currents with a very small inward Mg^{2+} component, which was suppressed by co-expression of ARL15 (***Figure 4A and B***) in accord with previous experiments (***Figure 3—figure supplement 3A, B***). In contrast, co-expression of CNNM3 did not change the properties of the TRPM7 channel (***Figure 4C and D***).

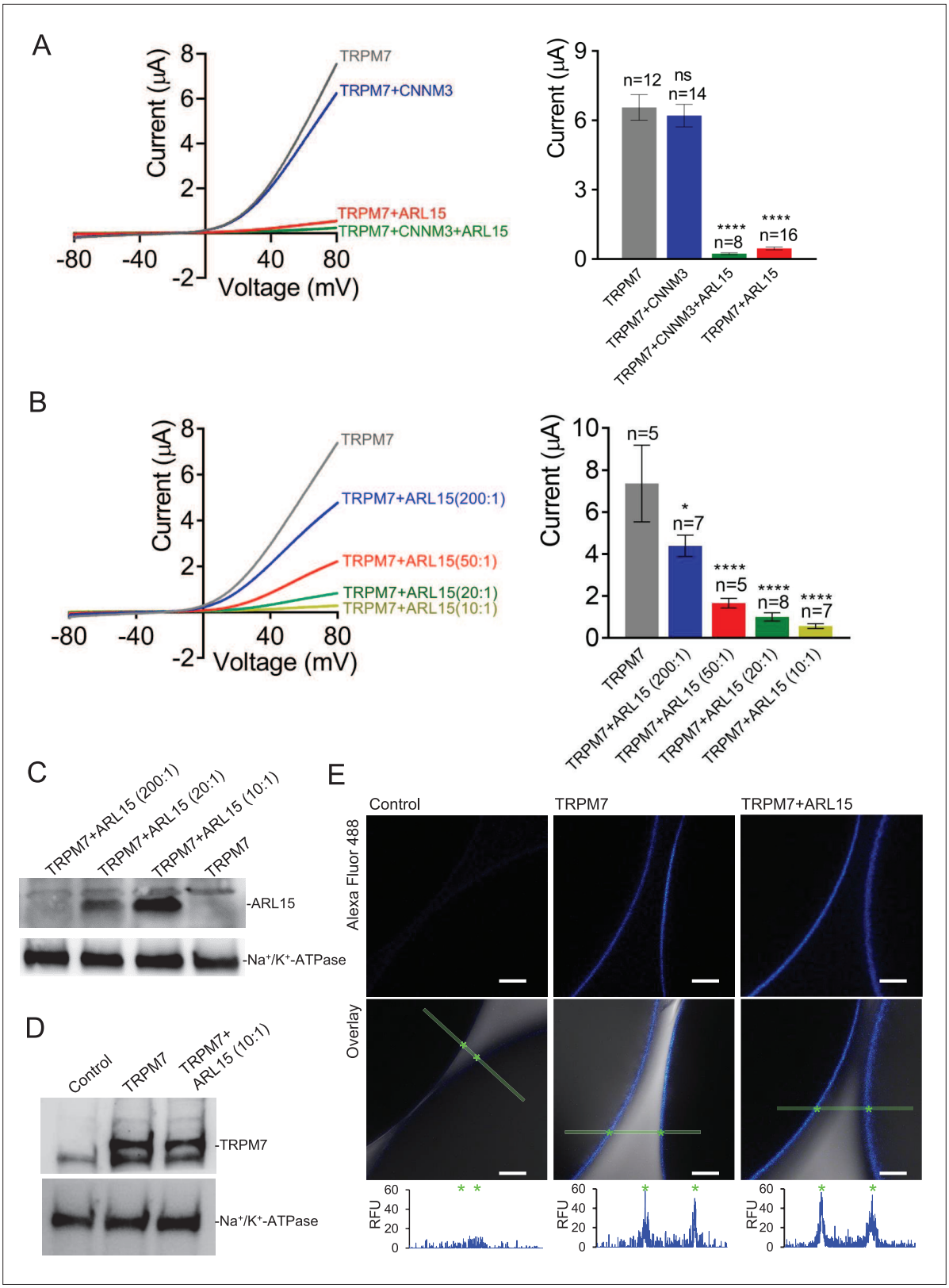

Figure 3. Heterologous expression of transient receptor potential melastatin-subfamily member 7 (TRPM7) in *Xenopus* oocytes. (**A, B**) Two-electrode voltage clamp (TEVC) measurements of TRPM7 currents. (**A**) *Left panel*: Representative current-voltage (I-V) relationships of TRPM7 currents measured in oocytes expressing TRPM7 alone or TRPM7 with CNNM3 or ADP-ribosylation factor-like protein 15 (ARL15) (cRNAs ratio 2:1), and TRPM7 with CNNM3 and ARL15 (cRNAs ratio 2:1:1). *Right panel*: Current amplitudes (mean ± standard error of the mean [SEM]) at +80 mV in measurements shown on the

Figure 3 continued on next page

Figure 3 continued

left. Two independent batches of injected oocytes (n = 8–16) were examined. *p < 0.05; ****p < 0.0001 (ANOVA). (**B**) *Left panel*: Representative I-V relationships of TRPM7 currents measured in oocytes expressing TRPM7 or co-expressing TRPM7 with ARL15 at the indicated ratios of injected cRNAs. *Right panel*: Current amplitudes (mean ± SEM) at +80 mV in measurements shown on the left. Two independent batches of injected oocytes (n = 5–7) were examined. *p < 0.05; ****p < 0.0001 (ANOVA). (**C**) Western blot analysis of ARL15 expression using the *anti*-Myc antibody in total lysates of oocytes injected with *Trpm7* or *Trpm7* and *Arl15* cRNAs (ratios 200:1, 20:1, and 10:1). Representative results are shown for two independent experiments. *Anti*-Na^+/K^+-ATPase antibody was used for loading controls. (**D**) Western blot analysis of TRPM7 expression using the *anti*-M7d antibody in total lysates of oocytes injected with *Trpm7* or *Trpm7* and *Arl15* cRNAs (ratio 10:1). *Anti*-Na^+/K^+ ATPase antibody was used for loading controls. Representative results are shown for two independent experiments. (**E**) Immunofluorescence staining of un-injected oocytes (control) or oocytes injected with *Trpm7* (TRPM7) or *Trpm7* and *Arl15* cRNAs (TRPM7+ ARL15, ratio 10:1) using *anti*-M7d antibody and *anti*-mouse antibody conjugated with Alexa Fluor 488. Confocal images of Alexa Fluor 488 fluorescence (Alexa488) and overlays of Alexa488 with differential interference contrast images (overlay) are depicted for two independent oocytes per image; scale bars, 50 µm. The diagrams depict fluorescence intensity acquired along the green bars shown in *overlay* images. The stars indicate the cell surface of two oocytes. Typical examples of two independent experiments (n = 10 oocytes) are shown.

The online version of this article includes the following figure supplement(s) for figure 3:

Figure supplement 1. Two-electrode voltage clamp (TEVC) measurements of capsaicin-induced TRPV1 currents in *Xenopus* oocytes.

Figure supplement 2. Heterologous expression of transient receptor potential melastatin-subfamily member 7 (TRPM7), ARL8A, and ADP-ribosylation factor-like protein 15 (ARL15) in *Xenopus* oocytes.

Figure supplement 3. Assessment of the importance of the transient receptor potential melastatin-subfamily member 7 (TRPM7) kinase activity for the functional interplay between ADP-ribosylation factor-like protein 15 (ARL15) and TRPM7 by two-electrode voltage clamp (TEVC) measurements.

Figure supplement 4. Impact of ADP-ribosylation factor-like protein 15 (ARL15) on endogenous transient receptor potential melastatin-subfamily member 7 (TRPM7) currents in HEK293 cells.

Next, we studied whether heterologous expression in mammalian cells would allow uncovering any functional effects of CNNM3 on TRPM7. We transiently transfected HEK293 cells with *Trpm7* and *Cnnm3* plasmid cDNAs (ratio 2:1) and performed patch-clamp measurements (***Figure 4—figure supplement 1***). TRPM7 currents were induced using the standard divalent cation-free internal solution and an external buffer containing 1 mM $CaCl_2$ and 2 mM $MgCl_2$. When currents were developed, cells were exposed to mannitol-based saline containing 10 mM Mg^{2+}. In accord with previous publications (***Ferioli et al., 2017***), the perfusion of TRPM7-expressing cells with 10 mM Mg^{2+} led to a significant reduction of outward currents accompanied by a relatively modest decrease of inward currents (***Figure 4—figure supplement 1***). Corresponding experiments with cells co-expressing TRPM7 and CNNM3 showed similar results (***Figure 4—figure supplement 1***), compatible with a TRPM7 Mg^{2+} permeability unaltered by co-expression of CNNM3, regardless of the heterologous expression system.

Previously, we found that TRPM7 controls the uptake of Mg^{2+} to maintain the cellular content of this mineral in resting cells (***Mittermeier et al., 2019***). To investigate whether CNNM3 modulates TRPM7-dependent Mg^{2+} uptake, we employed inductively coupled plasma mass spectrometry (ICP-MS) to compare total amounts of magnesium in *TRPM7*$^{-/-}$ HEK293 cells transfected with *Trpm7*, *Cnnm3*, or *Trpm7* plus *Cnnm3* cDNAs (***Figure 4—figure supplement 2***). Next, we normalised the levels of magnesium to cellular sulphur (a biomarker for the total protein content) and observed that transient expression of TRPM7 increased the cellular Mg content, whereas expression of CNNM3 did not change this parameter (***Figure 4—figure supplement 2***). Importantly, we found that co-expression of TRPM7 with CNNM3 did not impact the ability of TRPM7 to regulate the cellular content of Mg^{2+} (***Figure 4—figure supplement 2***). Hence, different experimental approaches did not reveal significant effects of CNNM3 on TRPM7 channel activity.

Since TRPM7 contains a C-terminal kinase domain, we studied whether CNNM3 might modulate the TRPM7 kinase moiety (***Figure 5*** and ***Figure 5—figure supplement 1***). To assess the activity of the TRPM7 kinase, we relied on the *anti*-(p)Ser1511 M7 antibody, which specifically recognises the known autophosphorylation site (Ser1511) of mouse TRPM7 (***Romagnani et al., 2017***). To verify that autophosphorylation of Ser1511 is dynamic, and changes of the TRPM7 kinase activity could therefore be visualised by the anti-(p)Ser1511 M7 antibody we treated HEK293 cells transiently overexpressing TRPM7 with TG100-115, a drug-like TRPM7 kinase inhibitor (***Song et al., 2017***). We observed that the exposure of living cells to TG100-115 led to suppression of (p)Ser1511 TRPM7 immunoreactivity in a dose-dependent fashion (***Figure 5—figure supplement 1A***). Moreover, the inhibitory effect of TG100-115 was time-dependent and could be detected 10 min after application of TG100-115

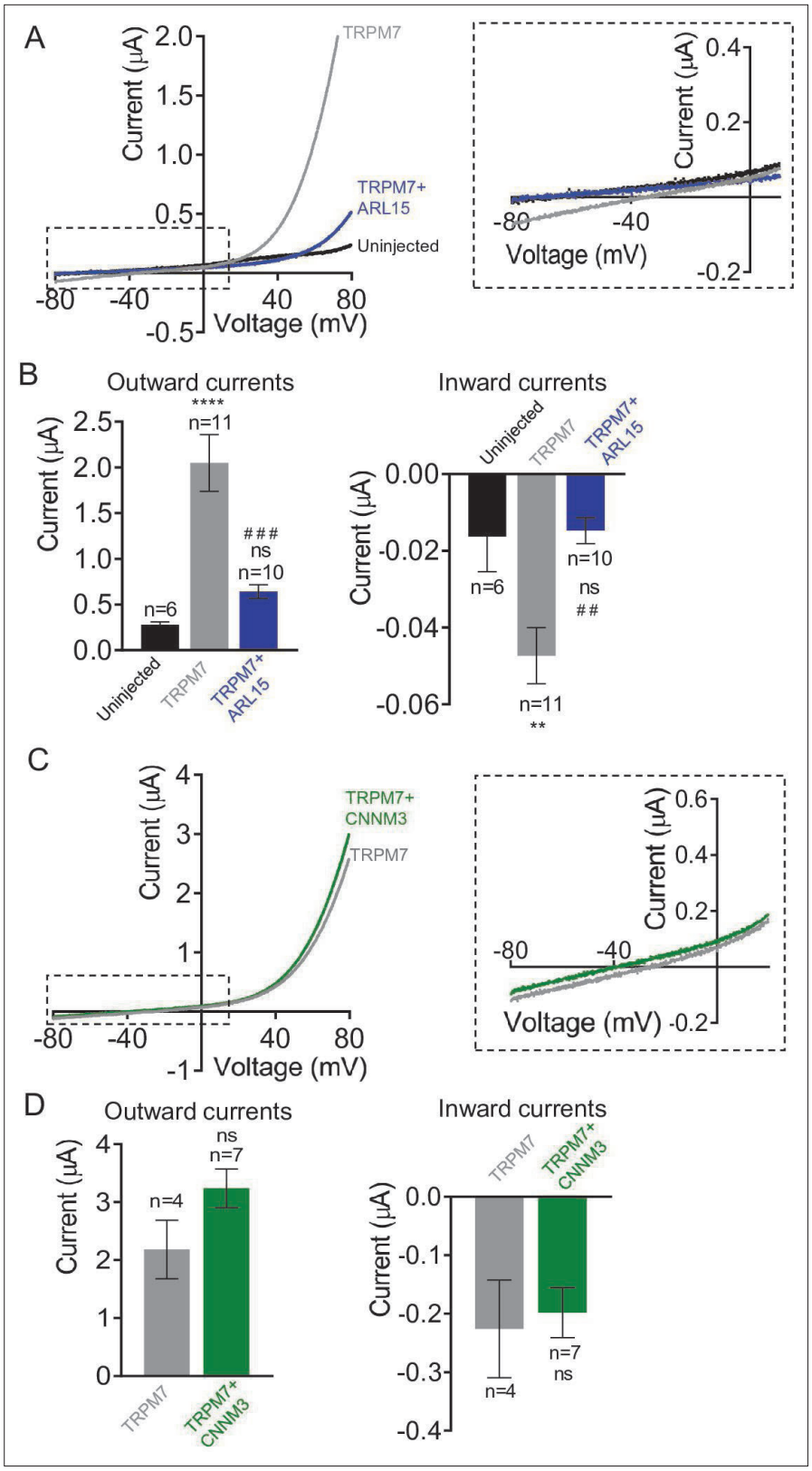

Figure 4. Effects of ADP-ribosylation factor-like protein 15 (ARL15) and CNNM3 on Mg^{2+} currents of the transient receptor potential melastatin-subfamily member 7 (TRPM7) channel expressed in *Xenopus* oocytes.
TEVC measurements were performed using the external ND96 solution containing 3 mM Mg2+and no other divalent cations. (A, B) Assessment of oocytes expressing TRPM7 or co-expressing TRPM7 with ARL15 (cRNA ratio

Figure 4 continued on next page

Figure 4 continued

10:1). (A) Representative I-V relationships ofTRPM7 currents. The dashed box in Left panelindicates the area of inward currents enlarged in the Right panel. (B) Current amplitudes (mean ± SEM) at+80 mV (Outward currents) and at -80 mV (Inward currents) in measurements from (A). Two independent batches of injected oocytes (n=6-11) were examined. ns, not 36significant; ** P < 0.01, **** P < 0.0001 significant to the Uninjected group (ANOVA). # # P < 0.01, # # # P < 0.001 significant to the TRPM7 group (ANOVA). (C, D) Examination of oocytes expressing TRPM7 or co-expressing TRPM7 with CNNM3 (cRNA ratio 2:1). Data were produced and analyzed as explained in (A, B). Two independent batches of injected oocytes (n=4-7) were examined. ns, not significant (two-tailed t-test).

The online version of this article includes the following figure supplement(s) for figure 4:

Figure supplement 1. Heterologous expression of transient receptor potential melastatin-subfamily member 7 (TRPM7) and CNNM3 in HEK293T cells.

Figure supplement 2. Assessment of total magnesium levels in *TRPM7*$^{-/-}$ HEK293T cells transiently transfected with *Trpm7* and *Cnnm3* plasmid cDNAs.

(***Figure 5—figure supplement 1B***). Furthermore, we found that wash-out of TG100-115 by fresh cell culture medium caused a fast recovery of the (p)Ser1511 TRPM7 signal (***Figure 5—figure supplement 1C***). Hence, detection of (p)Ser1511 TRPM7 levels seems a reliable means to monitor the TRPM7 kinase activity. Accordingly, we investigated whether co-expression of ARL15 could modulate TRPM7 kinase activity and found no changes in (p)Ser1511 TRPM7 immunoreactivity (***Figure 5***). Co-expression of CNNM3 however caused a significant reduction of the (p)Ser1511 TRPM7 signal (***Figure 5***), suggesting that CNNM3 functions as a negative regulator of the TRPM7 kinase.

Identification of new phosphorylation sites in the TRPM7 protein

In addition to subunit assembly, the MS data provided further insight into the post-translational modification(s) of the TRPM7 protein. Thus, TRPM7 purified either from rodent brain or from transfected HEK293 cells showed very similar patterns of serine and threonine phosphorylation, reflected by matching MS/MS spectra of peptides harbouring phosphorylation sites (***Figure 6A***, ***Figure 6—figure supplement 1***, ***Supplementary file 2*** to ***Figure 6***). Out of the nine shared phospho-sites, four have not been reported for TRPM7 in native tissue before (S1300, S1360, T1466, and S1567; ***Supplementary file 2*** to ***Figure 6***). An additional 26 phosphorylated serine and threonine residues could be assigned to TRPM7 isolated from HEK 293 cells, presumably based on the higher amounts of TRPM7 available for analysis from heterologous (over)-expression material; 22 of these 26 sites match sites previously reported for TRPM7 endogenously or heterologously expressed in cell lines, and four sites were newly detected (S1208, S1480, S1496, S1853; ***Supplementary file 2*** to ***Figure 6***). Most of the identified phosphorylation sites were found to cluster within the C-terminal cytoplasmic domain of TRPM7.

Finally, we asked whether measuring TRPM7 channel activity by TEVC would reveal any functional consequences of TRPM7 phosphorylation. We introduced phosphomimetic mutations in a subset of identified phospho-sites (S1208D, S1360D, S1480D, S1496D, and S1567D) and found that three TRPM7 mutants (S1208D, S1496D, and S1567D) displayed enhanced current amplitudes (***Figure 6B and C***), whereas their expression levels were similar to WT TRPM7 (***Figure 6D***). These findings suggest that phosphorylation of TRPM7 may represent a new regulatory mechanism reminiscent of the situation with TRPM8 (***Rivera et al., 2021***). To substantiate this notion further, it will be interesting to carry out a systematic functional analysis of the surprisingly extensive phosphorylation profile of TRPM7 (***Figure 6***).

Discussion

In the present study, we investigated the molecular appearance and subunit composition of TRPM7 as present in the cell membrane(s) of the rodent brain. We show that TRPM7 forms macromolecular complexes by assembling with CNNM proteins 1-4 and ARL15. Moreover, functional expression in heterologous expression systems showed that ARL15 strongly affects TRPM7 channel function, while CNNM3 appears to act as a negative regulator of TRPM7 kinase activity.

BN-PAGE of membrane fractions isolated from rodent brain and cultured HEK 293 cells identified endogenous TRPM7 in high ~1.2 MDa molecular weight complexes exceeding the calculated

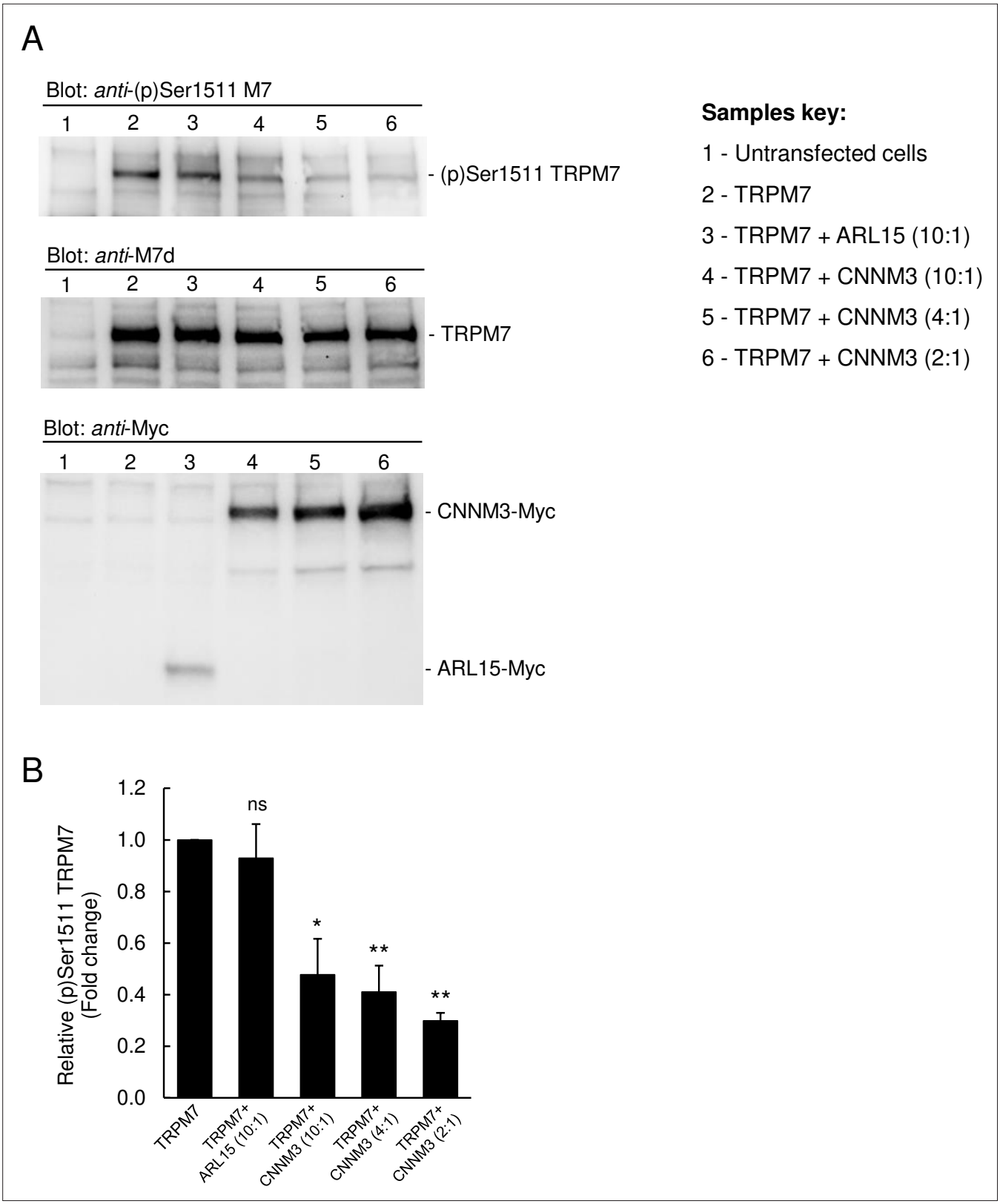

Figure 5. Impact of ADP-ribosylation factor-like protein 15 (ARL15) and CNNM3 on transient receptor potential melastatin-subfamily member 7 (TRPM7) autophosphorylation at Ser1511. (**A**) HEK293 cells were transiently transfected with *Trpm7*, co-transfected with *Trpm7* and *Arl15*, or with *Trpm7* and different amounts of *Cnnm3* plasmid cDNAs. Twenty-four hours after transfection, cell lysates were examined using an *anti*-(p)Ser1511 M7 antibody (*upper panel*). After a stripping step, the blot was probed with *anti*-M7d (*middle panel*) and anti-*Myc* antibodies (*lower panel*) to detect total levels of

Figure 5 continued on next page

Figure 5 continued

TRPM7, ARL15-Myc, and CNNM3-Myc, respectively. Representative results are shown from three independent experiments. (**B**) Quantification of (p) Ser1511 TRPM7 levels in Western blot experiments (n = 3) shown in (**A**). A relative band density for each sample was obtained by dividing the (p)Ser1511 signal (*upper panel*) by the corresponding *anti*-M7d value (*middle panel*). The relative density of *Sample 2* (TRPM7) was set as a 1.0 to calculate changes in (p)Ser1511 TRPM7 (mean ± standard error of the mean [SEM]) caused by co-transfection of *Arl15* or *Cnnm3* as outlined in the bar graph. ns, not significant; *p ≤ 0.05, **p ≤ 0.01 significant to the control (ANOVA).

The online version of this article includes the following figure supplement(s) for figure 5:

Figure supplement 1. Effects of TG100-115 on transient receptor potential melastatin-subfamily member 7 (TRPM7) autophosphorylation.

molecular mass of TRPM7 tetramers (~850 kDa) and suggesting that the TRPM7 channel kinase is predominantly embedded in a large macromolecular complex. Compared to other native TRP channels, such as TRPC4, TRPM3, and TRPV2, the expression level of TRPM7 was found to be up to three orders of magnitude lower, thus classifying TRPM7 as a very low-abundant protein in the rodent brain and indicating that comprehensive determination of the TRPM7 complexome is technically challenging. The unbiased ME-AP approach paired with stringent negative controls nevertheless allowed for the identification of high-confidence interaction partners based on their specific and consistent co-purification with TRPM7. Consequently, five proteins were found to assemble with native TRPM7, including four members of the *CNNM* gene family encoding putative Mg^{2+} transporters CNNM1-4 and a small G-protein ARL15. The fact that we did not detect all the interactors seen in mouse brain also in APs from rat brain is most likely due to the low abundance of endogenous TRPM7 (~50% less TRPM7 compared to APs from mouse brain). The interaction of TRPM7 with ARL15 and CNNM proteins was successfully confirmed in heterologous expression experiments. We also noted that previous proteome-wide interactome screens in cultured cells suggested an association of ARL15 with TRPM7 (***Huttlin et al., 2017***; ***Huttlin et al., 2021***), in line with our results.

To obtain first insight into a possible functional impact of ARL15 and CNNM3, the most prominent interaction partners of TRPM7 in our experimental settings, we measured the channel activity of TRPM7 expressed in *Xenopus* oocytes and HEK293 cells. We found that co-expression of TRPM7 with CNNM3 did not lead to significant changes in TRPM7 currents applying a broad range of experimental conditions. Consistently, we observed that the ability of TRPM7 to increase cellular Mg levels was not affected by CNNM3. However, CNNM3 appears to act as a negative regulator of the TRPM7 kinase activity, resembling the action of the drug-like kinase inhibitor TG100-115. Collectively, these results suggest that CNNM3 may represent the first known protein acting as a physiological modulator of the TRPM7 kinase activity.

In contrast to CNNM3, co-expression of TRPM7 with ARL15 in oocytes, but not with the closely related small G-protein ARL8A, caused robust suppression of TRPM7 currents regardless of the experimental conditions applied. Of note, transient expression of ARL15 in HEK 293 cells resulted in inhibition of endogenous TRPM7 currents, reinforcing our conclusion that ARL15 acts as a potent and specific negative regulator of the TRPM7 channel.

The *CNNM* (Cyclin M; CorC) gene family encodes highly conserved metal transporter proteins identified in all branches of living organisms, ranging from prokaryotes to humans (***Funato and Miki, 2019***; ***Giménez-Mascarell et al., 2019***). There are four family members in mammals, CNNM1-4, widely expressed in the body and abundantly present in the brain (***Funato and Miki, 2019***; ***Giménez-Mascarell et al., 2019***). The genetic inactivation of *Cnnm4* in mice leads to systemic Mg^{2+} deficiency (***Yamazaki et al., 2013***). In humans, point mutations in *CNNM2* cause hypomagnesemia (***Stuiver et al., 2011***), while mutations in *CNNM4* are associated with Jalili syndrome (***Parry et al., 2009***). Functional expression studies proposed that CNNMs operate as Na^{+}/Mg^{2+} exchangers responsible for the efflux of cytosolic Mg^{2+} from the cell (***Funato and Miki, 2019***; ***Giménez-Mascarell et al., 2019***). In contrast to this view, other investigators proposed that CNNM proteins indirectly regulate the influx of Mg^{2+} into the cell (***Arjona and de Baaij, 2018***). Recently resolved crystal structures of two prokaryotic CNNM-like proteins revealed that CNNMs form dimers and that each monomer contains three transmembrane helices harbouring Mg^{2+} and Na^{+} binding sites consistent with the suggested Na^{+}-coupled Mg^{2+} transport function of CNNMs (***Huang et al., 2021***; ***Chen et al., 2021***). While the majority of CNNM proteins in a cell is not bound to TRPM7, the direct association identified in this study suggests a new concept implying that two transporting mechanisms, TRPM7-mediated influx of divalent cations (Zn^{2+}, Mg^{2+}, and Ca^{2+}) and CNNM-dependent Na^{+}/Mg^{2+} exchange, can be physically coupled under

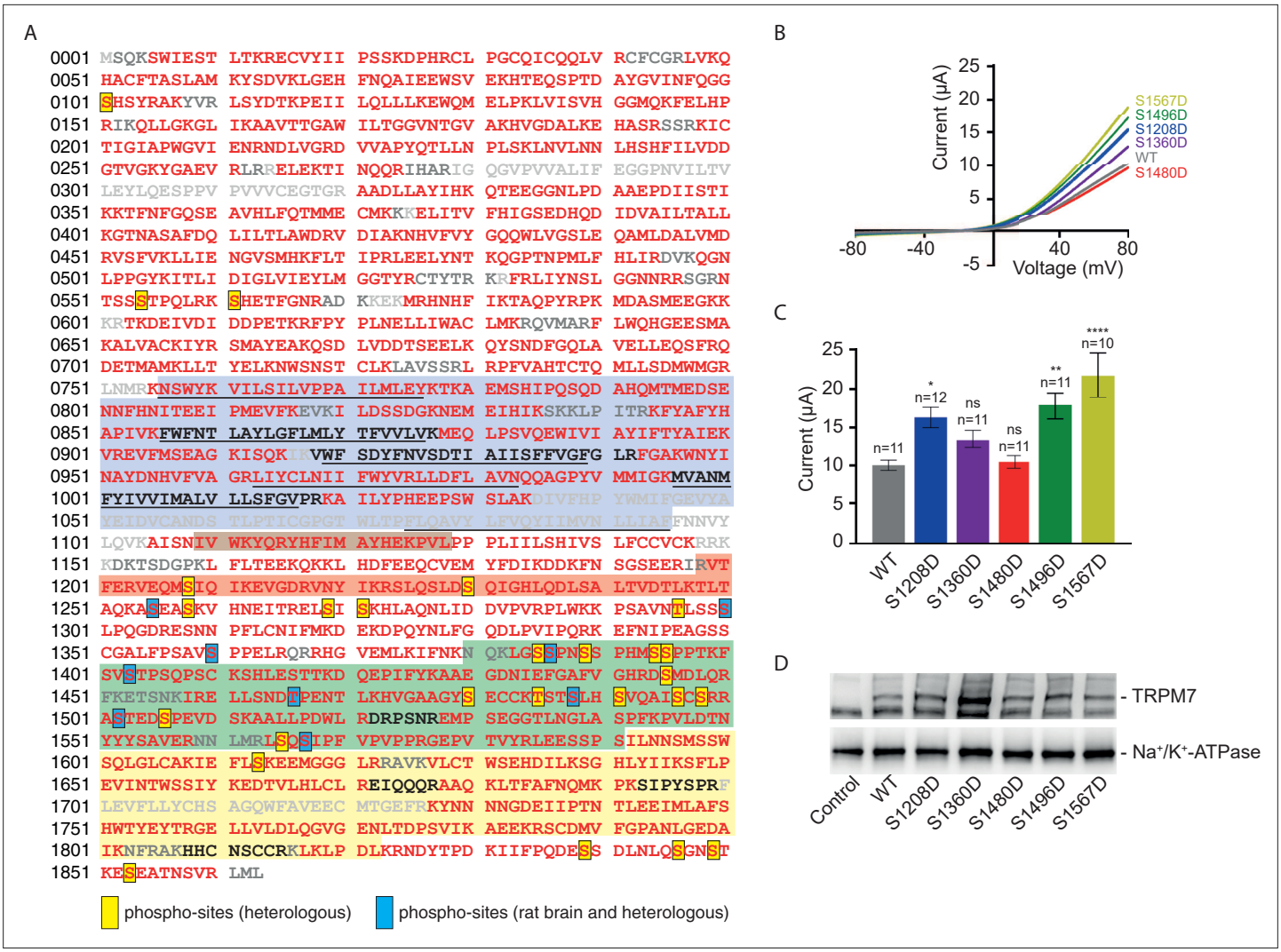

Figure 6. Identification of transient receptor potential melastatin-subfamily member 7 (TRPM7) phospho-sites and functional assessment of phosphomimetic TRPM7 mutants. (**A**) Coverage of the primary sequence of TRPM7 and phosphorylation sites as identified by mass spectrometry (MS) analyses of affinity purifications (APs) from transfected HEK293 cells and rodent brain. Peptides identified by MS are in red; those accessible to but not identified in tandem mass spectrometry (MS/MS) analyses are in black, and peptides not accessible to the MS/MS analyses used are given in grey. Blue boxes indicate phospho-sites identified in the brain and transfected HEK293 cells; those uniquely seen in heterologous expressions are boxed in yellow. Colour coding of hallmark domains is as in ***Figure 1A***; S1-S6 helices of TRPM7 are underlined. (**B, C**) Two-electrode voltage clamp (TEVC) measurements of phosphomimetic TRPM7 mutants performed and analysed as explained in ***Figure 3A***. (**B**) Representative current-voltage (I-V) relationships of TRPM7 currents measured in oocytes expressing WT and mutant variants of TRPM7, as indicated. (**C**) Current amplitudes (mean ± standard error of the mean [SEM]) at +80 mV of measurements shown in (**B**). Two independent batches of injected oocytes (n = 10–12) were examined. ns, not significant; *p ≤ 0.05, **p ≤ 0.01, ****p ≤ 0.0001 (ANOVA). (**D**) Western blot analysis of TRPM7 variants with phosphomimetic mutations expressed in *Xenopus* oocytes. Lysates of un-injected oocytes (control) or oocytes injected with WT and indicated mutant variants of *Trpm7* cRNAs were examined using the *anti*-M7d antibody. The *anti*-Na^{+}/K^{+} ATPase antibody was used for loading controls. Representative results are shown for three independent experiments.

The online version of this article includes the following figure supplement(s) for figure 6:

Figure supplement 1. Tandem mass spectrometry (MS/MS) spectra illustrating phosphorylation of Ser1567 in transient receptor potential melastatin-subfamily member 7 (TRPM7) from both brain (upper panel) and culture cells (lower panel).

native conditions, thus, warranting future studies to examine the exact functional interplay between the channel-kinase TRPM7 and CNNMs.

ARL15 is a member of the *ARF* gene family of small G-proteins (***Gillingham and Munro, 2007***). A common feature of ARFs is their ability to bind and regulate effector proteins in a GTP-dependent manner (***Gillingham and Munro, 2007***). GDP- and GTP-bound states of ARFs are controlled by GTPase-activating proteins (GAP) in conjunction with GTP exchange factors (GEF) (***Gillingham and***

Munro, 2007). The best-characterised ARFs are involved in membrane trafficking, phospholipid metabolism and remodelling of the cytoskeleton (*Gillingham and Munro, 2007*). While genome-wide association studies have linked ARL15 to systemic Mg^{2+} homeostasis and energy metabolism in humans (*Corre et al., 2018*; *Richards et al., 2009*), the particular functional role and corresponding GAP, GEF, and effector proteins of ARL15 remain to be established. To this end, the strong effect of ARL15 in suppressing TRPM7 currents observed in our study may suggest that TRPM7 serves as a specific effector protein of ARL15. The significance of this modulatory effect for native TRPM7 in the rodent brain, however, remains to be shown.

In some TRPM7-APs from HEK293 cells, we detected TRPM6, a genetically related channel, and two proteins representing the gene family of phosphatase of regenerating liver 1 and 3 (also entitled protein tyrosine phosphatases type 4A1 and 3, TP4A1 and 3) (*Table 1*). The Mg^{2+} transporter protein TRPM6 has been described to physically and functionally interact with TRPM7 (*Chubanov et al., 2004*; *Ferioli et al., 2017*; *Chubanov et al., 2016*). In the present study, TRPM6, even though detected, could not be consistently co-purified with multiple anti-TRPM7 antibodies, likely because TRPM6 is expressed at very low levels in the brain and HEK293 cells. Nevertheless, a previous study reporting that heterologously expressed ARL15 positively modulates TRPM6 (*Corre et al., 2018*) might suggest an overlap between the TRPM6 and TRPM7 interactomes.

Interestingly, a recent interactome screen based on lentiviral overexpression of tagged proteins in HEK293 and HTC116 cells revealed that TP4A1 and TP4A2 also interact with ARL15 and CNNMs (*Huttlin et al., 2017*; *Huttlin et al., 2021*). Furthermore, a hypothesis-driven search for interaction partners of CNNMs has shown that TP4A proteins assemble with CNNMs and that such interactions shape Mg^{2+} efflux from cells (*Funato et al., 2014*; *Hardy et al., 2015*; *Gulerez et al., 2016*; *Kostantin et al., 2016*; *Zhang et al., 2017*; *Giménez-Mascarell et al., 2017*). These findings are commensurate with our observation that TP4A1 and TP4A3 could be found in TRPM7 APs at low amounts.

Hence, based on the present analysis of native TRPM7 complexes in conjunction with earlier interactome experiments and functional expression studies, it is tempting to speculate that TRPM7/ARL15/CNNMs/TP4As form a protein network orchestrating transport of divalent cations across the cell membrane.

Materials and methods

Key resources table

Reagent type (species) or resource	Designation	Source or reference	Identifiers	Additional information
Strain, strain background (*Mus musculus*)	C57BL/6	Jackson Labs	JAX stock #000664	Six weeks of age, equal numbers of male and female
Strain, strain background (*Ratus norvegicus*)	Wistar	Charles River	Strain code:003	Six weeks of age, equal numbers of male and female
Strain, strain background (*Xenopus laevis*)	*Xenopus laevis*	NASCO	Cat#:LM00535	
Cell line (human)	HEK293T	Sigma	Cat#:96121229; RRID:CVCL_2737	
Cell line (human)	*TRPM7*$^{-/-}$ HEK293T	DOI:10.1073/pnas.1707380114		
Cell line (human)	HEK293T-Rex cells stably expressing *TRPM7*	10.1016 /s0092-8674(03)00556–7		
Antibody	Anti-HA (rat monoclonal)	Roche	Cat#:11867423001; RRID:AB_390918	IP (3–15 µg per IP), WB (0.2 µg/ml)
Antibody	Anti-HA (mouse monoclonal)	Invitrogen	Cat#:26183; RRID:AB_2533056	IP (3 µg per IP)
Antibody	Normal rabbit IgG	Millipore	Cat#:12–370; RRID:AB_145841	IP (15 µg per IP)

Continued on next page

Continued

Reagent type (species) or resource	Designation	Source or reference	Identifiers	Additional information
Antibody	Anti-βArrestin 2 (mouse monoclonal)	Santy Cruz Biotechnology	Cat#:sc-13140; RRID:AB_626701	WB (1 µg/ml)
Antibody	Anti-TRPC1 (rabbit polyclonal)	Other	4921	Gift from Veit Flockerzi Immunogen: N-terminus of mouse TRPC1, IP (15 µg per IP)
Antibody	Anti-TRPC3 (rabbit polyclonal)	Other	1378	Gift from Veit Flockerzi Immunogen: N-terminus of mouse TRPC3, IP (15 µg per IP)
Antibody	Anti-NMDAR1 (mouse monoclonal)	Millipore	Cat#:MAB1586; RRID:AB_11213180	IP (15 µg per IP)
Antibody	Anti-LRRTM2 (rabbit polyclonal),	ProteinTech	Cat#:23094–1-AP; RRID:AB_2879209	IP (15 µg per IP)
Antibody	Anti-DPP10 (mouse monoclonal)	Santa Cruz Biotechnology	sc-398108	IP (15 µg per IP)
Antibody	Anti-RGS9 (goat polyclonal)	Santa Cruz Biotechnology	sc-8143; RRID:AB_655555	IP (15 µg per IP)
Antibody	Anti-TRPM7 (mouse monoclonal)	Thermo Fisher Scientific	Cat#:MA5-27620; RRID:AB_2735401	IP (15 µg per IP)
Antibody	Anti-TRPM7 (mouse monoclonal)	NeuroMab	Cat#:75–114; RRID:AB_2877498	IP (15 µg per IP)
Antibody	Anti-(p)Ser1511 TRPM7 (mouse monoclonal)	DOI:10.1038/s41467-017-01960-z		Affinity purified with peptide H2N-DSPEVD(p)SKAALLPC-NH2, WB (2 µg/ml)
Antibody	Anti-M7c (rabbit polyclonal)	DOI:10.1038/s41467-017-01960-z		Affinity purified with peptide H2N-DSPEVDSKAALLPC-NH2, IP (15 µg per IP)
Antibody	Anti-M7d (2C7, mouse monoclonal)	This paper		See 'Materials and methods, Antibodies', IP (15 µg per IP), WB (0.8 µg/ml), IF (1.6 µg/ml)
Antibody	Anti-TRPM7 (4F9, mouse monoclonal)	This paper		See 'Materials and methods, Antibodies', WB (1.4 µg/ml)
Antibody	Anti-TRPM7 (rabbit polyclonal)	Millipore	Cat#:AB15562; RRID:AB_805460	WB (1 µg/ml)
Antibody	Anti-Flag (mouse monoclonal)	Sigma	Cat#:F3165; RRID:AB_259529	WB (1 µg/ml)
Antibody	Anti-βActin (rabbit polyclonal)	Bioss Inc	Cat#:bs-0061R; RRID:AB_10855480	WB (0.5 µg/ml)
Antibody	*Anti*-rabbit IgG (goat polyclonal, HRP conjugate)	abcam	ab7090	WB (1:30000)
Antibody	*Anti*-mouse IgG (goat polyclonal, HRP conjugate)	abcam	ab7068	WB (1:10000)
Antibody	*Anti*-mouse IgG (horse polyclonal, HRP conjugate)	Cell Signaling Technology	Cat#:7076	WB (1:1000)
Antibody	*Anti*-Na^+/K^+ ATPase (rabbit monoclonal, HRP conjugate)	Abcam	Cat#:ab185065	WB (1:1000)
Antibody	*Anti*-Myc (mouse monoclonal, clone 9B11)	Cell Signaling Technology	Cat#:2276	WB (1:1000)

Continued on next page

Continued

Reagent type (species) or resource	Designation	Source or reference	Identifiers	Additional information
Antibody	*Anti*-mouse IgG- Alexa Fluor 488 (goat IgG, Alexa Fluor 488 conjugate)	Thermo Fisher Scientific	Cat#:A11029	2 µg/ml
Recombinant DNA reagent	pT7-His_6-*Trpm7*-KD (plasmid)	This paper		See 'Materials and methods, Antibodies'
Peptide, recombinant protein	His_6-TRPM7-KD (purified protein)	This paper		See 'Materials and Methods, Antibodies'
Peptide, recombinant protein	TRPM7-KD (purified protein)	This paper		See 'Materials and methods, Antibodies'
Recombinant DNA reagent	Mouse *Trpm7* cDNA in pIRES2-EGFP vector (plasmid)	DOI: https://doi.org/10.1038/s41598-017-08144-1		Expression in mammalian cells
Recombinant DNA reagent	Mouse *Trpm6* cDNA in pIRES2-EGFP vector (plasmid)	DOI: https://doi.org/10.1038/s41598-017-08144-1		Expression in mammalian cells
Recombinant DNA reagent	Human *TRPM6* cDNA in pIRES2-EGFP vector (plasmid)	DOI: https://doi.org/10.1038/s41598-017-08144-1		Expression in mammalian cells
Recombinant DNA reagent	Mouse *Trpm7* cDNA in pOG1 vector (plasmid)	DOI: 10.1073/pnas.0305252101		cRNA synthesis
Recombinant DNA reagent	Mouse *Trpm7*-Myc cDNA in pcDNA3.1/V5-His TA-TOPO vector (plasmid)	DOI: 10.1073/pnas.0305252101		Expression in mammalian cells
Recombinant DNA reagent	Mouse *Trpm7*-HA cDNA in pcDNA3.1/V5-His TA-TOPO vector (plasmid)	DOI:10.1073/pnas.0305252101		Expression in mammalian cells
Recombinant DNA reagent	Human *TRPV1*-His cDNA in pNKS2 vector (plasmid)	This paper		See 'Materials and methods, Antibodies, Molecular biology' cRNA synthesis
Recombinant DNA reagent	Mouse *Cnnm1*-Myc-Flag in pCMV6-Entry (plasmid)	OriGene	Cat#:MR218318	Expression in mammalian cells
Recombinant DNA reagent	Mouse *Cnnm2*-Myc-Flag in pCMV6-Entry (plasmid)	OriGene	Cat#:MR218370	Expression in mammalian cells
Recombinant DNA reagent	Mouse *Cnnm3*-Myc-Flag in pCMV6-Entry (plasmid)	OriGene	Cat#:MR224758	Expression in mammalian cells, cRNA synthesis
Recombinant DNA reagent	Mouse *Cnnm4*-Myc-Flag in pCMV6-Entry (plasmid)	OriGene	Cat#:MR215721	Expression in mammalian cells
Recombinant DNA reagent	Mouse *Arl15*-Myc-Flag in pCMV6-Entry (plasmid)	OriGene	Cat#:MR218657	Expression in mammalian cells, cRNA synthesis
Recombinant DNA reagent	Mouse *Arl8a*-Myc-Flag in pCMV6-Entry (plasmid)	OriGene	Cat#:MR201740	Expression in mammalian cells, cRNA synthesis
Commercial assay or kit	Bio-Rad Protein Assay	Bio-Rad	Cat#:5000006	Protein concentration determination
Chemical compound, drug	ComplexioLyte CL-47	Logopharm	Cat#:CL-47–01	Mild detergent buffer
Chemical compound, drug	ComplexioLyte CL-91	Logopharm	Cat#:CL-91–01	Detergent buffer with intermediate stringency
Chemical compound, drug	Trypsin, sequencing grade modified	Promega	Cat#:V5111	
Chemical compound, drug	Leupeptin	Sigma	Cat#:L2884	

Continued on next page

Continued

Reagent type (species) or resource	Designation	Source or reference	Identifiers	Additional information
Chemical compound, drug	Pepstatin A	Sigma	Cat#:P5318	
Chemical compound, drug	Aprotinin	Roth	Cat#:A162.2	
Chemical compound, drug	Phenylmethylsulfonyl fluoride	Roth	Cat#:6367.3	
Chemical compound, drug	Iodoacetamide	Sigma	I6125	
Chemical compound, drug	Aminocaproic acid	Roth	3113.3	
Chemical compound, drug	TG100-115	Selleck Chemicals	Cat#:S1352	
Software, algorithm	msconvert.exe	http://proteowizard.sourceforge.net/		
Software, algorithm	MaxQuant v1.6.3	http://www.maxquant.org		
Software, algorithm	Mascot 2.6	Matrix Science, UK		
Software, algorithm	CellWorks 5.5.1	npi electronic https://www.npielectronic.com		
Software, algorithm	ZEN 2.3	Carl Zeiss https://www.zeiss.de		
Software, algorithm	PatchMaster 2 × 90	Harvard Bioscience https://www.heka.com		
Software, algorithm	Studio Lite 4.0	https://www.licor.com/bio/image-studio-lite		
Other	Dynabeads Protein A	Invitrogen	Cat#:10002D	
Other	Dynabeads Protein G	Invitrogen	Cat#:10004D	
Other	Tissue embedding media	Leica	Cat#:14020108926	Used to support gel slices during cryotomy

Antibodies

Antibodies used for APs were: *anti*-HA (11867423001, Roche) and *anti*-HA (26183, Invitrogen). TUC antibodies were: rabbit IgG (12–370, Millipore), *anti*-βArrestin 2 (sc-13140, Santa Cruz), *anti*-TRPC1 (4921, a gift from Veit Flockerzi), *anti*-Sac1 (ABFrontier), *anti*-TRPC3 (1378, a gift from Veit Flockerzi), *anti*-NMDAR1 (MAB1586, Sigma), *anti*-LRRTM2 (23094–1-AP, ProteinTech), *anti*-DPP10 (sc-398108, Santa Cruz), and *anti*-RGS9 (sc-8143, Santa Cruz).

Anti-TRPM7 mouse monoclonal antibody (anti-M7a, ***Figure 1A***) *was purchased from Thermo Fisher Scientific* (clone S74-25, Product # MA5-27620). *Anti*-TRPM7 mouse monoclonal antibody (*anti*-M7b, ***Figure 1A***) *was obtained from NeuroMab* (clone N74/25, Product # 75–114). Generation of a rabbit polyclonal *anti*-(p)Ser1511 TRPM7 antibody (*anti*-(p)Ser1511 M7, ***Figure 5***) was described previously (***Romagnani et al., 2017***). Briefly, rabbits were immunised with a phosphorylated peptide H2N-DSPEVD(**p**)SKAALLPC-NH2 ((p)Ser1511 in mouse TRPM7) coupled via its C-terminal cysteine residue to keyhole limpet hemocyanin (Eurogentec, Belgium). The generated serum was subjected to two rounds of affinity chromatography: a fraction of the antibody was purified using the phosphorylated peptide. Next, an additional round of chromatography was conducted using a non-phosphorylated variant of the peptide (H2N-DSPEVDSKAALLPC-NH2). The latter fraction of antibody was used in AP experiments (*anti*-M7c antibody, ***Figure 1A***).

Anti-TRPM7 2C7 mouse monoclonal antibody (*anti*-M7d, ***Figure 1A***, ***Figure 1—figure supplement 1***) was produced by Eurogentec (Belgium) as follows. The nucleotide sequence coding for His_6-tag followed by a cleavage site sequence for TEV protease and the amino acids 1501–1863 (kinase domain, KD) of mouse TRPM7 protein was synthesised in vitro and cloned into the prokaryotic expression

vector pT7. The resulting expression construct pT7-His_6-*Trpm7*-KD was verified by sequencing and transformed in *Escherichia coli* (BL21 DE3 pLysS). Next, the transformed *E. coli* strain was amplified in LB medium at 25°C; 1 mM IPTG was used for induction of the His_6-TRPM7-KD protein expression. The harvested cell pellet was disrupted by sonication. His_6-TRPM7-KD was identified in the soluble fraction of the lysate. His_6-TRPM7 was purified on an Ni Sepharose 6 Fast Flow column on an AKTA Avant 25 (GE Healthcare) using an imidazole gradient of 20–500 mM. The fraction containing His_6-TRPM7-KD was dialysed against a Tris buffer (0.5 mM EDTA, 1 mM DTT, and 50 mM Tris HCl pH 7.5). His_6-TRPM7-KD was subjected to TEV protease (New England Biolabs) digestion according to the manufacturer's instructions. Subsequently, non-digested His_6-TRPM7-KD and His_6-tagged fragments were removed using an Ni-Sepharose 6 Fast Flow column. The flow-through containing the cleaved TRPM7-KD was concentrated to 0.5 mg/ml in the Tris buffer and stored at –80°C. SDS-PAGE was used to verify the removal of the His_6-tag.

The standard mouse monoclonal antibody production program of Eurogentec (Belgium) was conducted to immunise four mice using the TRPM7-KD protein and to produce a library of hybridomas. ELISA and Western blot were used to screen the hybridomas and to perform a clonal selection. Two hybridoma clones, 2C7 and 4F9 (isotypes G1;K), were selected based on the antibody quality released in the culture medium. Both clones were propagated, and the corresponding cell culture media were collected for large-scale purification of the IgG fraction using Protein G affinity chromatography. The IgG fractions from 2C7 (0.8 mg/ml) and 4F9 (1.4 mg/ml) were dialysed in PBS and stored at –80°C. The specificity of the 2C7 and 4F9 IgGs (dilution 1:1000) was verified by Western blot analysis of HEK293T cells overexpressing the TRPM6 and TRPM7 proteins (***Figure 1—figure supplement 1***). The 2C7 antibody detected the mouse or human TRPM7, but not the mouse or human TRPM6 (***Figure 1—figure supplement 1***). In contrast, the 4F9 antibody detected only the mouse TRPM7 (***Figure 1—figure supplement 1***). Consequently, the 2C7 antibody (*anti*-M7d) was used in the present study.

Quantification of (p)Ser1511 TRPM7 and *anti*-M7d signals in ***Figure 5*** was performed using Image Studio Lite 4.0 software (https://www.licor.com/bio/image-studio-lite).

Molecular biology

Mouse *Trpm7*, mouse *Trpm6*, and human *TRPM6* cDNA in pIRES2-EGFP vector were reported previously (***Chubanov et al., 2004***; ***Ferioli et al., 2017***). cDNA encoding C-terminally His-tagged human *TRPV1* (NG_029716 ***Hayes et al., 2000***) was cloned into the pNKS2 vector (***Gloor et al., 1995***) using standard restriction enzyme (BamHI/SmaI) cloning techniques. The mouse *Trpm7* cDNA in the pOG1 and mouse *Trpm7-Myc* and *Trpm7-HA* cDNA variants in pcDNA3.1/V5-His TA-TOPO vector were described earlier (***Chubanov et al., 2004***; ***Ferioli et al., 2017***). Expression constructs encoding Myc-Flag-tagged (C-end) mouse *Cnnm1-4* and *Arl15*, and *Arl8A* cDNAs in the pCMV6-Entry expression vector were acquired from OriGene (MR218318 for *Cnnm1*, MR218370 for *Cnnm2*, MR224758 for *Cnnm3*, MR215721 for *Cnnm4*, MR218657 for *Arl15*, and MR201740 for *Arl8a*) and verified by sequencing. Point mutations in *Trpm7* were introduced using the QuikChange system (Thermo Fisher Scientific) according to the manufacturer's protocol and verified by sequencing (Eurofins, Germany).

Biochemistry

Cell lines, transient transfection: HEK293T cells (Sigma, 96121229, identity confirmed by STR profiling) were cultured at 37°C, 5% CO_2 in Dulbecco's modified Eagle's high glucose GlutaMAX medium (Gibco) supplemented with 10% foetal calf serum (Gibco), 1% penicillin/streptomycin (Gibco) and 10 mM Hepes (Gibco). *TRPM7*$^{-/-}$ HEK293T cells (***Abiria et al., 2017***) were cultured as WT cells with an addition of 10 mM $MgCl_2$, 3 µg/ml blasticidin S (InvivoGen), and 0.5 µg/ml puromycin (Gibco) to the medium. HEK293T-Rex cells stably expressing the human *TRPM7* were maintained as reported previously (***Schmitz et al., 2003***). The cell lines were tested negative for mycoplasma before use.

WT HEK293T cells were transfected with polyethylenimine (Polysciences) using a DNA to polyethylenimine ratio of 1:2.5. For transfection of *TRPM7*$^{-/-}$ HEK293T cells (***Abiria et al., 2017***), plasmid cDNA was diluted to 30 µg/ml in Hank's balanced salt solution, precipitated by addition of 113 mM $CaCl_2$ (final concentration) and added to the cells in culture medium lacking blasticidin S, puromycin, and 10 mM $MgCl_2$. For transfection, *Trpm7*, *Arl15*, and *Cnnm3* plasmid DNAs were mixed at a ratio of 3:1:1.

Preparation of plasma membrane-enriched protein fractions: Freshly excised brains from 25 male and 25 female 6-week-old rats (Wistar, Charles River) or mice (C57BL/6, Jackson Labs) were homogenised in homogenisation buffer (320 mM sucrose, 10 mM Tris/HCl pH 7.4, 1.5 mM $MgCl_2$, 1 mM EGTA and protease inhibitors leupeptin [Sigma], pepstatin A [Sigma], aprotinin [Roth] [1 µg/ml each], 1 mM phenylmethylsulfonyl fluoride [Roth], 1 mM iodoacetamide [Sigma]), particulates removed by centrifugation at 1080× *g* and homogenised material collected for 10 min at 200,000× *g*. After hypotonic lysis in 5 mM Tris/HCl pH 7.4 with protease inhibitors for 35 min on ice, the lysate was layered on top of a 0.5 and 1.3 M sucrose step gradient in 10 mM Tris/HCl pH 7.4, 1 mM EDTA/EGTA, and the plasma membrane-enriched fraction collected after centrifugation (45 min, 123,000× *g*) at the interface. Membranes were diluted in 20 mM Tris/HCl pH 7.4, collected by centrifugation (20 min, 200,000× *g*), and resuspended in 20 mM Tris/HCl pH7.4.

Cultured cells were harvested in phosphate buffer saline with protease inhibitors, collected by centrifugation (10 min, 500× *g*) and resuspended in homogenisation buffer. After sonication (2 × 5 pulses, duty 50, output 2 [Branson Sonifier 250]), membranes were pelleted for 20 min at 125,000× *g* and resuspended in 20 mM Tris/HCl pH 7.4. Protein concentration was determined with the Bio-Rad Protein Assay kit according to the manufacturer's instructions.

Immunoprecipitation: Membranes were resuspended in ComplexioLyte CL-47 or CL-91 solubilisation buffer (Logopharm) with added 1 mM EDTA/EGTA and protease inhibitors at a protein to detergent ratio of 1:8 and incubated for 30 min on ice. Solubilised protein was cleared by centrifugation (10 min, 125,000× *g*, 4°C) and incubated with antibodies cross-linked to Dynabeads (Invitrogen) by overhead rotation for 2 hr on ice. After two short washing steps with ComplexioLyte CL-47 dilution buffer (Logopharm), the captured protein was eluted in Laemmli buffer with dithiothreitol added after elution. Eluted proteins were separated by SDS-PAGE. For MS/MS analysis silver-stained (***Heukeshoven and Dernick, 1988***) protein lanes were cut-out, split at 50 kDa and pieces individually subjected to standard in-gel tryptic digestion (***Pandey and Mann, 2000***). For chemiluminescence detection, proteins were Western blotted onto PVDF membranes and probed with the following antibodies: *anti*-HA (11867423001, Roche), *anti*-Flag (F3165, Sigma), *anti*-βActin (bs-0061R, Bioss Inc).

BN-PAGE: Two-dimensional BN-PAGE/SDS-PAGE protein analysis was performed as described previously (***Schmidt et al., 2017***). Membrane protein fractions were solubilised in ComplexioLyte CL-47 as described above, salts exchanged for aminocaproic acid by centrifugation through a sucrose gradient, and samples loaded on non-denaturing 1–13% linear polyacrylamide gradient gels (anode buffer: 50 mM Bis-Tris, cathode buffer: 50 mM Tricine, 15 mM Bis-Tris, 0.02% Coomassie Blue G-250). For separation in the second dimension, individual gel lanes were isolated, equilibrated in 2× Laemmli buffer (10 min, 37°C), placed on top of SDS-PAGE gels and Western-probed using *anti*-TRPM7 (AB15562, Millipore).

Complexome profiling

The size distribution of solubilised native TRPM7-associated complexes was investigated using the high-resolution csBN-MS technique detailed in ***Faouzi et al., 2017***. Briefly, membranes isolated from adult mouse brain were solubilised with ComplexioLyte CL-47 (salt replaced by 750 mM aminocaproic acid), concentrated by ultracentrifugation into a 20%/50% sucrose cushion, supplied with 0.125% Coomassie G250 Blue and run overnight on a hyperbolic 1–13% polyacrylamide gel. The region of interest was excised from the lane, proteins fixed in 30% ethanol/15% acetic acid and the gel piece embedded in tissue embedding media (Leica). After careful mounting on a cryo-holder, 0.3 mm slices were harvested, rinsed, and subjected to in-gel tryptic digestion as described (***Faouzi et al., 2017***).

Mass spectrometry

Tryptic digests (dried peptides) were dissolved in 0.5% (v/v) trifluoroacetic acid and loaded onto a C18 PepMap100 precolumn (300 µm i.d. ×5 mm; particle size 5 µm) with 0.05% (v/v) trifluoroacetic acid (5 min 20 µl/min) using split-free UltiMate 3000 RSLCnano HPLCs (Dionex/Thermo Scientific, Germany). Bound peptides were then eluted with an aqueous-organic gradient (eluent A: 0.5% (v/v) acetic acid; eluent B: 0.5% (v/v) acetic acid in 80% (v/v) acetonitrile; times referring to AP-MS/csBN-MS): 5 min 3% B, 60/120 min from 3% B to 30% B, 15 min from 30% B to 99% B or 20 min from 30% B to 50% B and 10 min from 50% B to 99% B, respectively, 5 min 99% B, 5 min from 99% B to 3% B, 15/10 min 3% B (flow rate 300 nl/min). Eluted peptides were separated in a SilicaTip emitter (i.d.

75 µm; tip 8 µm; New Objective, Littleton, MA) manually packed 11 cm (AP-MS) or 23 cm (csBN-MS) with ReproSil-Pur 120 ODS-3 (C18; particle size 3 µm; Dr Maisch HPLC, Germany) and electrosprayed (2.3 kV; transfer capillary temperature 250/300°C) in positive ion mode into an Orbitrap Elite (AP-MS) or a Q Exactive HF-X (csBN-MS) mass spectrometer (both Thermo Scientific, Germany). Instrument settings: maximum MS/MS injection time = 200/400 ms; dynamic exclusion duration = 30/60 s; minimum signal/intensity threshold = 2000/40,000 (counts), top 10/15 precursors fragmented; isolation width = 1.0/1.4 m/z.

Peak lists were extracted from fragment ion spectra using the 'msconvert.exe' tool (part of ProteoWizard [***Chambers et al., 2012***]; http://proteowizard.sourceforge.net/; v3.0.6906 for Orbitrap Elite and v3.0.11098 for Q Exactive HF-X; Mascot generic format with filter options 'peakPicking true 1-' and 'threshold count 500 most-intense'). Precursor m/z values were preliminarily searched with 50 ppm peptide mass tolerance, their mass offset corrected by the median m/z offset of all peptides assigned, and afterwards searched with 5 ppm mass tolerance against all mouse, rat, and human (mouse/rat brain samples) or only human (HEK293T cell samples) entries of the UniProtKB/Swiss-Prot database. Acetyl (protein N-term), carbamidomethyl (C), Gln-> pyro Glu (N-term Q), Glu-> pyro Glu (N-term E), oxidation (M), phospho (S, T, Y), and propionamide (C) were chosen as variable modifications, and fragment mass tolerance was set to ±0.8 Da (Orbitrap Elite data) or ±20 mmu (Q Exactive HF-X data). One missed tryptic cleavage was allowed. The expect value cut-off for peptide assignment was set to 0.5. Related identified proteins (subset or species homologs) were grouped using the name of the predominant member. Proteins either representing exogenous contaminations (e.g., keratins, trypsin, IgG chains) or identified by only one specific peptide were not considered.

Label-free quantification of proteins was carried out as described in ***Bildl et al., 2012***; ***Müller et al., 2016***. Peptide signal intensities (peak volumes, PVs) from FT full scans were determined, and offline mass calibrated using MaxQuant v1.6.3 (http://www.maxquant.org). Then, peptide PV elution times were pairwise aligned using LOESS regression (reference times dynamically calculated from the median peptide elution times overall aligned datasets). Finally, PVs were assigned to peptides based on their m/z and elution time (±1 min/2–3 ppm, as obtained directly or indirectly from MS/MS-based identification) using in-house developed software. PV tables were then used to calculate protein abundance ratios in AP versus control (***Figure 1C***), the abundance norm value (***Figure 1B***, lower right) as an estimate for molecular abundance (both described in ***Schwenk et al., 2010***), and csBN-MS abundance profiles (***Figure 1B***, lower left) as detailed in ***Müller et al., 2016***. The latter were smoothed by sliding, averaging over a window of 5. Slice numbers were converted to apparent complex molecular weights by the sigmoidal fitting of (log(MW)) versus slice number of the observed profile peak maximum of mitochondrial marker protein complexes (***Schägger and Pfeiffer, 2000***).

Heterologous expression of TRPM7, CNNM3, ARL15, and ARL8A in *X. laevis* oocytes

TEVC measurements: *X. laevis* females were obtained from NASCO (Fort Atkinson, WI) and kept at the Core Facility Animal Models (CAM) of the Biomedical Center (BMC) of LMU Munich, Germany (Az:4.3.2–5682/LMU/BMC/CAM) in accordance with the EU Animal Welfare Act. To obtain oocytes, frogs were deeply anaesthetised in MS222 and killed by decapitation. Surgically extracted ovary lobes were dissociated by 2.5 hr incubation (RT) with gentle shaking in ND96 solution (96 mM NaCl, 2 mM KCl, 1 mM $CaCl_2$, 1 mM $MgCl_2$, 5 mM HEPES, pH 7.4) containing 2 mg/ml collagenase (Nordmark) and subsequently defolliculated by washing (15 min) with Ca^{2+}-free ND96. Stage V-VI oocytes were then selected and kept in ND96 containing 5 µg/ml gentamicin until further use.

TEVC measurements were performed as described previously (***Chubanov et al., 2004***) with a few modifications. Linearised cDNAs of *Trpm7* (in pOGI), *TRPV1* (in pNKS2), *Cnnm3, Arl8a*, and *Arl15* (all in pCMV6-Entry) were used for in vitro synthesis of cRNA (T7 or SP6 mMESSAGE mMACHINE transcription kits [Thermo Fisher Scientific]). In ***Figure 3A***, oocytes were injected with 5 ng of *Trpm7* cRNA or co-injected with 2.5 ng of *Cnnm3* (2:1 ratio), 2.5 ng *Arl15* (2:1 ratio), and 2.5 ng of *Cnnm3* with 2.5 ng of *Arl15* cRNAs (2:1:1 ratio). In ***Figure 3B***, oocytes were co-injected with 5 ng of *Trpm7* and 0.025–0.5 ng of *Arl15* cRNAs (200:1-10:1 ratio).

The injected oocytes were kept in ND96 solution, supplemented with 5 µg/ml gentamicin at 16°C. TEVC measurements were performed 3 days after injection at room temperature (RT) in Ca^{2+}/Mg^{2+}-free ND96 containing 3.0 mM $BaCl_2$ instead of $CaCl_2$ and $MgCl_2$ using a TURBO TEC-05X amplifier (npi

electronic) and CellWorks software (npi electronic). In some experiments, ND96 solution contained 3.0 mM $MgCl_2$ instead of 3.0 mM $BaCl_2$, as indicated in the corresponding figure legends. Oocytes were clamped at a holding potential of −60 mV, and 0.5 s ramps from −80 to +80 mV were applied at 6 s intervals. For statistical analysis, current amplitudes were extracted at –80 or +80 mV for individual oocytes, as indicated in the corresponding figure legends. Statistical significance (ANOVA) was calculated using GraphPad Prism 7.03.

Western blot: Oocytes *(n = 6 per group) were treated with* a lysis buffer (Pierce IP Lysis Buffer, Pierce) containing protease inhibitor and phosphatase inhibitor cocktails (Biotool), mixed (1:1) with 2× *Laemmli* buffer, heated at 70°C for 10 min, and cooled on ice. Samples were separated by SDS-PAGE (4–15% gradient Mini-PROTEAN, Bio-Rad) and electroblotted on nitrocellulose membranes (GE Healthcare Life Science). After blocking with 5% (w/v) non-fat dry milk in Tris-buffered saline with 0.1% Tween 20 (TBST). To probe for TRPM7 expression (***Figure 3D***), the upper part of the membrane was incubated with *anti*-M7d antibody (0.8 µg/ml) diluted in TBST with 5% (w/v) BSA, followed by washing in TBST, incubation with a horseradish peroxidase-coupled polyclonal horse anti-mouse IgG (#7076, Cell Signaling Technology; 1:1,000 in TBST with 5% (w/v) non-fat dry milk), and washing again in TBST. Blots were visualised using a luminescence imager (ChemiDoc Imaging System, Bio-Rad). The lower part of the membrane was developed using a horseradish peroxidase-coupled rabbit monoclonal *anti*-Na^+/K^+ ATPase antibody (ab185065, Abcam; 1:1000). To detect ARL15 (***Figure 3C***), the lower part of the membrane was incubated with a mouse *anti*-Myc antibody (clone 9B11, #2276, Cell Signaling Technology; 1:1000), and the upper part of the membrane was assessed by *anti*-Na^+/K^+ ATPase antibody.

Immunofluorescent staining: Oocytes *were* fixed in 4% (w/v) PFA (Electron Microscopy Sciences) in ND96 solution for 15 min at RT, followed by incubation in ice-cold methanol for 60 min at –18°C. After washing in ND96 (3×, RT), oocytes were incubated in ND96 containing 5% (w/v) BSA for 30 min at RT. *Anti*-M7d antibody (1.6 µg/ml in ND96 with 5% BSA) was applied overnight at 4°C. Afterwards, oocytes were washed in ND96 (3×, RT), and a goat *anti*-mouse IgG conjugated with Alexa Fluor 488 (Thermo Fisher Scientific; 2 µg/ml in ND96 with 5% BSA) was applied for 1 hr at RT. After washing in ND96 (3×, RT), differential interference contrast (DIC) and confocal images were obtained with a confocal laser scanning microscope LSM 880 AxioObserver (Carl Zeiss). We used a Plan-Apochromat 10×/0.45 objective, 488 nm excitation wavelengths and 493–630 nm filters. Acquired DIC and confocal images were analysed using the ZEN2.3 software (Carl Zeiss).

Patch-clamp experiments with HEK293T cells

WT HEK293T cells were cultured using 3 cm dishes and Dulbecco's modified Eagle's medium (DMEM, high glucose; Merck) supplemented with 10% FBS, 100 µg/ml streptomycin, 100 U/ml penicillin (all from Thermo Fisher Scientific). Cells were maintained in a humidified cell culture incubator (Heraeus, Thermo Fisher Scientific) at 37°C and 5% CO_2. To investigate the effect of CNNM3 on the TRPM7 channel, cells were transiently transfected by 2 µg *Trpm7* (in pIRES2-EGFP) or 2 µg *Trpm7* plus 0.5 µg *Cnnm3* (in pCMV6-Entry) expression constructs using Lipofectamine 2000 reagent (Thermo Fisher Scientific). To examine the effects of ARL15 on endogenous TRPM7 currents, HEK293T cells were transfected by 1 µg WT *Arl15* (in pCMV6-Entry) and 0.1 µg *EGFP* cDNAs (in pcDNA3.1/V5-His TA-TOPO).

Patch-clamp measurements were conducted with EGFP-positive cells 18–22 hr after transfection, as reported previously (***Chubanov et al., 2004***; ***Ferioli et al., 2017***), with minor modifications. Whole-cell currents were measured using an EPC10 patch-clamp amplifier and PatchMaster software (Harvard Bioscience). Voltages were corrected for a liquid junction potential of 10 mV. Currents were elicited by a ramp protocol from –100 to +100 mV over 50 ms acquired at 0.5 Hz and a holding potential of 0 mV. Inward and outward current amplitudes were extracted at –80 and +80 mV and were normalised to the cell size as pA/pF. Capacitance was measured using the automated capacitance cancellation function of EPC10. Patch pipettes were made of borosilicate glass (Science Products) and had resistance 2–3.5 MΩ. Unless stated otherwise, a standard extracellular solution contained (in mM): 140 NaCl, 2.8 KCl, 1 $CaCl_2$, 2 $MgCl_2$, 10 HEPES-NaOH, and 11 glucose (all from Sigma-Aldrich), pH 7.2. For assessing Mg^{2+} currents, the extracellular solutions contained (in mM): 10 HEPES-NaOH, 260 mannitol, and 10 $MgCl_2$, pH 7.2. Solutions were adjusted to 290 mOsm using a Vapro 5520 osmometer (Wescor Inc). The standard divalent cation-free intracellular pipette solution contained (in mM): 120 Cs-glutamate, 8 NaCl, 10 Cs-EGTA, 5 Cs-EDTA, 10 HEPES-CsOH (all from Sigma-Aldrich), pH

7.2. Data are presented as means ± standard error of the mean (means ± SEM). Statistical comparisons (Prism 8.4.0) were made using one-way ANOVA or a two-tailed t-test, as indicated in the figure legends. Significance was accepted at $p \leq 0.05$.

Determination of cellular Mg contents

The total content of Mg in *TRPM7*$^{-/-}$ HEK293T cells (***Abiria et al., 2017***) was determined by ICP-MS in ALS Scandinavia (Sweden) as reported previously (***Mittermeier et al., 2019***) with several modifications. The cells were cultured in DMEM (Merck) supplemented with 10% FBS, 100 µg/ml streptomycin, 100 U/ml penicillin, and 10 mM $MgCl_2$ (all from Thermo Fisher Scientific) in a humidified cell culture incubator (Heraeus, Thermo Fisher Scientific) at 37°C and 5% CO_2. To conduct ICP-MS experiments, *TRPM7*$^{-/-}$ HEK293T cells were plated in 10 cm^2 dishes at ~50% confluence in standard DMEM (without additional 10 mM Mg^{2+}) and transiently transfected with 20 µg *Trpm7*, 10 µg *Cnnm3*, or 20 µg *Trpm7* plus 10 µg *Cnnm3* plasmid cDNAs using Lipofectamine 2000 reagent (Thermo Fisher Scientific). After 24 hr, the cells were washed with serum-free DMEM, mechanically detached, and cell suspensions collected in 10 ml plastic tubes. After centrifugation (3 min, 1000 rpm), the medium was removed, and the cell pellet was resuspended in 5 ml PBS and passed to a fresh 10 ml tube. The cell suspension was centrifuged (3 min, 3500 rpm), the supernatant removed, and the cell pellet frozen at –20°C. Cell pellets were analysed by ICP-MS in ALS Scandinavia (Sweden). The experiment was repeated five times. Elementary Mg levels were normalised to elementary contents of sulphur (S) and represented as mean ± SEM. Data were compared by one-way ANOVA (Prism 8.4.0). Significance was accepted at $p \leq 0.05$.

Acknowledgements

VC, TG, SZ, US, and BF were supported by the Deutsche Forschungsgemeinschaft (German Research Foundation, DFG), TRR 152 (P02, P14 and P15). BF and US were supported by the DFG under Germany's Excellence Strategy (CIBSS-EXC2189 project ID: 390939984) and Project-ID 403222702 – SFB 1381. AN was supported by the DFG Project-ID 335447717 – SFB 1328 (P15). TG and AN were supported by Research Training Group 2338 (DFG). We thank Veit Flockerzi for *anti*-TRPC1/3 antibodies, David Clapham for *TRPM7*$^{-/-}$ HEK293T cells, Carsten Schmitz for HEK293T-REx cells stably expressing *TRPM7*, and Ilia Rodushkin for the support in ICP-MS. We thank Joanna Zaisserer, Lisa Pleninger, Yves Haufe, Monika Haberland, and Anna Erbacher for their technical assistance.

Additional information

Funding

Funder	Grant reference number	Author
Deutsche Forschungsgemeinschaft	TRR 152 P15	Vladimir Chubanov Thomas Gudermann
Deutsche Forschungsgemeinschaft	TRR 152 P02	Bernd Fakler Uwe Schulte
Deutsche Forschungsgemeinschaft	SFB 1328 P15	Annette Nicke
Deutsche Forschungsgemeinschaft	SFB 1381	Bernd Fakler
Deutsche Forschungsgemeinschaft	Research Training Group 2338	Thomas Gudermann Annette Nicke
Deutsche Forschungsgemeinschaft	TRR 152 P14	Susanna Zierler

The funders had no role in study design, data collection and interpretation, or the decision to submit the work for publication.

Author contributions

Astrid Kollewe, Data curation, Formal analysis, Investigation, Visualization, Writing – original draft, Writing – review and editing; Vladimir Chubanov, Conceptualization, Data curation, Funding acquisition, Investigation, Resources, Supervision, Writing – original draft, Writing – review and editing; Fong Tsuen Tseung, Leonor Correia, Eva Schmidt, Anna Rössig, Catrin Swantje Müller, Wolfgang Bildl, Investigation; Susanna Zierler, Data curation, Formal analysis, Methodology, Visualization; Alexander Haupt, Formal analysis, Investigation, Writing – review and editing; Uwe Schulte, Data curation, Formal analysis, Funding acquisition, Writing – review and editing; Annette Nicke, Data curation, Formal analysis, Methodology, Resources, Writing – review and editing; Bernd Fakler, Conceptualization, Data curation, Funding acquisition, Project administration, Resources, Writing – original draft, Writing – review and editing; Thomas Gudermann, Conceptualization, Data curation, Funding acquisition, Project administration, Writing – original draft, Writing – review and editing

Author ORCIDs

Vladimir Chubanov http://orcid.org/0000-0002-6042-4193
Alexander Haupt http://orcid.org/0000-0001-5647-5724
Annette Nicke http://orcid.org/0000-0001-6798-505X
Bernd Fakler http://orcid.org/0000-0001-7264-6423
Thomas Gudermann http://orcid.org/0000-0002-0323-7965

Decision letter and Author response

Decision letter https://doi.org/10.7554/eLife.68544.sa1
Author response https://doi.org/10.7554/eLife.68544.sa2

Additional files

Supplementary files

- Supplementary file 1. Numerical data for peak volumes, abundance norm values, relative abundance, and ratio distance values obtained through analysis of the mass spectrometry (MS) data.
- Supplementary file 2. Mass spectrometry (MS) spectra of phosphorylated transient receptor potential melastatin-subfamily member 7 (TRPM7), CNNM3, and CNNM4 peptides identified in affinity purifications (APs) from HEK293 and rodent brain.
- Supplementary file 3. Phosphorylation sites in transient receptor potential melastatin-subfamily member 7 (TRPM7), CNNM3, and CNNM4 identified in affinity purifications (APs) from transfected HEK293 cells and rodent brain. Excel file contains one worksheet: The phosphorylated residues of TRPM7, CNNM3, and CNNM4 identified by mass spectrometry (MS) in the present study are outlined in conjunction with previously published data (***Nguyen et al., 2019***; ***Zhou et al., 2013***; ***Cai et al., 2017***; ***Huttlin et al., 2010***).
- Transparent reporting form

Data availability

The mass spectrometry proteomics data have been deposited to the ProteomeXchange Consortium via the PRIDE partner repository with the dataset identifier PXD025279 and https://www.ebi.ac.uk/pride/archive/projects/PXD025279.

The following dataset was generated:

Author(s)	Year	Dataset title	Dataset URL	Database and Identifier
Haupt A, Fakler B	2021	The molecular appearance of native TRPM7 channel complexes identified by high-resolution proteomics	https://www.ebi.ac.uk/pride/archive/projects/PXD025279	PRIDE, PXD025279

References

Aarts M, Iihara K, Wei W-L, Xiong Z-G, Arundine M, Cerwinski W, MacDonald JF, Tymianski M. 2003. A key role for TRPM7 channels in anoxic neuronal death. *Cell* **115**: 863–877. DOI: https://doi.org/10.1016/s0092-8674(03)01017-1, PMID: 14697204

Abiria SA, Krapivinsky G, Sah R, Santa-Cruz AG, Chaudhuri D, Zhang J, Adstamongkonkul P, DeCaen PG, Clapham DE. 2017. TRPM7 senses oxidative stress to release Zn 2+ from unique intracellular vesicles. *PNAS* **114**: E6079–E6088. DOI: https://doi.org/10.1073/pnas.1707380114

Arjona FJ, de Baaij JHF. 2018. CrossTalk opposing view: CNNM proteins are not Na+ /Mg2+ exchangers but Mg2+ transport regulators playing a central role in transepithelial Mg2+ (re)absorption. *The Journal of Physiology* **596**: 747–750. DOI: https://doi.org/10.1113/JP275249, PMID: 29383729

Bildl W, Haupt A, Müller CS, Biniossek ML, Thumfart JO, Hüber B, Fakler B, Schulte U. 2012. Extending the dynamic range of label-free mass spectrometric quantification of affinity purifications. *Molecular & Cellular Proteomics* **11**: M111.007955. DOI: https://doi.org/10.1074/mcp.M111.007955, PMID: 22067099

Cai N, Bai Z, Nanda V, Runnels LW. 2017. Mass Spectrometric Analysis of TRPM6 and TRPM7 Phosphorylation Reveals Regulatory Mechanisms of the Channel-Kinases. *Scientific Reports* **7**: 42739. DOI: https://doi.org/10.1038/srep42739, PMID: 28220887

Chambers MC, Maclean B, Burke R, Amodei D, Ruderman DL, Neumann S, Gatto L, Fischer B, Pratt B, Egertson J, Hoff K, Kessner D, Tasman N, Shulman N, Frewen B, Baker TA, Brusniak MY, Paulse C, Creasy D, Flashner L, et al. 2012. A cross-platform toolkit for mass spectrometry and proteomics. *Nature Biotechnology* **30**:918–920. DOI: https://doi.org/10.1038/nbt.2377, PMID: 23051804

Chen YS, Kozlov G, Moeller BE, Rohaim A, Fakih R, Roux B, Burke JE, Gehring K. 2021. Crystal structure of an archaeal CorB magnesium transporter. *Nature Communications* **12**: 4028. DOI: https://doi.org/10.1038/s41467-021-24282-7, PMID: 34188059

Chubanov V, Waldegger S, Mederos y Schnitzler M, Vitzthum H, Sassen MC, Seyberth HW, Konrad M, Gudermann T. 2004. Disruption of TRPM6/TRPM7 complex formation by a mutation in the TRPM6 gene causes hypomagnesemia with secondary hypocalcemia. *PNAS* **101**: 2894–2899. DOI: https://doi.org/10.1073/pnas.0305252101, PMID: 14976260

Chubanov V, Gudermann T. 2014. Handbook of Experimental Pharmacology. Springer. DOI: https://doi.org/10.1007/978-3-642-54215-2_20, PMID: 24756719

Chubanov V, Ferioli S, Wisnowsky A, Simmons DG, Leitzinger C, Einer C, Jonas W, Shymkiv Y, Bartsch H, Braun A, Akdogan B, Mittermeier L, Sytik L, Torben F, Jurinovic V, van der Vorst EP, Weber C, Yildirim ÖA, Sotlar K, Schürmann A, et al. 2016. Epithelial magnesium transport by TRPM6 is essential for prenatal development and adult survival. *eLife* **5**: e20914. DOI: https://doi.org/10.7554/eLife.20914, PMID: 27991852

Chubanov V, Mittermeier L, Gudermann T. 2018. Role of kinase-coupled TRP channels in mineral homeostasis. *Pharmacology & Therapeutics* **184**: 159–176. DOI: https://doi.org/10.1016/j.pharmthera.2017.11.003, PMID: 29129644

Clark K, Middelbeek J, Dorovkov MV, Figdor CG, Ryazanov AG, Lasonder E, van Leeuwen FN. 2008. The alpha-kinases TRPM6 and TRPM7, but not eEF-2 kinase, phosphorylate the assembly domain of myosin IIA, IIB and IIC. *FEBS Letters* **582**: 2993–2997. DOI: https://doi.org/10.1016/j.febslet.2008.07.043, PMID: 18675813

Corre T, Arjona FJ, Hayward C, Youhanna S, de Baaij JHF, Belge H, Nägele N, Debaix H, Blanchard MG, Traglia M, Harris SE, Ulivi S, Rueedi R, Lamparter D, Macé A, Sala C, Lenarduzzi S, Ponte B, Pruijm M, Ackermann D, et al. 2018. Genome-Wide Meta-Analysis Unravels Interactions between Magnesium Homeostasis and Metabolic Phenotypes. *Journal of the American Society of Nephrology* **29**: 335–348. DOI: https://doi.org/10.1681/ASN.2017030267, PMID: 29093028

Desai BN, Krapivinsky G, Navarro B, Krapivinsky L, Carter BC, Febvay S, Delling M, Penumaka A, Ramsey IS, Manasian Y, Clapham DE. 2012. Cleavage of TRPM7 releases the kinase domain from the ion channel and regulates its participation in Fas-induced apoptosis. *Developmental Cell* **22**: 1149–1162. DOI: https://doi.org/10.1016/j.devcel.2012.04.006, PMID: 22698280

Dorovkov MV, Ryazanov AG. 2004. Phosphorylation of annexin I by TRPM7 channel-kinase. *The Journal of Biological Chemistry* **279**: 50643–50646. DOI: https://doi.org/10.1074/jbc.C400441200, PMID: 15485879

Duan J, Li Z, Li J, Hulse RE, Santa-Cruz A, Valinsky WC, Abiria SA, Krapivinsky G, Zhang J, Clapham DE. 2018. Structure of the mammalian TRPM7, a magnesium channel required during embryonic development. *PNAS* **115**: E8201–E8210. DOI: https://doi.org/10.1073/pnas.1810719115

Faouzi M, Kilch T, Horgen FD, Fleig A, Penner R. 2017. The TRPM7 channel kinase regulates store-operated calcium entry. *The Journal of Physiology* **595**: 3165–3180. DOI: https://doi.org/10.1113/JP274006, PMID: 28130783

Ferioli S, Zierler S, Zaißerer J, Schredelseker J, Gudermann T, Chubanov V. 2017. TRPM6 and TRPM7 differentially contribute to the relief of heteromeric TRPM6/7 channels from inhibition by cytosolic Mg2+ and Mg·ATP. *Scientific Reports* **7**: 8806. DOI: https://doi.org/10.1038/s41598-017-08144-1, PMID: 28821869

Fleig A, Chubanov V. 2014. Handbook of Experimental Pharmacology. Springer. DOI: https://doi.org/10.1007/978-3-642-54215-2_21, PMID: 24756720

Funato Y, Yamazaki D, Mizukami S, Du L, Kikuchi K, Miki H. 2014. Membrane protein CNNM4-dependent Mg2+ efflux suppresses tumor progression. *The Journal of Clinical Investigation* **124**: 5398–5410. DOI: https://doi.org/10.1172/JCI76614, PMID: 25347473

Funato Y, Miki H. 2019. Molecular function and biological importance of CNNM family Mg2+ transporters. *Journal of Biochemistry* **165**: 219–225. DOI: https://doi.org/10.1093/jb/mvy095, PMID: 30476181

Gillingham AK, Munro S. 2007. The small G proteins of the Arf family and their regulators. *Annual Review of Cell and Developmental Biology* **23**: 579–611. DOI: https://doi.org/10.1146/annurev.cellbio.23.090506.123209, PMID: 17506703

Giménez-Mascarell P, Oyenarte I, Hardy S, Breiderhoff T, Stuiver M, Kostantin E, Diercks T, Pey AL, Ereño-Orbea J, Martínez-Chantar ML, Khalaf-Nazzal R, Claverie-Martin F, Müller D, Tremblay ML,

Martínez-Cruz LA. 2017. Structural Basis of the Oncogenic Interaction of Phosphatase PRL-1 with the Magnesium Transporter CNNM2. *The Journal of Biological Chemistry* **292**: 786–801. DOI: https://doi.org/10.1074/jbc.M116.759944, PMID: 27899452

Giménez-Mascarell P, González-Recio I, Fernández-Rodríguez C, Oyenarte I, Müller D, Martínez-Chantar ML, Martínez-Cruz LA. 2019. Current Structural Knowledge on the CNNM Family of Magnesium Transport Mediators. *International Journal of Molecular Sciences* **20**: E1135. DOI: https://doi.org/10.3390/ijms20051135, PMID: 30845649

Gloor S, Pongs O, Schmalzing G. 1995. A vector for the synthesis of cRNAs encoding Myc epitope-tagged proteins in *Xenopus laevis* oocytes. *Gene* **160**: 213–217. DOI: https://doi.org/10.1016/0378-1119(95)00226-v, PMID: 7543868

Gulerez I, Funato Y, Wu H, Yang M, Kozlov G, Miki H, Gehring K. 2016. Phosphocysteine in the PRL-CNNM pathway mediates magnesium homeostasis. *EMBO Reports* **17**: 1890–1900. DOI: https://doi.org/10.15252/embr.201643393, PMID: 27856537

Hardy S, Uetani N, Wong N, Kostantin E, Labbé DP, Bégin LR, Mes-Masson A, Miranda-Saavedra D, Tremblay ML. 2015. The protein tyrosine phosphatase PRL-2 interacts with the magnesium transporter CNNM3 to promote oncogenesis. *Oncogene* **34**: 986–995. DOI: https://doi.org/10.1038/onc.2014.33, PMID: 24632616

Hayes P, Meadows HJ, Gunthorpe MJ, Harries MH, Duckworth MD, Cairns W, Harrison DC, Clarke CE, Ellington K, Prinjha RK, Barton AJL, Medhurst AD, Smith GD, Topp S, Murdock P, Sanger GJ, Terrett J, Jenkins O, Benham CD, Randall AD, et al. 2000. Cloning and functional expression of a human orthologue of rat vanilloid receptor-1. *Pain* **88**: 205–215. DOI: https://doi.org/10.1016/S0304-3959(00)00353-5, PMID: 11050376

Hermosura MC, Nayakanti H, Dorovkov MV, Calderon FR, Ryazanov AG, Haymer DS, Garruto RM. 2005. A TRPM7 variant shows altered sensitivity to magnesium that may contribute to the pathogenesis of two Guamanian neurodegenerative disorders. *PNAS* **102**: 11510–11515. DOI: https://doi.org/10.1073/pnas.0505149102, PMID: 16051700

Heukeshoven J, Dernick R. 1988. Improved silver staining procedure for fast staining in PhastSystem Development Unit. I. Staining of sodium dodecyl sulfate gels. *Electrophoresis* **9**: 28–32. DOI: https://doi.org/10.1002/elps.1150090106, PMID: 2466645

Hofmann T, Schäfer S, Linseisen M, Sytik L, Gudermann T, Chubanov V. 2014. Activation of TRPM7 channels by small molecules under physiological conditions. *Pflugers Archiv* **466**: 2177–2189. DOI: https://doi.org/10.1007/s00424-014-1488-0, PMID: 24633576

Huang Y, Jin F, Funato Y, Xu Z, Zhu W, Wang J, Sun M, Zhao Y, Yu Y, Miki H, Hattori M. 2021. Structural basis for the Mg 2+ recognition and regulation of the CorC Mg 2+ transporter. *Science Advances* **7**: abe6140. DOI: https://doi.org/10.1126/sciadv.abe6140

Huttlin EL, Jedrychowski MP, Elias JE, Goswami T, Rad R, Beausoleil SA, Villén J, Haas W, Sowa ME, Gygi SP. 2010. A tissue-specific atlas of mouse protein phosphorylation and expression. *Cell* **143**: 1174–1189. DOI: https://doi.org/10.1016/j.cell.2010.12.001, PMID: 21183079

Huttlin EL, Bruckner RJ, Paulo JA, Cannon JR, Ting L, Baltier K, Colby G, Gebreab F, Gygi MP, Parzen H, Szpyt J, Tam S, Zarraga G, Pontano-Vaites L, Swarup S, White AE, Schweppe DK, Rad R, Erickson BK, Obar RA, et al. 2017. Architecture of the human interactome defines protein communities and disease networks. *Nature* **545**: 505–509. DOI: https://doi.org/10.1038/nature22366, PMID: 28514442

Huttlin EL, Bruckner RJ, Navarrete-Perea J, Cannon JR, Baltier K, Gebreab F, Gygi MP, Thornock A, Zarraga G, Tam S, Szpyt J, Gassaway BM, Panov A, Parzen H, Fu S, Golbazi A, Maenpaa E, Stricker K, Guha Thakurta S, Zhang T, et al. 2021. Dual proteome-scale networks reveal cell-specific remodeling of the human interactome. *Cell* **184**: 3022-3040.. DOI: https://doi.org/10.1016/j.cell.2021.04.011, PMID: 33961781

Jin J, Desai BN, Navarro B, Donovan A, Andrews NC, Clapham DE. 2008. Deletion of Trpm7 disrupts embryonic development and thymopoiesis without altering Mg2+ homeostasis. *Science* **322**: 756–760. DOI: https://doi.org/10.1126/science.1163493, PMID: 18974357

Jin Jie, Wu L-J, Jun J, Cheng X, Xu H, Andrews NC, Clapham DE. 2012. The channel kinase, TRPM7, is required for early embryonic development. *PNAS* **109**: E225-E233. DOI: https://doi.org/10.1073/pnas.1120033109, PMID: 22203997

Kostantin E, Hardy S, Valinsky WC, Kompatscher A, de Baaij JHF, Zolotarov Y, Landry M, Uetani N, Martínez-Cruz LA, Hoenderop JGJ, Shrier A, Tremblay ML. 2016. Inhibition of PRL-2·CNNM3 Protein Complex Formation Decreases Breast Cancer Proliferation and Tumor Growth. *The Journal of Biological Chemistry* **291**: 10716–10725. DOI: https://doi.org/10.1074/jbc.M115.705863, PMID: 26969161

Krapivinsky G, Krapivinsky L, Manasian Y, Clapham DE. 2014. The TRPM7 chanzyme is cleaved to release a chromatin-modifying kinase. *Cell* **157**: 1061–1072. DOI: https://doi.org/10.1016/j.cell.2014.03.046, PMID: 24855944

Liu Y, Chen C, Liu Y, Li W, Wang Z, Sun Q, Zhou H, Chen X, Yu Y, Wang Y, Abumaria N. 2018. TRPM7 Is Required for Normal Synapse Density, Learning, and Memory at Different Developmental Stages. *Cell Reports* **23**: 3480–3491. DOI: https://doi.org/10.1016/j.celrep.2018.05.069, PMID: 29924992

Mederos y Schnitzler M, Wäring J, Gudermann T, Chubanov V. 2008. Evolutionary determinants of divergent calcium selectivity of TRPM channels. *FASEB Journal* **22**: 1540–1551. DOI: https://doi.org/10.1096/fj.07-9694com, PMID: 18073331

Mittermeier L, Demirkhanyan L, Stadlbauer B, Breit A, Recordati C, Hilgendorff A, Matsushita M, Braun A, Simmons DG, Zakharian E, Gudermann T, Chubanov V. 2019. TRPM7 is the central gatekeeper of intestinal

mineral absorption essential for postnatal survival. *PNAS* **116**: 4706–4715. DOI: https://doi.org/10.1073/pnas.1810633116, PMID: 30770447

Monteilh-Zoller MK, Hermosura MC, Nadler MJS, Scharenberg AM, Penner R, Fleig A. 2003. TRPM7 provides an ion channel mechanism for cellular entry of trace metal ions. *The Journal of General Physiology* **121**: 49–60. DOI: https://doi.org/10.1085/jgp.20028740, PMID: 12508053

Müller CS, Haupt A, Bildl W, Schindler J, Knaus H-G, Meissner M, Rammner B, Striessnig J, Flockerzi V, Fakler B, Schulte U. 2010. Quantitative proteomics of the Cav2 channel nano-environments in the mammalian brain. *PNAS* **107**: 14950–14957. DOI: https://doi.org/10.1073/pnas.1005940107, PMID: 20668236

Müller CS, Bildl W, Haupt A, Ellenrieder L, Becker T, Hunte C, Fakler B, Schulte U. 2016. Cryo-slicing Blue Native-Mass Spectrometry (csBN-MS), a Novel Technology for High Resolution Complexome Profiling. *Molecular & Cellular Proteomics* **15**:669–681. DOI: https://doi.org/10.1074/mcp.M115.054080, PMID: 26598645

Müller CS, Bildl W, Klugbauer N, Haupt A, Fakler B, Schulte U. 2019. High-Resolution Complexome Profiling by Cryoslicing BN-MS Analysis. *Journal of Visualized Experiments* **10**: 152. DOI: https://doi.org/10.3791/60096

Nadler MJ, Hermosura MC, Inabe K, Perraud AL, Zhu Q, Stokes AJ, Kurosaki T, Kinet JP, Penner R, Scharenberg AM, Fleig A. 2001. LTRPC7 is a Mg.ATP-regulated divalent cation channel required for cell viability. *Nature* **411**: 590–595. DOI: https://doi.org/10.1038/35079092, PMID: 11385574

Nguyen TTA, Li W, Park TJ, Gong LW, Cologna SM. 2019. Investigating Phosphorylation Patterns of the Ion Channel TRPM7 Using Multiple Extraction and Enrichment Techniques Reveals New Phosphosites. *Journal of the American Society for Mass Spectrometry* **30**: 1359–1367. DOI: https://doi.org/10.1007/s13361-019-02223-5, PMID: 31140077

Pandey A, Mann M. 2000. Proteomics to study genes and genomes. *Nature* **405**: 837–846. DOI: https://doi.org/10.1038/35015709, PMID: 10866210

Parry DA, Mighell AJ, El-Sayed W, Shore RC, Jalili IK, Dollfus H, Bloch-Zupan A, Carlos R, Carr IM, Downey LM, Blain KM, Mansfield DC, Shahrabi M, Heidari M, Aref P, Abbasi M, Michaelides M, Moore AT, Kirkham J, Inglehearn CF. 2009. Mutations in CNNM4 cause Jalili syndrome, consisting of autosomal-recessive cone-rod dystrophy and amelogenesis imperfecta. *American Journal of Human Genetics* **84**: 266–273. DOI: https://doi.org/10.1016/j.ajhg.2009.01.009, PMID: 19200525

Perraud AL, Zhao X, Ryazanov AG, Schmitz C. 2011. The channel-kinase TRPM7 regulates phosphorylation of the translational factor eEF2 via eEF2-k. *Cellular Signalling* **23**: 586–593. DOI: https://doi.org/10.1016/j.cellsig.2010.11.011, PMID: 21112387

Richards JB, Waterworth D, O'Rahilly S, Hivert M-F, Loos RJF, Perry JRB, Tanaka T, Timpson NJ, Semple RK, Soranzo N, Song K, Rocha N, Grundberg E, Dupuis J, Florez JC, Langenberg C, Prokopenko I, Saxena R, Sladek R, Aulchenko Y, et al. 2009. A genome-wide association study reveals variants in ARL15 that influence adiponectin levels. *PLOS Genetics* **5**: 12. DOI: https://doi.org/10.1371/journal.pgen.1000768, PMID: 20011104

Rivera B, Moreno C, Lavanderos B, Hwang JY, Fernández-Trillo J, Park K-S, Orio P, Viana F, Madrid R, Pertusa M. 2021. Constitutive Phosphorylation as a Key Regulator of TRPM8 Channel Function. *The Journal of Neuroscience* **41**: 8475–8493. DOI: https://doi.org/10.1523/JNEUROSCI.0345-21.2021, PMID: 34446569

Romagnani A, Vettore V, Rezzonico-Jost T, Hampe S, Rottoli E, Nadolni W, Perotti M, Meier MA, Hermanns C, Geiger S, Wennemuth G, Recordati C, Matsushita M, Muehlich S, Proietti M, Chubanov V, Gudermann T, Grassi F, Zierler S. 2017. TRPM7 kinase activity is essential for T cell colonization and alloreactivity in the gut. *Nature Communications* **8**: 1917. DOI: https://doi.org/10.1038/s41467-017-01960-z, PMID: 29203869

Runnels LW, Yue L, Clapham DE. 2001. TRP-PLIK, a bifunctional protein with kinase and ion channel activities. *Science* **291**: 1043–1047. DOI: https://doi.org/10.1126/science.1058519, PMID: 11161216

Runnels LW, Yue L, Clapham DE. 2002. The TRPM7 channel is inactivated by PIP(2) hydrolysis. *Nature Cell Biology* **4**: 329–336. DOI: https://doi.org/10.1038/ncb781, PMID: 11941371

Ryazanov AG, Ward MD, Mendola CE, Pavur KS, Dorovkov MV, Wiedmann M, Erdjument-Bromage H, Tempst P, Parmer TG, Prostko CR, Germino FJ, Hait WN. 1997. Identification of a new class of protein kinases represented by eukaryotic elongation factor-2 kinase. *PNAS* **94**: 4884–4889. DOI: https://doi.org/10.1073/pnas.94.10.4884, PMID: 9144159

Sah R, Mesirca P, Mason X, Gibson W, Bates-Withers C, Van den Boogert M, Chaudhuri D, Pu WT, Mangoni ME, Clapham DE. 2013a. Timing of myocardial trpm7 deletion during cardiogenesis variably disrupts adult ventricular function, conduction, and repolarization. *Circulation* **128**: 101–114. DOI: https://doi.org/10.1161/CIRCULATIONAHA.112.000768, PMID: 23734001

Sah R, Mesirca P, Van den Boogert M, Rosen J, Mably J, Mangoni ME, Clapham DE. 2013b. Ion channel-kinase TRPM7 is required for maintaining cardiac automaticity. *PNAS* **110**: E3037-E3046. DOI: https://doi.org/10.1073/pnas.1311865110, PMID: 23878236

Schägger H, Pfeiffer K. 2000. Supercomplexes in the respiratory chains of yeast and mammalian mitochondria. *The EMBO Journal* **19**: 1777–1783. DOI: https://doi.org/10.1093/emboj/19.8.1777, PMID: 10775262

Schmidt N, Kollewe A, Constantin CE, Henrich S, Ritzau-Jost A, Bildl W, Saalbach A, Hallermann S, Kulik A, Fakler B, Schulte U. 2017. Neuroplastin and Basigin Are Essential Auxiliary Subunits of Plasma Membrane Ca2+-ATPases and Key Regulators of Ca2+ Clearance. *Neuron* **96**: 827-838.. DOI: https://doi.org/10.1016/j.neuron.2017.09.038, PMID: 29056295

Schmitz C, Perraud A-L, Johnson CO, Inabe K, Smith MK, Penner R, Kurosaki T, Fleig A, Scharenberg AM. 2003. Regulation of vertebrate cellular Mg2+ homeostasis by TRPM7. *Cell* **114**: 191–200. DOI: https://doi.org/10.1016/s0092-8674(03)00556-7, PMID: 12887921

Schwenk J, Metz M, Zolles G, Turecek R, Fritzius T, Bildl W, Tarusawa E, Kulik A, Unger A, Ivankova K, Seddik R, Tiao JY, Rajalu M, Trojanova J, Rohde V, Gassmann M, Schulte U, Fakler B, Bettler B. 2010. Native GABA(B)

receptors are heteromultimers with a family of auxiliary subunits. *Nature* **465**: 231–235. DOI: https://doi.org/10.1038/nature08964, PMID: 20400944

Schwenk J, Harmel N, Brechet A, Zolles G, Berkefeld H, Müller CS, Bildl W, Baehrens D, Hüber B, Kulik A, Klöcker N, Schulte U, Fakler B. 2012. High-resolution proteomics unravel architecture and molecular diversity of native AMPA receptor complexes. *Neuron* **74**: 621–633. DOI: https://doi.org/10.1016/j.neuron.2012.03.034, PMID: 22632720

Schwenk J, Pérez-Garci E, Schneider A, Kollewe A, Gauthier-Kemper A, Fritzius T, Raveh A, Dinamarca MC, Hanuschkin A, Bildl W, Klingauf J, Gassmann M, Schulte U, Bettler B, Fakler B. 2016. Modular composition and dynamics of native GABAB receptors identified by high-resolution proteomics. *Nature Neuroscience* **19**: 233–242. DOI: https://doi.org/10.1038/nn.4198, PMID: 26691831

Song C, Bae Y, Jun J, Lee H, Kim ND, Lee K-B, Hur W, Park J-Y, Sim T. 2017. Identification of TG100-115 as a new and potent TRPM7 kinase inhibitor, which suppresses breast cancer cell migration and invasion. *Biochimica et Biophysica Acta. General Subjects* **1861**: 947–957. DOI: https://doi.org/10.1016/j.bbagen.2017.01.034, PMID: 28161478

Stritt S, Nurden P, Favier R, Favier M, Ferioli S, Gotru SK, van Eeuwijk JMM, Schulze H, Nurden AT, Lambert MP, Turro E, Burger-Stritt S, Matsushita M, Mittermeier L, Ballerini P, Zierler S, Laffan MA, Chubanov V, Gudermann T, Nieswandt B, et al. 2016. Defects in TRPM7 channel function deregulate thrombopoiesis through altered cellular Mg(2+) homeostasis and cytoskeletal architecture. *Nature Communications* **7**: 11097. DOI: https://doi.org/10.1038/ncomms11097, PMID: 27020697

Stuiver M, Lainez S, Will C, Terryn S, Günzel D, Debaix H, Sommer K, Kopplin K, Thumfart J, Kampik NB, Querfeld U, Willnow TE, Němec V, Wagner CA, Hoenderop JG, Devuyst O, Knoers NVAM, Bindels RJ, Meij IC, Müller D. 2011. CNNM2, encoding a basolateral protein required for renal Mg2+ handling, is mutated in dominant hypomagnesemia. *American Journal of Human Genetics* **88**: 333–343. DOI: https://doi.org/10.1016/j.ajhg.2011.02.005, PMID: 21397062

Sun H-S, Jackson MF, Martin LJ, Jansen K, Teves L, Cui H, Kiyonaka S, Mori Y, Jones M, Forder JP, Golde TE, Orser BA, Macdonald JF, Tymianski M. 2009. Suppression of hippocampal TRPM7 protein prevents delayed neuronal death in brain ischemia. *Nature Neuroscience* **12**: 1300–1307. DOI: https://doi.org/10.1038/nn.2395, PMID: 19734892

Voringer S, Schreyer L, Nadolni W, Meier MA, Woerther K, Mittermeier C, Ferioli S, Singer S, Holzer K, Zierler S, Chubanov V, Liebl B, Gudermann T, Muehlich S. 2020. Inhibition of TRPM7 blocks MRTF/SRF-dependent transcriptional and tumorigenic activity. *Oncogene* **39**: 2328–2344. DOI: https://doi.org/10.1038/s41388-019-1140-8, PMID: 31844251

Yamazaki D, Funato Y, Miura J, Sato S, Toyosawa S, Furutani K, Kurachi Y, Omori Y, Furukawa T, Tsuda T, Kuwabata S, Mizukami S, Kikuchi K, Miki H. 2013. Basolateral Mg2+ extrusion via CNNM4 mediates transcellular Mg2+ transport across epithelia: a mouse model. *PLOS Genetics* **9**: 12. DOI: https://doi.org/10.1371/journal.pgen.1003983, PMID: 24339795

Zhang H, Kozlov G, Li X, Wu H, Gulerez I, Gehring K. 2017. PRL3 phosphatase active site is required for binding the putative magnesium transporter CNNM3. *Scientific Reports* **7**: 48. DOI: https://doi.org/10.1038/s41598-017-00147-2

Zhou H, Di Palma S, Preisinger C, Peng M, Polat AN, Heck AJR, Mohammed S. 2013. Toward a comprehensive characterization of a human cancer cell phosphoproteome. *Journal of Proteome Research* **12**: 260–271. DOI: https://doi.org/10.1021/pr300630k, PMID: 23186163

7.1 Supplementary figures publication 2

In this chapter I only included supplementary figures I produced myself.

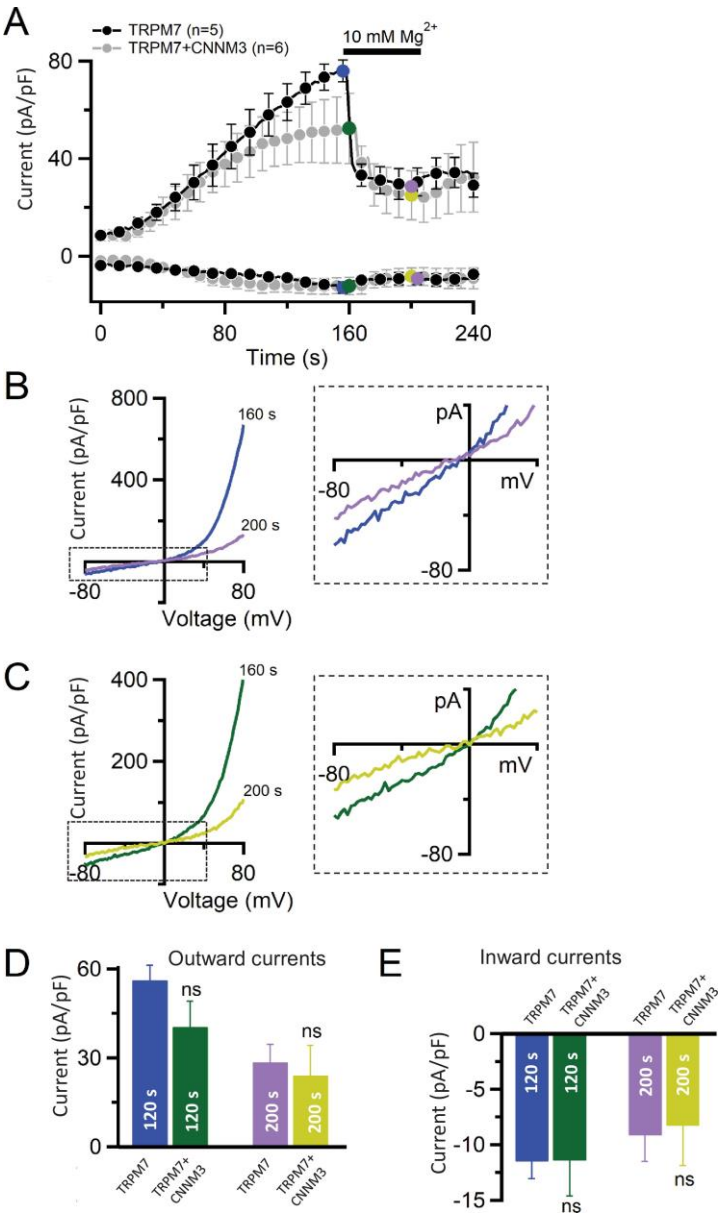

Figure 4-figure supplement 1. Heterologous expression of TRPM7 and CNNM3 in HEK293T cells. (**A**) Whole-cell currents were recorded in cells transfected by TRPM7 or TRPM7 with CNNM3 using the standard Mg^{2+}-free internal solution and standard external solution. When currents were developed, the cells were exposed to the external solution containing 10 mM Mg^{2+} as indicated by a black bar. Current amplitudes (mean ± SEM) were acquired at -80 and +80 mV and plotted over time. (**B, C**) Representative I-V relationships of currents in (A) at 160 s and 200 s in cells transfected by TRPM7 (B) or TRPM7 with CNNM3 (C). The dashed boxes in the *Left panels* indicate areas of inward currents enlarged in the *Right panels.* (**D**) Bar graphs of outward (+80 mV, mean ± SEM) and inward (+80 mV, mean ± SEM) currents were obtained before and after the application of 10 mM Mg^{2+} as indicated in (A). n, number of cells measured. ns, not significant (two-tailed t-test).

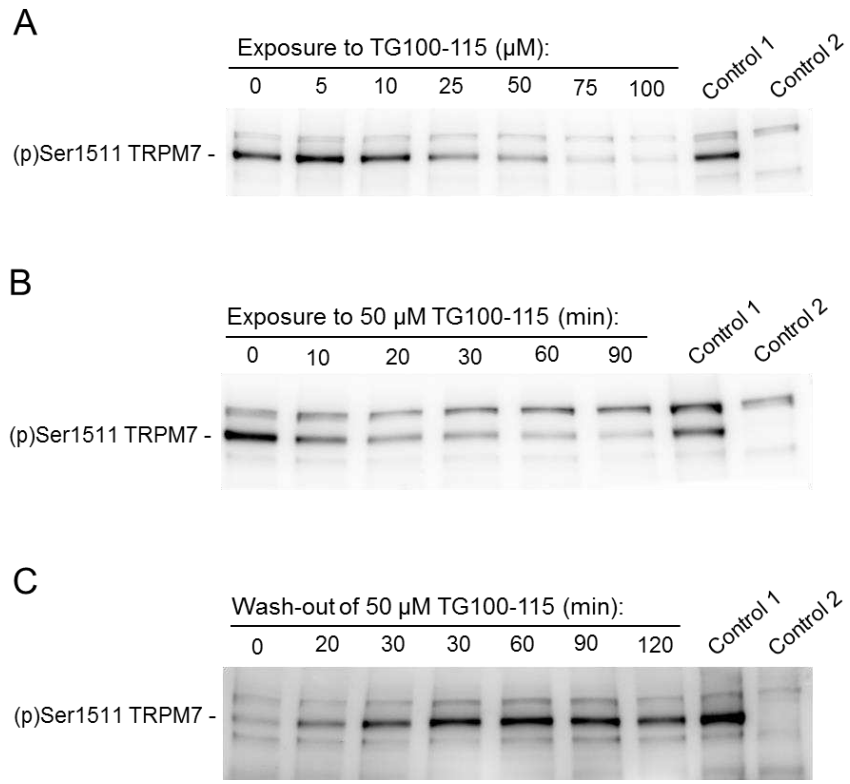

Figure 5-figure supplement 1. Effects of TG100-115 on the autophosphorylation of TRPM7.

(**A**) Dose-dependent inhibitory effects of TG100-115 on the autophosphorylation of TRPM7. HEK293 cells were transiently transfected by TRPM7 cDNA. 24 h after transfection, the indicated concentrations of TG100-115 were added to the cell culture medium, cells were cultured for an additional 12 h and immunoreactivity of (p)Ser1511 in TRPM7 was detected in cell lysates using the *anti*-M7c antibody. (**B**) Time-dependent action of TG100-115 on (p)Ser1511-TRPM7 levels. TRPM7-transfected cells were exposed to the cell culture medium containing 50 μM TG100-115 during 10-60 min at room temperature, and cell lysates were examined as in (A). (**C**) Reversibility of TG100-115 effects on the autophosphorylation of TRPM7.

TRPM7-transfected cells were exposed to the cell culture medium containing 50 μM TG100-115 for 2 h. Afterwards, the cells were washed with a fresh medium and incubated without TG100-115 for 20-120 min at room temperature. Immunoreactivity of (p)Ser1511 in TRPM7 was detected as in (A). To verify the specificity of the TRPM7 signal, lysates from TRPM7-transfected and untransfected cells were used (correspondently, Control 1 and Control 2). Representative results are shown from two independent experiments. Note: In contrast to (p)Ser1511 signal, unspecific bands were equally detectable in all samples examined.

8. References

1. Schmidt E, Narangoda C, Nörenberg W, Egawa M, Rössig A, Leonhardt M, et al. Structural mechanism of TRPM7 channel regulation by intracellular magnesium. Cellular and Molecular Life Sciences 2022;79(225).
2. Autzen HE, Myasnikov AG, Campbell MG, Asarnow D, Julius D, Cheng Y. Structure of the human TRPM4 ion channel in a lipid nanodisc. Science. 2018;359(6372):228-32.
3. Demeuse P, Penner R, Fleig A. TRPM7 channel is regulated by magnesium nucleotides via its kinase domain. The Journal of general physiology. 2006;127(4):421-34.
4. Diver MM, Cheng Y, Julius D. Structural insights into TRPM8 inhibition and desensitization. Science. 2019;365(6460):1434-40.
5. Duan J, Li Z, Li J, Santa-Cruz A, Sanchez-Martinez S, Zhang J, et al. Structure of full-length human TRPM4. Proceedings of the National Academy of Sciences. 2018;115(10):2377-82.
6. Guo J, She J, Zeng W, Chen Q, Bai X-c, Jiang Y. Structures of the calcium-activated, non-selective cation channel TRPM4. Nature. 2017;552(7684):205-9.
7. Wang L, Fu T-M, Zhou Y, Xia S, Greka A, Wu H. Structures and gating mechanism of human TRPM2. Science. 2018;362(6421):eaav4809.
8. Winkler PA, Huang Y, Sun W, Du J, Lü W. Electron cryo-microscopy structure of a human TRPM4 channel. Nature. 2017;552(7684):200-4.
9. Yin Y, Le SC, Hsu AL, Borgnia MJ, Yang H, Lee S-Y. Structural basis of cooling agent and lipid sensing by the cold-activated TRPM8 channel. Science. 2019;363(6430):eaav9334.
10. Zhang Z, Tóth B, Szollosi A, Chen J, Csanády L. Structure of a TRPM2 channel in complex with Ca2+ explains unique gating regulation. Elife. 2018;7:e36409.
11. Kozak JA, Matsushita M, Nairn AC, Cahalan MD. Charge screening by internal pH and polyvalent cations as a mechanism for activation, inhibition, and rundown of TRPM7/MIC channels. The Journal of general physiology. 2005;126(5):499-514.
12. Hofmann T, Schäfer S, Linseisen M, Sytik L, Gudermann T, Chubanov V. Activation of TRPM7 channels by small molecules under physiological conditions. Pflügers Archiv-European Journal of Physiology. 2014;466(12):2177-89.
13. Chubanov V, Mederos y Schnitzler M, Meißner M, Schäfer S, Abstiens K, Hofmann T, et al. Natural and synthetic modulators of SK (Kca2) potassium channels inhibit magnesium-dependent activity of the kinase-coupled cation channel TRPM7. British journal of pharmacology. 2012;166(4):1357-76.
14. Murata Y, Iwasaki H, Sasaki M, Inaba K, Okamura Y. Phosphoinositide phosphatase activity coupled to an intrinsic voltage sensor. Nature. 2005;435(7046):1239-43.
15. Nadler MJ, Hermosura MC, Inabe K, Perraud A-L, Zhu Q, Stokes AJ, et al. LTRPC7 is a Mg· ATP-regulated divalent cation channel required for cell viability. Nature. 2001;411(6837):590-5.
16. Kollewe A, Chubanov V, Tseung FT, Correia L, Schmidt E, Rössig A, et al. The molecular appearance of native TRPM7 channel complexes identified by high-resolution proteomics. Elife. 2021;10:e68544.
17. Romagnani A, Vettore V, Rezzonico-Jost T, Hampe S, Rottoli E, Nadolni W, et al. TRPM7 kinase activity is essential for T cell colonization and alloreactivity in the gut. Nature communications. 2017;8(1):1-14.

18. Song C, Bae Y, Jun J, Lee H, Kim ND, Lee K-B, et al. Identification of TG100-115 as a new and potent TRPM7 kinase inhibitor, which suppresses breast cancer cell migration and invasion. Biochimica et Biophysica Acta (BBA)-General Subjects. 2017;1861(4):947-57.
19. Owsianik G, Talavera K, Voets T, Nilius B. Permeation and selectivity of TRP channels. Annu Rev Physiol. 2006;68:685-717.
20. Venkatachalam K, Montell C. TRP channels. Annu Rev Biochem. 2007;76:387-417.
21. Grimm C, Kraft R, Sauerbruch S, Schultz Gn, Harteneck C. Molecular and functional characterization of the melastatin-related cation channel TRPM3. Journal of Biological Chemistry. 2003;278(24):21493-501.
22. Vriens J, Owsianik G, Hofmann T, Philipp SE, Stab J, Chen X, et al. TRPM3 is a nociceptor channel involved in the detection of noxious heat. Neuron. 2011;70(3):482-94.
23. Held K, Voets T, Vriens J. TRPM3 in temperature sensing and beyond. Temperature. 2015;2(2):201-13.
24. Naylor J, Li J, Milligan CJ, Zeng F, Sukumar P, Hou B, et al. Pregnenolone sulphate-and cholesterol-regulated TRPM3 channels coupled to vascular smooth muscle secretion and contraction. Circulation research. 2010;106(9):1507-15.
25. Perraud A-L, Fleig A, Dunn CA, Bagley LA, Launay P, Schmitz C, et al. ADP-ribose gating of the calcium-permeable LTRPC2 channel revealed by Nudix motif homology. Nature. 2001;411(6837):595-9.
26. Sano Y, Inamura K, Miyake A, Mochizuki S, Yokoi H, Matsushime H, et al. Immunocyte Ca2+ influx system mediated by LTRPC2. Science. 2001;293(5533):1327-30.
27. Hara Y, Wakamori M, Ishii M, Maeno E, Nishida M, Yoshida T, et al. LTRPC2 Ca2+-permeable channel activated by changes in redox status confers susceptibility to cell death. Molecular cell. 2002;9(1):163-73.
28. Wehage E, Eisfeld Jr, Heiner I, Jüngling E, Zitt C, Lückhoff A. Activation of the cation channel long transient receptor potential channel 2 (LTRPC2) by hydrogen peroxide: a splice variant reveals a mode of activation independent of ADP-ribose. Journal of Biological Chemistry. 2002;277(26):23150-6.
29. McKemy DD. TRPM8: the cold and menthol receptor. TRP ion channel function in sensory transduction and cellular signaling cascades. 2007.
30. McKemy DD, Neuhausser WM, Julius D. Identification of a cold receptor reveals a general role for TRP channels in thermosensation. Nature. 2002;416(6876):52-8.
31. Peier AM, Moqrich A, Hergarden AC, Reeve AJ, Andersson DA, Story GM, et al. A TRP channel that senses cold stimuli and menthol. Cell. 2002;108(5):705-15.
32. Hofmann T, Chubanov V, Gudermann T, Montell C. TRPM5 is a voltage-modulated and Ca2+-activated monovalent selective cation channel. Current biology. 2003;13(13):1153-8.
33. Launay P, Fleig A, Perraud A-L, Scharenberg AM, Penner R, Kinet J-P. TRPM4 is a Ca2+-activated nonselective cation channel mediating cell membrane depolarization. Cell. 2002;109(3):397-407.
34. Chubanov V, y Schnitzler MM, Wäring J, Plank A, Gudermann T. Emerging roles of TRPM6/TRPM7 channel kinase signal transduction complexes. Naunyn-Schmiedeberg's archives of pharmacology. 2005;371(4):334-41.
35. Monteilh-Zoller MK, Hermosura MC, Nadler MJ, Scharenberg AM, Penner R, Fleig A. TRPM7 provides an ion channel mechanism for cellular entry of trace metal ions. The Journal of general physiology. 2003;121(1):49-60.

36. Chubanov V, Waldegger S, y Schnitzler MM, Vitzthum H, Sassen MC, Seyberth HW, et al. Disruption of TRPM6/TRPM7 complex formation by a mutation in the TRPM6 gene causes hypomagnesemia with secondary hypocalcemia. Proceedings of the National Academy of Sciences. 2004;101(9):2894-9.
37. Pedersen SF, Owsianik G, Nilius B. TRP channels: an overview. Cell calcium. 2005;38(3-4):233-52.
38. Schlingmann KP, Waldegger S, Konrad M, Chubanov V, Gudermann T. TRPM6 and TRPM7—Gatekeepers of human magnesium metabolism. Biochimica et Biophysica Acta (BBA)-Molecular Basis of Disease. 2007;1772(8):813-21.
39. Schlingmann KP, Weber S, Peters M, Nejsum LN, Vitzthum H, Klingel K, et al. Hypomagnesemia with secondary hypocalcemia is caused by mutations in TRPM6, a new member of the TRPM gene family. Nature genetics. 2002;31(2):166-70.
40. Walder RY, Landau D, Meyer P, Shalev H, Tsolia M, Borochowitz Z, et al. Mutation of TRPM6 causes familial hypomagnesemia with secondary hypocalcemia. Nature genetics. 2002;31(2):171-4.
41. Gees M, Colsoul B, Nilius B. The role of transient receptor potential cation channels in Ca2+ signaling. Cold Spring Harbor perspectives in biology. 2010;2(10):a003962.
42. Chubanov V, Ferioli S, Wisnowsky A, Simmons DG, Leitzinger C, Einer C, et al. Epithelial magnesium transport by TRPM6 is essential for prenatal development and adult survival. Elife. 2016;5:e20914.
43. Chubanov V, Mittermeier L, Gudermann T. Role of kinase-coupled TRP channels in mineral homeostasis. Pharmacology & Therapeutics. 2018;184:159-76.
44. Chubanov V, Waldegger S, Schnitzler MMy, Vitzthum H, Sassen MC, Seyberth HW, et al. Disruption of TRPM6/TRPM7 complex formation by a mutation in the TRPM6 gene causes hypomagnesemia with secondary hypocalcemia. Proceedings of the National Academy of Sciences. 2004;101(9):2894-9.
45. Mittermeier L, Demirkhanyan L, Stadlbauer B, Breit A, Recordati C, Hilgendorff A, et al. TRPM7 is the central gatekeeper of intestinal mineral absorption essential for postnatal survival. Proceedings of the National Academy of Sciences. 2019;116(10):4706-15.
46. Ryazanova LV, Rondon LJ, Zierler S, Hu Z, Galli J, Yamaguchi TP, et al. TRPM7 is essential for Mg2+ homeostasis in mammals. Nature communications. 2010;1(1):1-9.
47. Schlingmann KP, Weber S, Peters M, Niemann Nejsum L, Vitzthum H, Klingel K, et al. Hypomagnesemia with secondary hypocalcemia is caused by mutations in TRPM6, a new member of the TRPM gene family. Nature genetics. 2002;31(2):166-70.
48. Stritt S, Nurden P, Favier R, Favier M, Ferioli S, Gotru SK, et al. Defects in TRPM7 channel function deregulate thrombopoiesis through altered cellular Mg2+ homeostasis and cytoskeletal architecture. Nature communications. 2016;7(1):1-13.
49. Stritt S, Nurden P, Favier R, Favier M, Ferioli S, Gotru SK, et al. Defects in TRPM7 channel function deregulate thrombopoiesis through altered cellular Mg 2+ homeostasis and cytoskeletal architecture. Nature communications. 2016;7(1):1-13.
50. Fujiwara Y, Minor Jr DL. X-ray crystal structure of a TRPM assembly domain reveals an antiparallel four-stranded coiled-coil. Journal of molecular biology. 2008;383(4):854-70.
51. Ferioli S, Zierler S, Zaißerer J, Schredelseker J, Gudermann T, Chubanov V. TRPM6 and TRPM7 differentially contribute to the relief of heteromeric TRPM6/7 channels from inhibition by cytosolic Mg 2+ and Mg· ATP. Scientific reports. 2017;7(1):1-19.

52. Lück-Vielmetter D, Schleicher M, Grabatin B, Wippler J, Gerisch G. Replacement of threonine residues by serine and alanine in a phosphorylatable heavy chain fragment of Dictyostelium myosin II. FEBS letters. 1990;269(1):239-43.
53. Vaillancourt JP, Lyons C, Côté G. Identification of two phosphorylated threonines in the tail region of Dictyostelium myosin II. Journal of Biological Chemistry. 1988;263(21):10082-7.
54. Middelbeek J, Clark K, Venselaar H, Huynen MA, Van Leeuwen FN. The alpha-kinase family: an exceptional branch on the protein kinase tree. Cellular and molecular life sciences. 2010;67(6):875-90.
55. Clark K, Middelbeek J, Dorovkov MV, Figdor CG, Ryazanov AG, Lasonder E, et al. The α-kinases TRPM6 and TRPM7, but not eEF-2 kinase, phosphorylate the assembly domain of myosin IIA, IIB and IIC. FEBS letters. 2008;582(20):2993-7.
56. Dorovkov MV, Ryazanov AG. Phosphorylation of annexin I by TRPM7 channel-kinase. Journal of Biological Chemistry. 2004;279(49):50643-6.
57. Faouzi M, Kilch T, Horgen FD, Fleig A, Penner R. The TRPM7 channel kinase regulates store-operated calcium entry. The Journal of physiology. 2017;595(10):3165-80.
58. Perraud A-L, Zhao X, Ryazanov AG, Schmitz C. The channel-kinase TRPM7 regulates phosphorylation of the translational factor eEF2 via eEF2-k. Cellular signalling. 2011;23(3):586-93.
59. Runnels LW, Yue L, Clapham DE. TRP-PLIK, a bifunctional protein with kinase and ion channel activities. Science. 2001;291(5506):1043-7.
60. Voringer S, Schreyer L, Nadolni W, Meier MA, Woerther K, Mittermeier C, et al. Inhibition of TRPM7 blocks MRTF/SRF-dependent transcriptional and tumorigenic activity. Oncogene. 2020;39(11):2328-44.
61. Desai BN, Krapivinsky G, Navarro B, Krapivinsky L, Carter BC, Febvay S, et al. Cleavage of TRPM7 releases the kinase domain from the ion channel and regulates its participation in Fas-induced apoptosis. Developmental cell. 2012;22(6):1149-62.
62. Krapivinsky G, Krapivinsky L, Manasian Y, Clapham DE. The TRPM7 chanzyme is cleaved to release a chromatin-modifying kinase. Cell. 2014;157(5):1061-72.
63. Hashimoto YK, Satoh T, Okamoto M, Takemori H. Importance of autophosphorylation at Ser186 in the A-loop of salt inducible kinase 1 for its sustained kinase activity. Journal of cellular biochemistry. 2008;104(5):1724-39.
64. Yamaguchi H, Matsushita M, Nairn AC, Kuriyan J. Crystal structure of the atypical protein kinase domain of a TRP channel with phosphotransferase activity. Molecular cell. 2001;7(5):1047-57.
65. Duan J, Li Z, Li J, Hulse RE, Santa-Cruz A, Valinsky WC, et al. Structure of the mammalian TRPM7, a magnesium channel required during embryonic development. Proceedings of the National Academy of Sciences. 2018;115(35):E8201-E10.
66. Schmitz C, Perraud A-L, Johnson CO, Inabe K, Smith MK, Penner R, et al. Regulation of vertebrate cellular Mg2+ homeostasis by TRPM7. Cell. 2003;114(2):191-200.
67. Ryazanov AG. Elongation factor-2 kinase and its newly discovered relatives. FEBS letters. 2002;514(1):26-9.
68. Schnitzler MMy, Wäring J, Gudermann T, Chubanov V. Evolutionary determinants of divergent calcium selectivity of TRPM channels. The FASEB Journal. 2008;22(5):1540-51.
69. Kerschbaum HH, Cahalan MD. Single-channel recording of a store-operated Ca2+ channel in Jurkat T lymphocytes. Science. 1999;283(5403):836-9.

70. Kozak JA, Kerschbaum HH, Cahalan MD. Distinct properties of CRAC and MIC channels in RBL cells. The Journal of general physiology. 2002;120(2):221-35.
71. Bates-Withers C, Sah R, Clapham DE. TRPM7, the Mg 2+ inhibited channel and kinase. Transient Receptor Potential Channels. 2011:173-83.
72. Chubanov V, Schäfer S, Ferioli S, Gudermann T. Natural and synthetic modulators of the TRPM7 channel. Cells. 2014;3(4):1089-101.
73. Runnels LW, Yue L, Clapham DE. The TRPM7 channel is inactivated by PIP 2 hydrolysis. Nature cell biology. 2002;4(5):329-36.
74. Jansen C, Sahni J, Suzuki S, Horgen FD, Penner R, Fleig A. The coiled-coil domain of zebrafish TRPM7 regulates Mg· nucleotide sensitivity. Scientific reports. 2016;6(1):1-13.
75. Matsushita M, Kozak JA, Shimizu Y, McLachlin DT, Yamaguchi H, Wei F-Y, et al. Channel function is dissociated from the intrinsic kinase activity and autophosphorylation of TRPM7/ChaK1. Journal of Biological Chemistry. 2005;280(21):20793-803.
76. Huttlin EL, Bruckner RJ, Navarrete-Perea J, Cannon JR, Baltier K, Gebreab F, et al. Dual proteome-scale networks reveal cell-specific remodeling of the human interactome. Cell. 2021;184(11):3022-40. e28.
77. Huttlin EL, Bruckner RJ, Paulo JA, Cannon JR, Ting L, Baltier K, et al. Architecture of the human interactome defines protein communities and disease networks. Nature. 2017;545(7655):505-9.
78. Gillingham AK, Munro S. The small G proteins of the Arf family and their regulators. Annu Rev Cell Dev Biol. 2007;23:579-611.
79. Bai Z, Feng J, Franken GA, Al'Saadi N, Cai N, Yu AS, et al. CNNM proteins selectively bind to the TRPM7 channel to stimulate divalent cation entry into cells. PLoS biology. 2021;19(12):e3001496.
80. Zierler S, Yao G, Zhang Z, Kuo WC, Pörzgen P, Penner R, et al. Waixenicin A inhibits cell proliferation through magnesium-dependent block of transient receptor potential melastatin 7 (TRPM7) channels. Journal of Biological Chemistry. 2011;286(45):39328-35.

Acknowledgements

This work was performed in the laboratories of Prof. Dr. Thomas Gudermann and Dr. Vladimir Chubanov at the Walther-Straub-Institute of Pharmacology and Toxicology of the Ludwig-Maximilians-University in Munich. This thesis would not have been possible without the emotional support and professional assistance of various people, to whom I would like to express my gratitude.

First of all, I would like to thank **Prof. Dr. Thomas Gudermann** for giving me the opportunity to accomplish my PhD in his laboratory at the Walther-Straub-Institute, for analytically reading of this thesis.

I also would like to sincerely thank **Prof. Dr. Susanna Zierler** for supervising this thesis, her extremely valuable professional advices and for the comprehensive introduction into electrophysiological technique. I am immensely grateful for all the experience and knowledge I gained while working with Susanna.

I would like to express my profound gratitude to my supervisor **Dr. Vladimir Chubanov** for his excellent scientific guidance, his great scientific enthusiasm and for providing exciting research projects. I highly appreciate his precious scientific suggestions, the patience and time he invested while supporting me during my practical work and writing.

I would like to thank **Prof. Dr. Maria Kurnikova** and **Prof. Dr. Wolfgang Nörenberg** for collaboration and for providing us with valuable data in molecular modelling and single-cell patch-clamp experiments.

Special thanks go to all my present and former colleagues: **Miyuki Egawa, Joanna Zaißerer, Anna Rössig, Anna Erbacher, Banu Akdogan, Lisa Pleninger, Leonor Correia, Angel Tseung, Sebastian Weidenbach, Silvia Ferioli and Lorenz Mittermeier** for the helpful, motivating and friendly working atmosphere in the laboratory. In particular I am very grateful to Joanna for her experimental support and technical assistance in the laboratory. Thank you for your positive attitude and for providing us with your delicious Nussecken und carrot cake. A special thanks goes to Miyuki, who became a valuable friend over the years, for her helpful advices, encouraging lunch breaks and support in laboratory work especially in confocal microscopy. A big thank you to **Miyuki** and **Anna Rössig** for supporting me in

patch-clamp experiments during revision of the publication 1. Special thanks also to **Anna Erbacher** and Miyuki for the critical reading of my thesis.

In addition, I would like to extend my thanks to all members of the Walther Straub Institute for their support over the years.

On a personal level I would like to thank my beloved friends and family: My parents, **Gerhard** and **Rita**, as well as my brother **Mathias** for their constant emotional, financial and encouraging support during my studies and my whole life. **Nynke, Anna and all other friends** deserve my profound gratitude for supporting me in my personal life and for being there whenever I needed. Special thanks to **Nynke** for encouraging me to start my master studies in biology after finishing the first state exam. I am extremely grateful to have you all in my life.

Last but not least, I want to thank **Christoph**, my beloved husband and father of our little son **Jonas** for being a constant source of support during the ups and downs of my master and PhD studies and for giving me unlimited happiness, support and motivation in our young family life.